Title

Enabling Multi-Functionality through a Low-Cost Hybridization Method of ZnO Nanostructure

Author

Quan, Jonathan

Publication Date

2014

UNIVERSITY OF CALIFORNIA,

Los Angeles

Enabling Multi-Functionality through a Low-Cost Hybridization Method of ZnO Nanostructure

A dissertation submitted in partial satisfaction of the
requirements for the degree Doctor Philosophy
in Materials Science and Engineering

by

Jonathan Timothy Quan

2014

ABSTRACT OF THE DISSERTATION

Enabling Multi-Functionality through a Low-Cost Hybridization Method of ZnO Nanostructure

by

Jonathan Timothy Quan

Doctor of Philosophy in Materials Science and Engineering

University of California, Los Angeles, 2014

Professor Jenn-Ming Yang, Chair

This dissertation presents the investigation of hybridizing ZnO nanostructures on carbon fiber through a new, low-cost and robust method. The method developed in this dissertation will lead to the development of novel multifunctional composites.

Carbon fiber bundles coated with galvanization zinc particles were subjected to joule heating to initialize Self-propagating High-temperature (combustion) Synthesis (SHS) in atmospheric conditions. The bundles were made into a composite through a wet layup process. Upon mechanical deflection, the composite produced a voltage response of 0.1V. The hybridization of ZnO nanostructures on carbon fiber was designed to enabled multi-functionality for carbon fiber reinforced composites including sensing, damping, and energy harvesting.

To understand this method, the reactions dynamics and the ZnO nanostructures growth mechanisms were investigated. It was found that the combustion reaction is affected by the amount of zinc precursor concentration and the heat transfer rate. The greater amount of zinc precursor requires a lower heat transfer rate to initiate the SHS process. Upon a sufficient heat transfer, combustion will occur. If the heat transfer rate is too low, no combustion occurs. Near the minimum heat transfer rate, the reaction is considered metastable. The results of the reaction were characterized through SEM, TEM, and XRD. Various ZnO nanostructures such as tetrapods, sheets, nanowires, and hollow sea urchins were observed for the SHS reaction, metastable reaction, and the non-combusted reaction.

ZnO nanostructure growth mechanisms were understood through vacuum thermal oxidation and CVD experiments. Thermal oxidation develops ZnO nanostructures through diffusion mechanisms where as CVD develops ZnO through deposition mechanism. Based on the similarity of ZnO nanostructures were found in the vacuum systems and SHS process, ZnO nanostructure growth mechanisms were proposed for the combustion process. ZnO nanostructures hybridized on the carbon fiber grow through deposition and diffusion mechanisms. The nanostructures' growths are affect by the heat transfer rate and oxygen availability.

Finally, a composite with piezoelectric response has been constructed and demonstrated.

The dissertation of Jonathan Timothy Quan is approved.

Suneel Kodambaka

Chi On Chui

King-Ning Tu

Jenn-Ming Yang, Committee Chair

University of California, Los Angeles

2014

This work is dedicated to my family, my friends, and my God.

Table of contents

List of Figures

Acknowledgements:

An old African proverb states: “It takes a village to raise a man”. I agree with this wholeheartedly because my advisor, mentors, family members, and friends have supported and encouraged me through wonderful conversations, lessons, and employment opportunities.

First, I would like to thank my advisor, Professor Jenn-Ming Yang for giving me the opportunity to pursue my interest in nanostructure materials and structural materials. Though many of my ideas were unobtainable, I am grateful for the strong advice and encouragement to try new ideas. Second, I want to thank Professor Suneel Kodambaka for allowing me to work and interact in his lab. I have become a stronger critical thinker, always asking “why?” until a satisfactory answer can be met. Third, I want to thank Professor Arie Venkert for taking me under his wing during his sabbatical at UCLA. I have become a better scientist and a stronger person under his guidance. Fourth, I want to thank Professor Donald Browne and Dr. Gershon Weltman for entrusting me as an Ethics TA for many years. I will miss conversing on the couches and reading the fascinating title spines on the bookshelves. Fifth, I would like to thank Professor Kanji Ono, Professor Marek Przystupa, and Dr. Neil Siegel for employing me as a TA for their respective courses. These opportunities have allowed me to continue my research.

I want to thank my lab partners in the Hybrid and Multi-Phase Materials Lab and the In situ Microscopy Lab who have mentored and assisted me in my research and provided wonderful friendships. Dr. Po-Ching Yeh has been a great mentor and provided great assistance to my projects. Discussions with Dr. Henry Colorado spurred the idea of hybridizing ZnO nanostructures on carbon fiber. Dr. Yuya Murata and Dr. Jeung Hun Park have been great mentors in vacuum systems and crystal growth. They helped me get started when I started with just a lab bench. Joseph Severino has been a great peer; I learned a great deal from him and am always inspired by his DIY attitude. Chilan Ngo has been a great lab mom and helped in my TEM analysis.

In the Materials Science and Engineering Department, I want to thank Dr. Sergey Prikhodko for his patient guidance in electron microscopy. Many of the images I have in my thesis were developed under his guidance. I also want to thank Jeff McKay for his help in the clean room. My fears of acids are greatly lessened, which will be very useful for my next opportunity.

I also want to thank the people outside the lab who were equally supportive of my work and interest. My parents have been thoroughly supportive of my education and life goals. More importantly, they have helped shape me into the man I am today. Austin, my brother, has been a constant encouragement. I am grateful for our strong sibling bond and memories together. Spencer, my mentor for many years, kept me grounded throughout my time as a UCLA student. I am grateful for his intentional encouragement and guidance. Jessica, my fiancée, I am blessed to have her in my life. I am grateful for her support, encouragement, and willingness stick by my side. Mission accomplished. Finally, I know there are many names that should be listed here, but I promise that none of you are forgotten.

VITA

2008 B.S., Materials Science and Engineering, University of California Los Angeles, Los Angeles, California

2010 M.S., Materials Science and Engineering, University of California Los Angeles, Los Angeles, California

PUBLICATIONS IN PREPARATION

Chapter 1: Literature Review

1.1. Multifunctional Materials: an Open Opportunity

In the last decade, multifunctional materials have been under investigation for their advantages in weight saving, sensing, energy harvesting, antimicrobial, and structural support[1,2,3,4]. Multifunctional materials can be defined as materials used for more than one intended purpose. For the last century, materials were primarily studied and developed for their individual unique properties[5]. The prominent fields for materials science include structural, electric, optical, magnetic, and thermal properties. Initially through systems engineering, firms have found creative ways to integrate and utilize the materials we have today. As fundamental understanding of prevalent, precious, rare, and exotic materials expanded, it has opened up the opportunities for the integration of many materials to serve more than one function[6].

Multifunctional materials can address engineering requirements with more environmentally friendly and energy efficient processing and fewer raw materials[1]. This allows for more efficient use of materials that saving weight and lower redundancies in structure and processing. Multi-functionality can be added through smart materials, which can have the ability to experience changes in their properties through external stimuli. Multi-functionality for materials offers a unique opportunity for a variety of applications while providing a significant decrease in redundancies. It is important that research and development for multifunctional materials are pursued because they will help continue to address key concerns in the consumer market, national interest, and humanity.

Current success of Smart Mobile Devices[7] provide an analogy of the type of impact that multifunctional materials could bring into our society. Smartphones combine the capabilities of multiple devices, which saves weight for users and offers more utility than its original purpose for audio communication. Some of the features that Smartphones possess include: wireless device communication, wireless data streams, photography, filming, gaming, navigation, music, videos, better battery life, and strong calculation processing[8,9]. From these smart devices, many software applications have been developed that have helped provide greater utility for the end user[10]. The integration of all these devices and new software provides an enhanced user experienced where the utility of the whole unit is greater than the sum of its components[11]. That same design philosophy is quite often used for composite manufacturing. Different materials are brought together to utilize their individual unique properties[12].

For this multifunctional material work, the following properties were desired: good structural properties, multifunctional properties, and well known and energy efficient processing properties. Through a material selection process, carbon fiber and zinc oxide (ZnO) were chosen for this work. To fulfill the structural property requirement, carbon fiber was chosen for its low density, corrosive resistance, good tensile strength, and good modulus[13]. A Scanning Electron Microscope (SEM) image of a carbon fiber bundle (Cytec T300) is seen in figure 1.1. The fibers have an average diameter 5µm and connected through sizing. ZnO was chosen for its functional properties, which include: semiconducting, photo excitation, and piezoelectricity properties were desired[14,15,16,17]. A diagram of its properties can be seen in figure 1.2[15]. Both materials are both widely available and have well-established processes each material cost effective; additionally, it was also discovered that ZnO has many nanostructures. The reduced size is known to enhance many functional materials' properties making, materials with nanostructure variation are desired. Figure 1.3[18] shows an image of the variation of ZnO nanostructures produce under different carbothermal evaporation CVD. This selection left us with carbon fiber and ZnO nanostructures.

The purpose of this work is to demonstrate a possible method to develop multifunctional materials through the use of ZnO nanostructures on carbon fiber that is both cost and energy efficient. The first part of this work will discuss the fundamentals of ZnO nanostructure synthesis through widely used techniques: thermal oxidation (TO) and chemical vapor deposition (CVD)[19,20]. Each of these techniques is important because ZnO nanostructures can grow through diffusion or deposition growth mechanisms. By understanding the ZnO properties, changes in process designs can be made to current systems to help make ZnO nanostructures synthesis more energy efficient, resulting in cost effectiveness. The second part of this works attempts to hybridize ZnO nanostructures on carbon fiber using a cost effective and robust combustion method. The growth mechanisms that were observed in TO and CVD can be used to help explain nanostructures seen in the hybridization combustion synthesis. Through hybridization of ZnO nanostructures on carbon fiber, multi-functionality is added onto carbon fibers through the ZnO nanostructures[21]. These can be used to develop multifunctional composites with the possibility of sensing, dampening, and energy harvesting[22,23,24].

1.2. Carbon Fiber Basics

Carbon fiber is a well-known high-strength material, which has been primarily used as reinforcement for a polymer and cement matrices. Qualities that have made carbon fiber an appealing structural material include its low density, high tensile strength, and high modulus. For many decades, carbon fiber research and development were focused on the high technology sector such aerospace engineering. Their goal was to increase carbon fiber yield for large-scale production and increase maximum performance[13].

The yield significantly increased when polyacrylonitrile (PAN) and pitch based fibers were discovered. It not only allowed for greater carbon fiber production yields but also produced superior carbon fibers derived from natural fiber sources. PAN based carbon fibers tend to have better tensile strength and elongation to break percentages; whereas pitched based carbon fibers offer better modulus[25]. Fiber quality improvements have included various additional precursors, processing adjustments, alignment, and surface treatments. Since then, they have achieved 90-95% of the graphite's theoretical modulus of (~1025GPa) and a reported tensile strength of 7GPa. From a production standpoint, carbon fibers with a tensile strength of 5GPa are much more feasible to achieve. Table 1 shows of high performance fibers and their respective properties[26].

Additional qualities that have made carbon fiber an appealing structural material include its good chemical resistance, fatigue resistance, low linear coefficient of thermal expansion, and good strength retention at high temperature. These qualities allow for successful applications in harsher environments where its metal counterparts cannot sustain. Carbon fiber also has appealing properties that are not required for many structural applications including good electrical conductivity and thermal conductivity.

The culmination of carbon fiber research and development has led into currently available outstanding commercial products. For commercial airliners, the Boeing 787 offers better fuel efficiency and better passenger comfort[27]. The increased fuel efficiency is derived from the weight savings from the replacement of metal components for the low density of carbon fiber. Additionally, carbon fiber's resistance to fatigue and corrosion has improved passenger comfort. Flights are now allowed to have greater cabin pressure with humidity comparable to air-conditioned buildings. Prior to carbon fiber, the cabin pressure and humidity had to be artificially reduced to prevent fatigue and stress corrosion in aluminum based fuselages. For ground transportation, automobiles have also benefited in weight reduction and complex shapes manufacturing. These are used for applications in high performance sports or fuel-efficient vehicles. For many years, carbon fiber was only exclusively used for high tech applications, but it is now more accessible for civilian products.

1.3 ZnO Basics

ZnO is a well-known II-VI semiconductor and has been heavily studied for its wide band gap[16,17] and strong piezoelectric response[28,29]. ZnO has applications in photophysics[30], photochemistry[31], radiation hardness[32], and near ultra-violet optical devices[33]. ZnO is also a well-known material that produces a variety of nanostructures. Some of the basic material properties of ZnO are listed in Table 2[16].

The history behind ZnO is quite rich dating back to Biblical copper smelting. For the last 1000 years, ZnO, originally known as Cadmia or “philosophers wool”, was a useful material with application in pigments, cements, and pharmaceuticals. In 1781, a German chemist it was discovered that ZnO could be developed through the burning of metallic Zinc. This process was adopted by industry in 1840 when Leclaire manufactured large quantities of ZnO through burning zinc in air. Metallic zinc is melted in a graphite crucible above the boiling temperature of 907°C. At temperatures greater than this, metallic zinc begins to boil; the produced vapors begin to react with the oxygen in the air. This process is known as the French Method, which is an indirect process because it requires zinc ores to be transformed into metallic zinc before it can be turned into ZnO. In 1852, the New Jersey Zinc Company found a more economic method of producing ZnO through the smelting of zinc ore with coal. This method is known as the American Process, which is a direct process because it transforms zinc ore directly to ZnO[14].

In the 1950’s, a resurgence of research and developmental interest was poured into ZnO’s fundamental properties because thin films were discovered to have unique II-VI semiconducting solid-state properties for semiconducting, piezoelectric responses, sensing, catalytic, and thermal applications. During this period, understanding of ZnO chemistry, crystallography, and fundamental properties were better understood[14].

In the early part of the 21st century, ZnO once again became the darling of the scientific community because it was a well-known material that exhibited a variety of different nanostructures[15]. These nanostructures include tubes[34], nanowires[35], sheets[36], and tetrapods[37]. Beyond the scientific curiosity of these nanostructures, there were many who were interested in potential applications for these nanostructures[14,15]. Properties of ZnO at the nanoscale, like other materials, are very different than properties at bulk scale. Since ZnO had a variety of nanostructures, many have ventured into understanding these structures to manipulate and fine tune specific properties.

1.3.1. ZnO Composition

Based on the phase diagram[38] shown in figure 1.4, Zinc Oxide is a simple II-VI material, where there are two stable stoichiometric ratios: ZnO and ZnO_2 [38]. Amongst these two compounds, ZnO is the most common and stable. Due to the lack of stoichiometric variety, it is helpful for characterization. ZnO will readily form when Zn is exposed to oxygen rich environments. To form ZnO, Zn can be in solid, liquid, aqueous, or vapor form. Once formed, ZnO is stable until it is heated to $1200^{o}C$[14]. Decomposition at lower temperatures is achievable in the presence of a catalyst or carbon.

1.3.2. Crystal structure

ZnO's structure is composed of alternating coordinates of Zn^{2+} and O^{2-} ions. Zinc Oxide is known to have three different crystal structures (also known as phases): Wurtzite, Zinc Blende, and Rocksalt[16]. In each of these phases are shown in figure 1.5[16], the Zn^{2+} and O^{2-} create interpenetrating sub-lattices. Amongst these phases, the Wurtzite phase is the most commonly found and used. In Wurtzite and in Zinc-Blende crystal structures, the Zn and the O ions have a tetrahedral coordination, where each Zn ion bonds with four O ions and vice versa. Normally a tetrahedral coordination is an indicator of covalent sp^3 bonds, but ZnO Wurtzite and Zinc-Blende structures are considered partially covalent and ionic with an iconicity of f_i=0.616 on the Phillips iconicity scale[39]. For Rocksalt formation, the bonding between Zn and O ions are primarily ionic.

The order of these phases are based upon free energy level where Wurtzite has the lowest free energy of -5.658 eV, Zinc-Blende has an intermediate free energy of -5.606e eV, and Rocksalt has the highest free energy -5.416 eV. The lattice parameters of the phases are also known where the Wurtzite phase's lattice parameters are a= 3.25 Å and c= 5.207 Å; the Zinc-Blende phase's lattice parameter is a= 4.62 Å[40]; and the rock salt phase's lattice parameter is 4.25 Å[41]. A diagram comparing the free energy and the volume per formula unit is shown in figure 1.6[42].

The Wurtzite (WZ) crystal structure is based on a hexagonal unit cell with an ideal c/a ratio of 1.633. However, ZnO's c/a ratio is 1.602. This departure from the ideal ratio is caused by the natural polarization between the Zn (cation) and the oxygen (anion). The Zn and O are arranged together in a tetrahedral making the bond between the two ions more covalent in nature[16]. Amongst the different phases, the WZ phase is commonly found in ambient conditions. Increases in temperature or pressure will cause shifts in free energy, which results in phase changes.

The WZ phase is also well known for its non-central symmetry polar surfaces. The most common face is the (0001), also referred to as the basal plane. Other common facets include $(10\bar{1}0)$ and $(11\bar{2}0)$ planes. Amongst these facets, only the (0001) facet is polar[43]. This facet is also atomically flat and stable requiring no surface reconstruction. The polarization derives from the Zn and oxygen faced surfaces. The Zn faced surface generate a positive charge whereas O faced surfaces generate a negative charge. Amongst the facets, the (0001) facet has the highest surface energy, resulting in this facet having the highest growth rate during synthesis as the crystal continuously tries to minimize the surface area. This has been observed in both diffusion and vapor deposition growths. Amongst the other two common facets, the $(10\bar{1}0)$ facet is also stable, but the $(11\bar{2}0)$ is less stable and has a high degree of surface roughness.

The Zinc-Blende (ZB) crystal structure is based off of two intertwined face-center-cubic (FCC) sub-lattices. The intertwined FCC sub-lattice is positioned at four different one quarter of the diagonal positions. Amongst the phases, the ZB crystal structure is considered to be a metastable phase. The ZnO ZB phase and ZnO WZ phase are very close in free energy and primarily differ in stacking sequence. For FCC crystals, the stacking sequence is observed in the [111] direction in the ABCABC order. The ZnO Wurtzite mimics the hexagonal stacking sequence and the Zinc-Blende follows the FCC sequence. For hexagonal systems, the stacking sequence is observed in the [0001] direction in the ABABAB order. For the Zinc-Blende structure, the observed stacking sequence in the [111] direction follows the AaBbCcAaBbCc order[16], where the capital letters represent the cation and the lowercase letters represent the anions. The sequence for Wurtzite in the [0001] direction is AaBbAaBb. For ZB ZnO growth, a cubic-crystal based substrate must be used[44,45,46].

The Rocksalt (RS) crystal structure is based on the cubic structure commonly found in the NaCl crystal system, where the Zn fills the cation positions and the O fills in the anion positions. In most literature the RS ZnO phase can be obtained from the WZ ZnO phase under external hydrostatic pressures above 10GPa[47]. Above this pressure RS ZnO is stable. The heavy pressure causes a phase change in ZnO from WZ to RS because the interionic coulomb interactions become more ionic versus covalent. The phase change begins to occur at hydrostatic pressures 9.1±0.2 GPa. This transformation was observed through energy-dispersive x-ray diffraction (EDXD) under synchrotron radiation in situ when the ZnO WZ was exposed to increasing hydrostatic pressures[41]. The transformational pressure for ZnO WS to ZnO RS is relatively modest in respect to other II-VI semiconductor[16].

1.3.3. Wurtzite Properties

The WZ phase has been heavily studied for three unique solid-state properties: high band gap semiconductor properties, Photoelectrochemical properties, and piezoelectric properties. ZnO's other properties include ferrite properties, catalytic properties, and candoluminescent properties[48,49]. These other properties will not be discussed in the scope of this work.

The basis of ZnO's properties comes from its polar structure. Cations are created from zinc atoms and anions are created by oxygen atoms. The cations help contribute mixed valence states where as the anions create deficiencies through vacancies. Through careful ZnO synthesis and processing, the ratios of cations and anions can be altered thus altering the polar nature of ZnO. If controlled, the electrical, optical, and magnetic properties can be manipulated.

1.3.4. Semiconducting Properties

ZnO is a direct wide band gap II-VII semiconductor with a band gap of E_g=3.37 eV at room temperature. At low temperature, the band gap can be as high as E_g=3.44eV[17]. A wide band gap semiconductor is generally defined as a material with a band gap between 2 - 4eV. Above 4eV, a material is classified as an insulator.

Work on ZnO as a semiconductor and electron property research have included ZnO as a substrate for GaN and other alloy growth, availability of high quality bulk single crystals, opportunities for electoral conductivity modification, and strong luminescence for lasers. Due to its wide band gap, ZnO can have photoemissions in the green, blue, or UV region. ZnO also has a high mobility and high carrier density. When prepared with the proper technique and proper donor concentration, the mobility was measured to be of $205cm^2V^{-1}s^{-1}$ at room temperature and as high as $2000cm^2V^{-1}s^{-1}$ at 50K[50]. Applications for ZnO as a semiconductor have included: photodetectors[51], photoconductors[52], light emitting diodes in the blue and ultraviolet region[53].

Like many other semiconductors, ZnO's electronic properties can be adjusted by suitable annealing heat treatment and dopants. Naturally, ZnO is n-type semiconductor. Some have explained that the ZnO is naturally zinc rich which can be seen in the phase diagram. Like most semiconductors, ZnO experienced an increase in conductivity at elevated temperatures. Annealing heat treatment increases ZnO's conductivity by removing a variety of defects. These imperfections include crystal distortions based on surface tension, vacancies, substitution of Zn or O atom, or interstitial atoms. Further study show that the primary increased conductivity comes from O vacancies, not Zn interstitials[54]. Elements such as magnesium, cadmium, chromium or aluminum in small quantities can increase the conductivity. Band-gap engineering can also be achieved through cadmium and magnesium doping. Cadmium will decrease the band gap whereas Magnesium will increase the band-gap[16]. Thus, band-gap engineering can be achieved through cadmium oxide and magnesium oxide interfaces.

Obtaining p-type ZnO doping has been a challenge for ZnO due to limited understanding and ZnO's natural n-type conductivity tendencies[17]. Recently however, better understanding of ZnO n-type conductivity and various dopants that act as acceptors have helped lower ZnO's conductivity. Some of these doping elements include lithium, sodium, phosphorous, and arsenic. Reliable p-type doping would open up new opportunities in device applications, especially in light emitting diodes and lasers[55].

1.3.5. Photoelectrochemical Properties

For many decades there has been a lot of excitement towards ZnO's photoelectrochemical properties especially photoluminescence, cathodoluminescence, and electroluminescence. More importantly, ZnO nanostructures can adjust and fine-tune these properties due to the size effect.

Energy absorption must first take place for an electron to be excited from the ground state to an excited state in order for luminesce to occur through photoluminescence, cathodoluminescence, or electroluminescence. Upon the electron's return from the excited state to the ground state, light is emitted as excess energy is released. A diagram of energy states is shown in figure 1.7[55].

For photoluminescence, ZnO experiences photoexcitation before light is released. Photoexitiation is defined as electron excitation from the ground state to excited states through photon absorption. For ZnO, high-energy light in the UV region is required for excitation. Similarly, cathodoluminescence is the process in which ZnO absorbs electrons from an electronic beam for electron excitation. Finally, for electroluminescence, ZnO absorbs electrons through electric current for electron excitation.

When the excited electrons return to the ground state, the transition releases energy in the form of light. Based on the ZnO's inherent band gap, ZnO will produce a green luminescence with a wavelength of 535nm. The color of the emitted light can be adjusted through dopants or perfections of the crystal structure[56]. To adjust the emitted light, shallow donor or deep acceptor dopants are used to lower the band gap for the emission of longer wavelengths.

In addition to dopants, the photoemission can also be adjusted by the size of the ZnO. A blue shift in luminesce can be experienced for ZnO nanostructures that have features smaller than 200nm under an electron beam with an accelerating voltage of 15kV. The smaller the diameter, the further the shift towards the lower wavelengths will be illuminated[57]. The shift caused by the band gap narrowing effect will decrease in the band gap width because of an electron-electron repulsive interaction. In addition, there is a Bursteian-Moss (BM) effect, which is experienced in n-type semiconductors. Through the BM effect the band gap is enlarged which affects absorption and photoluminescence[58]. Both of these effects will cause the Fermi level to move into the conduction band causing a filling of the conduction band. Thus for excitation to occur, electrons much reach the valence bands that are around or above the Fermi level. The blue shift or the BM shift (ΔE_{BM}) can be explained through the following equation:

$$\Delta E_{BM} = \left(1 + \frac{m_e^*}{m_h^*}\right)\left(\left(\frac{3}{\pi}\right)^{2/3} \frac{h^2}{8m_e^*} n^{2/3} - 4KT\right)$$

where m^*_e is the effective mass for an electron, m^*_h is the effective mass for a hole, h is the Planck constant, K is the Boltzmamn constant, n is the electron carrier concentration in the conduction band, and T is the absolute temperature. The mechanism behind the blue shift is the increase in the electron carrier concentration in the conduction band when the diameter for nanostructures decreases below a threshold value. The smaller diameter offers a greater surface to volume ratio. Thus when secondary electrons are excited under an electron beam, they can be easily transported to the surface. Without this transport to the surface, secondary electrons would be accumulated and would prevent further electrons from becoming absorbed for excitation.

1.3.6. Piezoelectric Properties

ZnO has a piezoelectric strain constant of d_{33}=12.4 (10^{-12}C/N)[59] which is the highest value amongst tetrahedrally bonded semiconductors. The ZnO Wurtzite derives its piezoelectric configuration from its polar tetrahedral configuration. ZnO has a c/a ratio of 1.602, which is off from the ideal hexagonal Wurtzite c/a ratio of 1.633. This results in a normal dipole moment and polarization in the c-axis. Thus when a mechanical stress is introduced, a change in potential is experienced due to the polarity. The piezoelectric properties also experiences a size effect[60]. At lower frequencies, nanostructures experience a greater piezoelectric coefficient. A figure of Wang and Zhoa's work showing the piezoelectric strain coefficient increase due to the size effect is shown in figure 1.8.

Piezoelectricity can be defined as electromechanical coupling where certain materials demonstrated reversibility in electro-elasto-mechanical deformation. Under mechanical stress these materials generate electrical polarization. Conversely under an electrical field, these materials undergo mechanical deformation. Through these properties, it earned its name "piezo" which translate into "to press" from Greek[61]. The piezoelectric materials that are widely used include crystals, ceramics, and polymers.

Only materials with crystallographic atomic structures have shown piezoelectric properties. Currently, there are 32 crystal classes. 21 of these 32 crystal classes lack a center of symmetry. Amongst this smaller group, 20 of these possess piezoelectricity properties. Thus there is a direct correlation between lack of symmetry and piezoelectricity[2,62]. When mechanical stress is applied, the symmetry of these crystals is altered thus causing a disturbance in the moment. Vice versa, when an electrical field is applied, the crystal undergoes mechanical deformation. This is the fundamental theory for the piezoelectricity at the atomic level.

Piezoelectric materials are used in commercial transducers and actuators for sensing and energy harvestors. Transducers transfer one signal to another signal; making devices such as sensors effective. Actuators are defined as devices that can mechanically move or induce a mechanical force which is possible through the converse effect. Sensors on the other hand, produce a signal through the direct effect, where a mechanical force creates a displacement in the polarization in the material. Many sensors are used for ultrasonic and sonar applications through the creation of images though echoes[2].

The electromechanical coupling has two major components, the electric charge displacement, D, and strain, S. The electric charge displacement (C/m^2), D, and it can be expressed as:

$$D = \varepsilon E$$

Where ε is the relative permittivity[F/m] and E is the electric field strength (Vm^{-1}). Strain, S, can be expressed through Hooke's law:

$$S = sT$$

Where s is the compliance (10^{-12}m^2/N) and T is the stress (N/m^2).

When the two components are coupled, it can be expressed as

$$\{S\} = [s^E]\{T\} + [d^t]\{E\}$$

$$\{D\} = [d]\{T\} + [\varepsilon^T]\{E\}$$

where d is known as the piezoelectric charge constant (or the piezoelectric strain constant). In matrix form, piezoelectric charge constant, d, expresses the direct piezoelectric effect whereas d^t is the matrix for the converse piezoelectric effect. The superscript t represents the transposition of a matrix. The superscripts E and T are used to indicate electrical or mechanical boundary conditions. For electrical boundary conditions, the superscript E represents the material under a zero or constant field. For the mechanical boundary condition, the superscript T represents the material being under zero or constant stress. In other electromechanical relation equations, other subscripts such as D or S may be observed where D represents constant electric charge displacement and S represents constant strain[62]. With these important parameters, it sets up the ability to characterize the different constants that help represent different ratios. Under these boundary conditions, the equations can be simply expressed as:

$$S= d^t *E$$

$$D= d *T$$

The piezoelectric charge constant, d, dictates the polarization generated per applied mechanical stress (T) unit. It can also be expressed as the mechanical strain experienced by the piezoelectric material under per applied unit of electric field.

The piezoelectric charge constant, d, can be represented as the piezoelectric voltage coefficient, g_{ij} (Vm/N).

$$g_{ij} = d_{ij}/\varepsilon_0\varepsilon$$

This parameter is often used because g_{ij} directly relates the electric field to applied stress. The piezoelectric voltage coefficient, g, is a function of the piezoelectric charge constant, d, and takes into account the inverse contributions of ε_0, the permittivity of free space, and ε, the relative dielectric constant of the material. When researchers work on applications used for sensing or energy harvesting, this parameter should play a factor in their materials selection. The two subscripts: i and j, are often associated with d. The first subscript describes the direction of the induced polarization, when the electric field is zero or the direction electric field applied; the second subscript describes the direction of the applied stress or induced strain. Bulk materials tend to have lower g_{ij} values because of higher ε values. However by reducing the material into fibers, ε is reduced thus increasing g_{ij} allowing the material to yield higher output voltage. Many materials that are used as transducers have very high g_{ij} and d_{ij}.

1.4. ZnO Nanostructure Synthesis

ZnO is well known for its micro and nanostructures. The methods to growth ZnO nanostructures include Thermal Oxidation[63], Chemical Vapor Deposition (CVD)[37,64] and Hydrothermal Reaction[65]. Other methods can be included in this list, but to a certain degree they are a derivation of these methods. Under certain conditions, CVD and hydrothermal reaction can also grow exceptionally pure ZnO crystals, with minimal defect bulk. The two methods under investigation for this work are vacuum thermal oxidation and CVD. These two methods are very different in terms of ZnO growth mechanisms. Thermal oxidation grows ZnO nanostructures from a diffusion mechanism where Zn ions travel through the ZnO structure to reach an oxygen rich environment. In the case of CVD, vaporized Zn and oxygen ions deposit on solid ZnO interface. For hydrothermal reactions, the ions come from supersaturated liquids that are adsorbed and crystalized onto the ZnO solid-interface. For this work, these two primary methods of interest, thermal oxidation and CVD will be discussed in detailed. Chapter 2 will further thediscuss the importance of temperature in thermal oxidation. Chapter 3 will discuss the effects of oxygen variation and the oxygen injection zones in CVD growth.

1.4.1. Thermal Oxidation

The thermal oxidation method is simply the reaction of a metal specie and oxygen. This can be explained by equation 1:

$$\frac{x}{y}M + \frac{1}{2}O_2 \rightarrow \frac{1}{y}M_xO_y$$

where M is the metal specie and O_2 is the oxygen molecule; x and y are the stoichiometric ratio units for a complete reaction with no byproducts. For thermal oxidation of zinc, the reaction follows the same metal oxide equation[63]

$$Zn + \frac{1}{2}O_2 \rightarrow ZnO$$

Due to the simple stoichiometric crystal structure, x and y are both determined to have the values of 1. Prior to oxidation, the metallic zinc precursor can be in the form of a solid or liquid. When the metallic zinc is exposed to oxygen, almost immediately after exposure, a metal oxide layer is formed. Interestingly, the reaction immediately slowed because the newly formed layer serves as a barrier for metallic zinc to reach the oxygen rich environment. To reach the oxygen rich environment, the metallic zinc diffuses through the metal oxide level. This can be seen in figure 1.9[63]. Zn diffusion between the metal-oxide layer has been found to be greater than oxygen diffusion through the metal oxide layer.

The rate at which Zn oxidation occurs is determined by the metallic rate consumption. This can be seen by the rate equation

$$\frac{-d[Zn]}{dt} \equiv r$$

where [Zn] is the available Zn specie, t is time, and r is the rate. In a closed system where the available oxygen is fixed, the rate equation can be expanded to the oxygen consumption rate. The concentration of Zn can be denoted as C. During oxidation, the instantaneous concentration, C, of the remaining metallic species could be determined with the following equation

$$C = C_0 exp\left(\frac{-x^2}{4Dt}\right)$$

where C_0 is the original concentration, x is the diffusion profile depth, D is the diffusivity, and t is time[66].

The rate, r, can be equated to the reaction rate constant, k. The chemical reaction rate constant, k, is dependent on temperature and available oxygen concentration. The temperature contribution is seen in the Arrhenius equation,

$$r = k = Aexp\left(\frac{-E_a}{RT}\right)$$

where A is the pre-exponential factor, E_a is the activation energy, R is the universal gas constant, and T is the temperature. The higher the temperature, the closer the exponential portion of the Arrhenius equation approaches the value 1.

For the zinc thermal oxidation, reaction is a solid-state diffusion process where existing zinc structures reacts with oxygen at the surface layer. Initial oxidation is quick, but the reaction is slowed by mass transfer diffusion. The oxide layer serves as a buffer-layer between an oxygen rich environment and unreacted Zn. Driven by the chemical potential, the unreacted zinc will diffuse through the oxide layer to reach and react with the oxygen rich environment[54]. For steady-state diffusion rates, Fick's law is used to describe the flux of concentration of material moving through a medium.

$$J = -D\frac{dC}{dx}$$

where J is known as the flux with units of $\left(\frac{mol}{m^2 \cdot s}\right)$, D is known as the diffusion coefficient with the units of $\left(\frac{m^2}{s}\right)$, C represents the concentration of the material where $\left(\frac{mol}{m^3}\right)$, and x is the position represented in length. For non-steady state cases where the diffusion causes the concentration to change over time, Fick's second law is used[67].

$$\frac{dC}{dt} = D\frac{d^2C}{dx^2}$$

where the constants are the same as Fick's first law with the additional condition of time, t (s)[68]. The diffusion coefficient, also known as diffusivity, is temperature dependent also described by the Arrhenius equation:

$$D = D_o exp\left(\frac{-E}{RT}\right)$$

where D_0 is the maximum diffusion coefficient, E is the activation energy (J), R is gas constant $3.14\left(\frac{J}{mol\cdot K}\right)$, and T is the temperature with units in kelvins, (K).

For Zn diffusion through ZnO, the diffusion mechanism is driven through vacancy diffusion as oppose to interstitial diffusion. This was measure through electrical measurements to confirm vacancy diffusion. Upon higher Zn vacancies, the conductivity is lower for ZnO. Zinc interstitials would not affect the conductivity as greatly as Zn vacancies. In addition, vacancy diffusion for isotropic conditions was also verified by the conditions of large activation energy for successful migration and formation; and a large pre-exponential in the Arrhenius equation[54].

For many years, it was thought that Zn diffusion in ZnO was isotropic, meaning that it did not follow any specific direction or crystal path. At the time, many of these experiments were conducted at the bulk level. In the 1970's, diffusion tests were performed on thin ZnO films to better determine depth profiles[69]. This allowed for better understanding of ZnO diffusion through different crystal directions. It must be noted that these diffusion experiments were performed on relatively lower temperatures. Higher temperature thermal oxidation would cause anisotropic ZnO growth at the micro and/or nanoscale[63].

Traditionally, low-temperature oxidation for metal structures that undergo isotropic oxidation display a uniform layer of oxidation. At higher temperature oxidation, scales develop due to easier nucleation of an oxide layer and respective faster growth of nucleated oxides[70].

The ZnO anisotropic growth under thermal oxidation baffled many researchers. Recently, it was agreed upon that ZnO diffusion coefficients for isotropic conditions were found to have a activation energy of 372 kJ/mol[54]. Specific Zn diffusion coefficients were found for different directions through ZnO. The two important directions include the c-axis [0001] and the a-axis [$11\bar{2}0$]. The diffusion coefficient in the [0001] direction was found to be

$$D_c = 8.2\times10^{-6} exp\left(-\frac{171}{RT}\right)\frac{cm^2}{s}$$

and the diffusion coefficient in the [$11\bar{2}0$] was found to be

$$D_a = 4.9\times10^{-6} exp\left(-\frac{169}{RT}\right)\frac{cm^2}{s}$$

At low temperature, the oxidation rate is very slow and the diffusion coefficients are not viable. Instead of an anisotropic structure, a uniform oxide develops at a slow rate[69]. Figure 1.10[15] shows nanowires and ribbons with common facets. However, at higher temperatures, the difference between the oxidation rates specific to the crystallographic directions is more apparent which helps points to different diffusion coefficients for different directions. As prolonged thermal oxidation continues, anisotropic materials begin to develop.

The anisotropic morphologies can be seen in many ZnO nanostructures specific to thermal oxidation which include nanowires, tubes, hollow spheres, and hollow sea-urchins. At temperatures above 450°C, nanowires will form. High temperatures will make Zn diffusion through the ZnO [0001] crystallographic direction[71] more favorable than other directions, which leads to the anisotropic ZnO structures[72,73]. The hollow ZnO structures are caused by the Kirkendall effect where there is faster diffusion of Zinc vs Oxygen through ZnO. As Zn diffuses through the ZnO layer, the ZnO layer grows in the direction of the oxygen rich environment leaving behind a cavity in the oxygen void area. The ZnO sea-urchins are unique nanostructures developed through a modified Kirkendall Process. Like other hollow structures, the sea urchin initially develops a ZnO shell when the Zn particle oxidizes at low temperatures or low oxygen conditions. As temperature or oxygen content increases, the unreacted Zn, beneath the ZnO shell surface, will accelerate its diffusion through specific ZnO orientations causing growths of ZnO whiskers/ nanowires in the [0001] direction. Thus the final structure is a hollow ZnO sphere covered by ZnO nanowires.

To understand how ZnO nanowires are grown under changing substrate temperatures, a vacuum thermal oxidation system was created with a tube furnace system fitted with two independent heating controls for Zn evaporation and substrate heating. The zinc heating source was an alumina crucible wrapped in a tungsten filament. The substrate heating element was made of a nickel chrome filament, which is used for oxidation resistance and lower temperature heating. The system was fitted with a roughing pump, which reached a minimum pressure of $2x10^{-3}$ Torr. Argon and oxygen gas lines were both attached to the system with independent gas flow controllers. The argon was used as transport gas, whereas oxygen was used as the reactant gas. For thermal oxidation, zinc first was evaporated and transported towards the substrate with argon. When the evaporation was completed and the heat source had cooled, oxygen was introduced into the system. The source was cooled to prevent oxidation of the precursor and the tungsten heating filament.

1.4.2. Deposition

ZnO can be deposited through either physical vapor deposition (PVD) or chemical vapor deposition (CVD). PVD is a method that physically transports materials via techniques such as evaporation and sputtering to a substrate. Upon contact with the substrate, the materials condense on the substrate to form a new layer. CVD is a technique where chemical reactants are transported to the substrate to undergo a chemical reaction. For most ZnO thin film applications, PVD through sputtering is used. Grown films are used for high bandwidth and/or for piezoelectric applications. However, CVD is preferred for nanostructure growth tetrapods[19,37,74], ribbons[75], nanowires[76], and sheets[36, 77]. Factors that affect ZnO deposition growth include Zn precursors, oxygen concentration exposure, pressure, and temperature.

CVD can be performed by a variety of different reaction types: pyrolysis, reduction, oxidation, compound formation, and combustion. In the case for pyrolysis, reactions are created by the thermal deposition of liquid species on hot surfaces[78,79]. In reduction CVD, ZnO can be reduced with graphitic carbon to form Zn vapors. This process is known as carbothermal evaporation[80]. For oxidation, metal is exposed to oxygen gas to produce oxides[19,37,81]. Deposition using compound formation requires different gasses such as carbides, nitrides, borides, or sulfide gases to produced compound materials. ZnO does not rely on compound formation. For combustion synthesis, a zinc ion rich solvent is brought to a flame and directed towards a substrate. The atmospheric oxygen reacts with the zinc ions to produced ZnO[82,83]. For most ZnO nanostructure synthesis work, the most popular method has been the combination of reduction and oxidation.

Zn precursors can come in a variety of a metal organic compounds such as zinc acetate[84] or Diethylzinc (DEZn)[85], as an oxide[86], or in metallic zinc form[37, 71] _ENREF_63. In every case, the goal for each of the precursors is to isolate the Zn component as Zn vapor. Metal organics[87] have been widely used because the Zn component can be controlled more easily in terms of quantity and can be isolated at relatively low temperatures. However, metal organics have a high cost per unit, which has limited its general use. For oxide precursors, decomposition of the oxide can occur under high temperature. The decomposition temperature of ZnO under vacuum is 1400°C. However, this decomposition temperature can be lowered to 950°C when it exposed to graphitic carbon[77,88]. This is known as carbothermal evaporation where the carbon reacts with oxygen ions to produce carbon dioxide. The thermodynamics of the reaction can be determined by the Ellington Plots[89,90]. In both ZnO vaporization and carbothermal ZnO evaporation, Zinc vapors are not produced until the required temperature is met. Thus the vapor pressure can be identified through the temperature/pressure chart[91] seen in figure 1.11.

$$2ZnO + C = CO_2 + 2Zn$$

For this type of growth, supplemental oxygen is required to reform ZnO.

$$2ZnO + C + 0_2 = CO_2 + 2ZnO$$

Carbothermal evaporation has been a very popular method to form ZnO nanostructures due to its simplicity and low cost of operation. ZnO developed from a metallic Zn precursor has been considered the most basic ZnO growth system. Zn vapors are easily produced because Zn has a melting temperature of 420°C and a boiling temperature of 920°C. Unfortunately, control has been limited due to metallic zinc's high vapor pressure. Additionally, when metallic Zn is exposed to oxygen, an oxide layer is quickly formed, which limits vaporization. Thus for controlled ZnO formation through metallic Zn precursors, it is important to have exact heating temperatures and controlled oxygen exposure regions.

Many research groups have shown that many nanostructures are dependent on synthesis temperature. Generally the progressive order of ZnO nanostructures is rods, nanowires, sheets, and tetrapods where the temperature is increasing for each structure[19,92,93]. When growing ZnO via CVD, it is important to understand that nanostructures have a lower melting temperature. This will allow ZnO synthesis with defined hexagonal structures to occur at temperatures below 700°C. This means that a system can be designed to have a lower synthesis temperature than current ZnO evaporation or carbothermal evaporation systems.

Oxygen concentration exposure plays a key role in oxidation because it affects the rate at which Zn vapors can react[36,18]. Many CVD ZnO experiments have been performed where oxygen concentrations have been the main variable. As a result, a variety of different ZnO nanostructures were created. The oxygen concentrations play a key role in determining different types of nanostructure formations causing some phases or different facets to preferentially grow. Generally, oxygen concentrations range, between 5-20%. At high temperature and high oxygen concentration conditions, the environment become metastable, allowing for growth in the ZB phase to become energetically favorable[74]. Tetrapods are commonly developed under these conditions. For slightly lower temperature and oxygen concentrations, ZnO heterogeneous WZ growth in the $[10\bar{1}0]$ or $[2\bar{1}\bar{1}0]$ direction is more favorable. Growth in theses directions produces nanostructures such as ribbons and sheets. These facets are seen in figure 1.10[15]. At lower temperatures and oxygen flow concentrations, WZ nanowires grown in the [0001] direction are the most favorable because basal plane has the lowest surface energy.

Ultimately, crystal growth cannot occur unless a thermodynamically favorable environment is created. Conditions must be met so that there is an energy advantage for the desired reaction to occur. For certain reactions to occur, temperature and pressure can be adjusted to lower the Gibb's free energy and achieve a $\Delta G<0$[20].

The basics of deposition growth require materials in the vapor phases to condense into liquid or solid phases at lower temperature reaction regions or make contact with a substrate with lower surface energy. The reactants are transported by convective or diffusive transport in the reaction zone. In the vapor transport, there may be gas phase reactions. Eventually, the primed reactants will reach the substrate surface. At the surface, there will be a chemical and physical adsorption. At a certain point, there will be surface reaction, which will lead to the formation of a film. Any volatile byproducts will be desorbed and transported away from the reaction zone through convective or diffusive transport.

The initial deposition is known as nucleation[66]. The conditions for nucleation require a favorable thermodynamic environment that can also energetically overcome the barrier of forming nuclei. There are two types of nucleation: homogenous and heterogenous nucleation. Homogenous nucleation requires nuclei to form in vapor before it is deposited on the surface.

Upon deposition on the substrate, the newly formed nuclei will have an epitaxial relationship with the substrate. Homogenous nucleation requires more energy to overcome the barrier to form nuclei than heterogenous nucleation. Heterogenous nucleation occurs when nuclei form on an existing substrate surface. The substrate significantly lowers the energetic barrier for nucleation. Depending on the substrate, the newly deposited film/nanostructures can be grown epitaxially, meaning that newly formed material will take on the lattice parameters in the transverse direction of the substrate.

For uniform deposition, gas transport control is very important. To control the deposition rate, it is imperative to control gas flow rates. However, the appropriate flow rate is difficult to determine[94]. At high flow rates, there is a lot of turbulence; at low flow rates, laminar flow rates are produced. The flux of vapor to the surface is determined as F_1 which can be defined as:

$$F_1 = h_G \times (C_G - C_S)$$

where h_G is known as the gas phase mass transport coefficient, C_G is the gas concentration, and C_S is the surface concentration on surface. The gas phase mass transport coefficient be further broken down as the quotient of the diffusion constant of gas, D, and boundary border thickness, δ:

$$h_G = D/\delta$$

The diffusion constant of gas can be broken down as :

$$D = D_0 \frac{T^{3/2}}{P}$$

where D_0 is maximum diffusion coefficient, T is the chamber's temperature, and P is the chamber's pressure. The boundary layer thickness, δ, can also be broken down as a function of distance:

$$\delta_S(x) = \left(\frac{\mu x}{\rho U}\right)^{1/2}$$

where x is distance traveled, ρ is the gas density, U is the velocity, and μ is the viscosity of the gas flow.

To calculate the amount of material that reacts with the surface, the term reaction flux, F_2, is used and can be defined as

$$F_2 = k_S \times C_S$$

where $k_{S,}$ is the surface reaction rate. When these two are combined, the deposition rate or growth velocity, v, can be determined:

$$v = \frac{F}{N} = \frac{C_g}{\frac{1}{h_G} + \frac{1}{k_S}}$$

where F is the overall net flux and N is the is the atomic density of deposited material.

Based on these factors, there exist two types of limited cases for deposition: reaction limited growth and mass transport limited growth. Generally, at high T, deposition is dominated by mass transport limitations: $R \propto T^{3/2}$. However at lower T, the deposition case is surface reaction limited: $R \propto exp\left(\frac{-E}{RT}\right)$. This can be seen in the Deposition Rate versus Temp curve[95].

For mass transport limited growth, the surface reaction rate is much higher than the gas phase mass transport coefficient where:

$$k_S >> h_G$$

Since k_S is generally high, crystal growth is limited by the material transport to the substrate. Unlike k_S, h_G is not affected by temperature, however, h_G is limited at higher temperature. Crystals that are produced by mass transport limited growths tend to have non-uniform film growth, thus, gas dynamics and reaction chamber designs are important[96].

In reaction limited growth the gas phase mass transport coefficient is much greater than the surface reaction rate where:

$$h_G >> k_S$$

The growth of crystals is controlled by processes on the surface such as: adsorption, decomposition, surface migration, chemical reactions, and desorption of products. All of these processes contribute to the surface reaction rate, k_S. If k_S is low, crystals will grow slowly. The growth rate of crystals can be increased with temperature increase because k_S is highly temperature dependent. For most precision thin film growths such as epitaxial growth, reaction limited growth is often preferred despite the slow growth process. In most cases, it is desired to have reaction limited growth where there is an ample supply of gas transport. To increase the transport coefficient, the pressure should be lowered and the gas flow should be increased. Thus, based on these parameters, it is important for CVD systems to have good vacuum to limit the mean free path and impingement rate of transported materials.

For ZnO deposition growth, films, bulk crystals, and nanostructures can be developed through CVD. Very often for nanowire growth, catalysts are used to help decrease the surface energy for adsorption to help increase the surface reaction. In 1964, Wagner and Ellis introduced a mechanism called Vapor-Liquid-Solid (VLS)[97]. In this growth mechanism, a liquid metal catalyst is used to adsorb vapors. Upon supersaturation of the liquid, the will be axial crystal growth at the liquid solid interface. Similarly, ZnO can be grown through a vapor-solid-solid (VSS) process where a metal alloy composite is used to adsorb vapors. Interestingly, ZnO nanostructures can also be created catalyst-free through vapor solid (VS) growth. In VS growth, zinc and oxygen ions deposit directly on the existing ZnO structures.

Amongst these methods to grow ZnO nanostructures, VLS and VSS are the most popular method because metal catalysts can be introduced prior to the deposition. Catalysts act as nucleation sites and can be used for template growth. The metal catalysts that are generally used tend to be transition metals that have lower melting temperatures but have high evaporating temperatures. The catalyst is usually metal and lowers the surface energy to allow for easier adsorption of Zn vapors. Upon supersaturation, the Zn will deposit at the liquid/solid catalyst and solid ZnO interface. Soon afterwards, it is quickly oxidized under oxygen exposure. The process continues until either the catalyst vaporizes away or the Zn precursor is exhausted[98].

For ZnO vapor solid growth, a CVD system was set up. The system was based off the same tube furnace used for the vacuum thermal oxidation. The system was retrofitted with an oxygen inlet that extended into the tube to bypass the zinc evaporation source. The reaction would occur inside the hot zone. No substrate temperature manipulation was used. The system allowed for uniform Zn evaporation while allowing for lower temperature VS growth. Different oxygen concentrations were used to observe specific nanostructures associated with the concentration.

1.5. Conclusion

The opportunity to develop a multifunctional material based upon two well-known materials: carbon fiber composites and ZnO nanostructures will open up an avenue of engineering research and applications. Carbon fiber is projected to be used for many structural applications that require a high strength to weight ratio. Multifunctional properties can be added through ZnO, which will help meet new requirements in safety, energy harvesting, and sensing. Amongst ZnO properties, the semiconductor properties, photoelectrochemical properties, and piezoelectric properties are the most heavily researched and useful properties. For this work, piezoelectricity has the most application for the hybridized ZnO nanostructures on carbon fiber.

Future work in this field can explore semiconductor properties and photoelectrochemical properties for added functionality to carbon fiber composites.

1.6. Figures and Tables

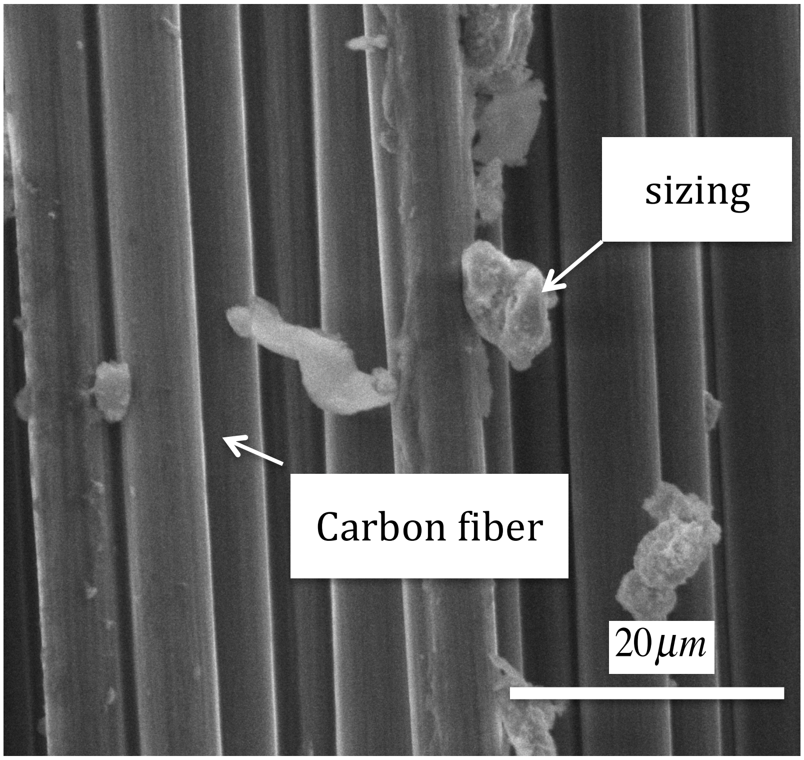

Figure 1.1: A SEM image of a Cytec T300 carbon fiber bundle, which is held together by sizing. The carbon fiber was measured to be 7µm in diameter.

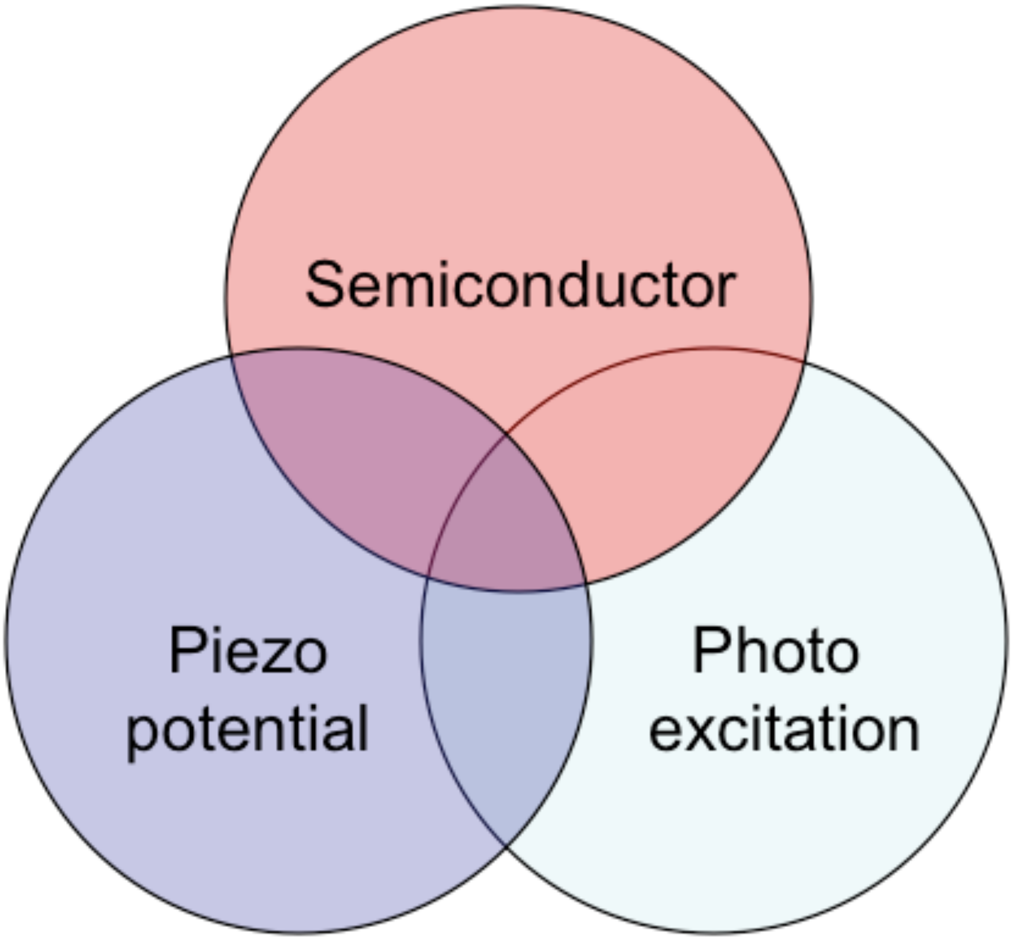

Figure 1.2[15]: ZnO's three most popular solid-state properties include its semiconductor, piezo potential, and photo excitation properties. Wang used this diagram to represent the relationship between the multifunctional opportunities for ZnO.

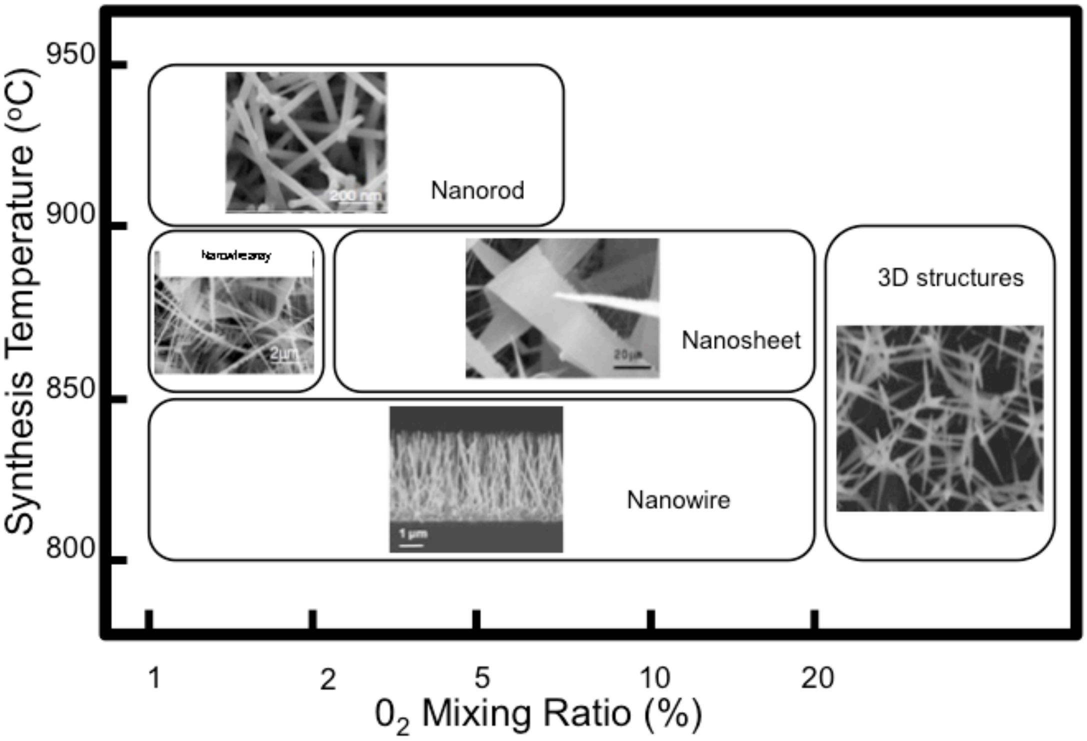

Figure 1.3[93]: ZnO nanostructure synthesis was demonstrated in a carbon thermal evaporation CVD experiment. The nanostructures' synthesis was heavily influenced by the synthesis and Oxygen flow mixing-ratio.

Assessed Zn-O Phase Diagram (Condensed System)

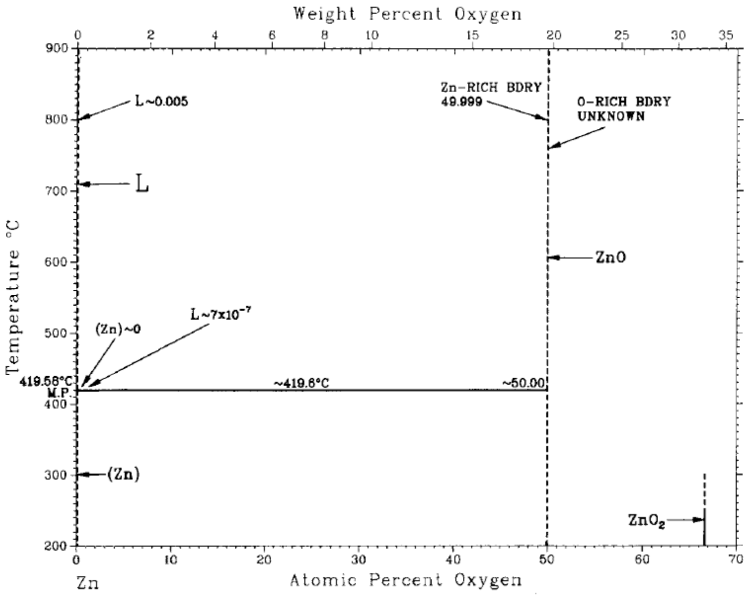

H.A. Wriedt, 1987.

Figure 1.4[38]: ZnO phase diagram shows a simple stoichiometry; ZnO is very stable.

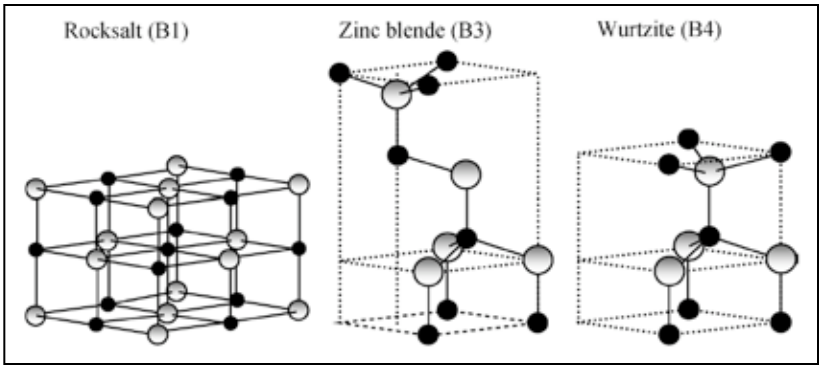

Figure 1..5[16]: ZnO can be rearranged into three phases: Rocksalt, Zinc-Blende, and Wurtzite.

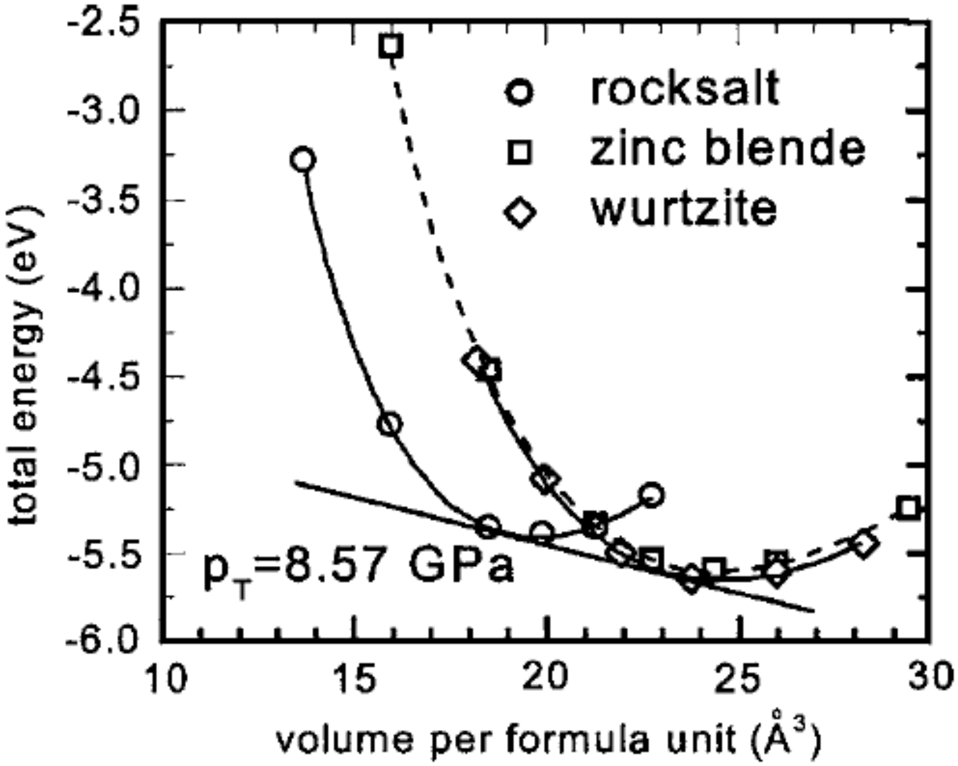

Figure 1..6[42]: Free energy vs volume per formula unit shows Wurtzite with the lowest free energy. The Zinc-blende can be achieved with a slight increase in free energy. For Rocksalt to be stable, high pressureis required.

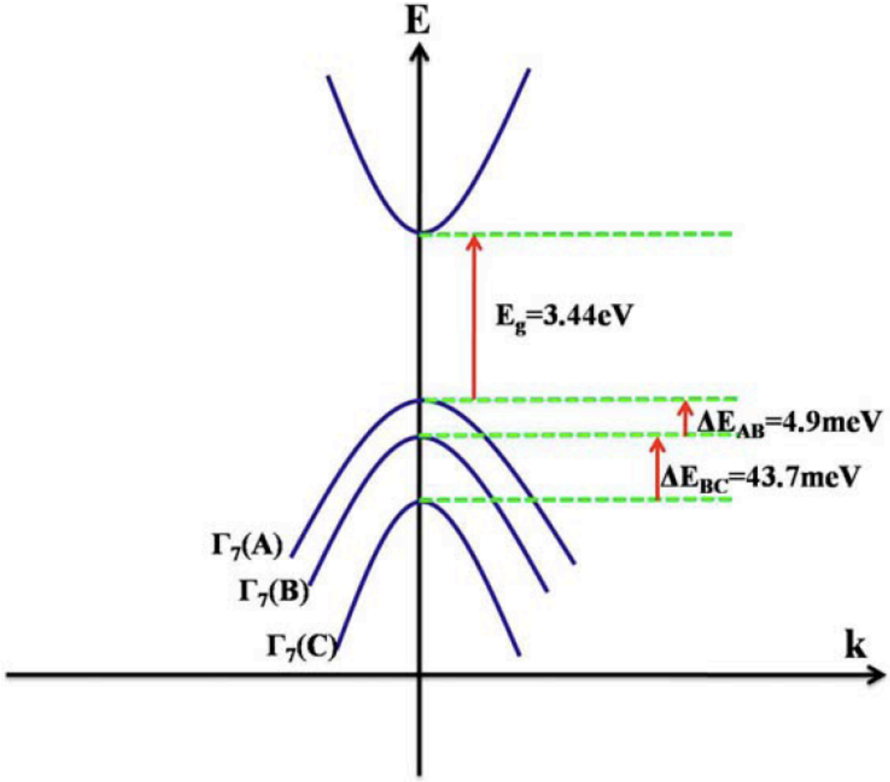

Figure 1.7[55]**: A diagram shows sub-band states (A,B,and C) in ZnO's valance band crystal field splitting .**

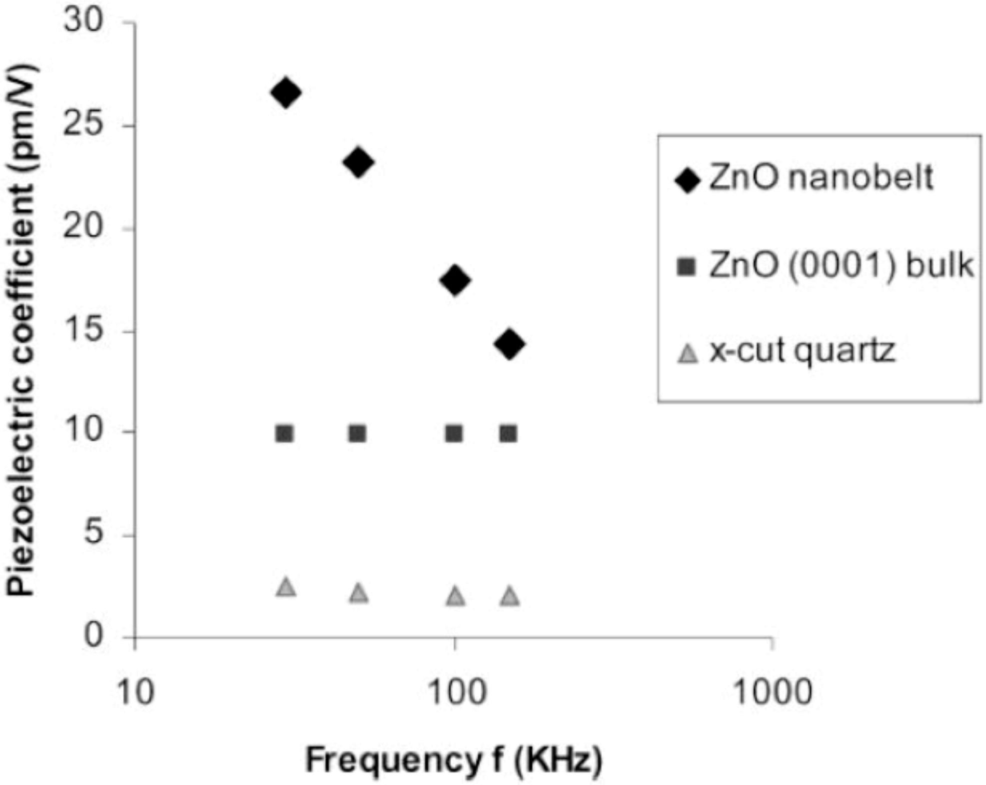

Figure 1.8[59]: ZnO nanobelts were shown to have higher piezoelectric coefficient at low frequencies.

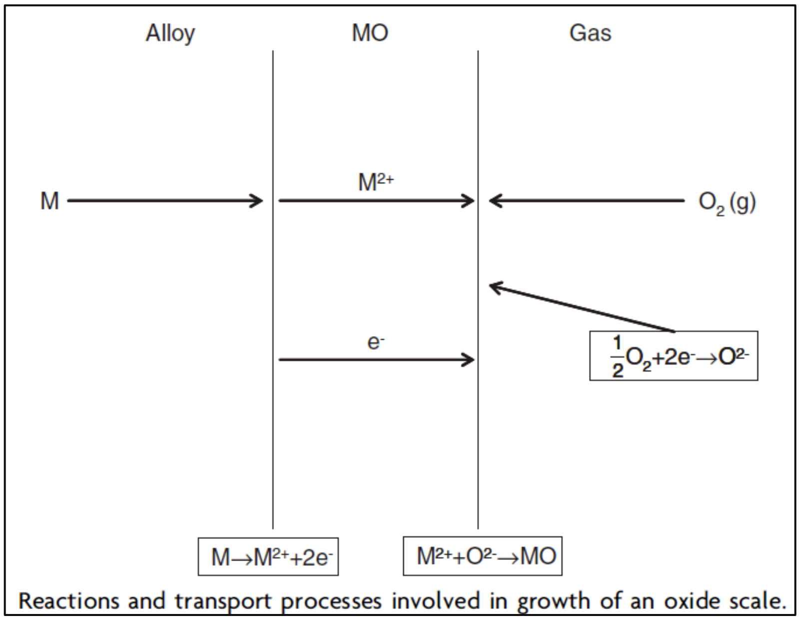

Figure 1.9[63]: This image shows a typical oxidation reaction diagram where the metal ions diffuse through the metal oxide towards the oxygen rich surface.

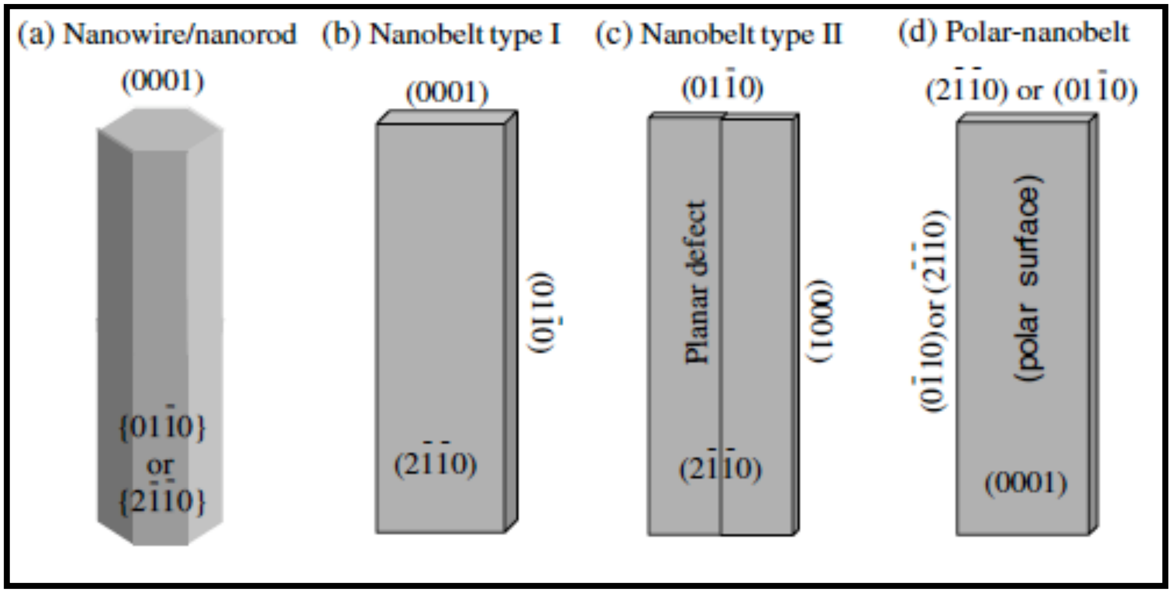

Figure 1.10[15]: Common anisotropic ZnO nanostructure are labeled with their respective facets.

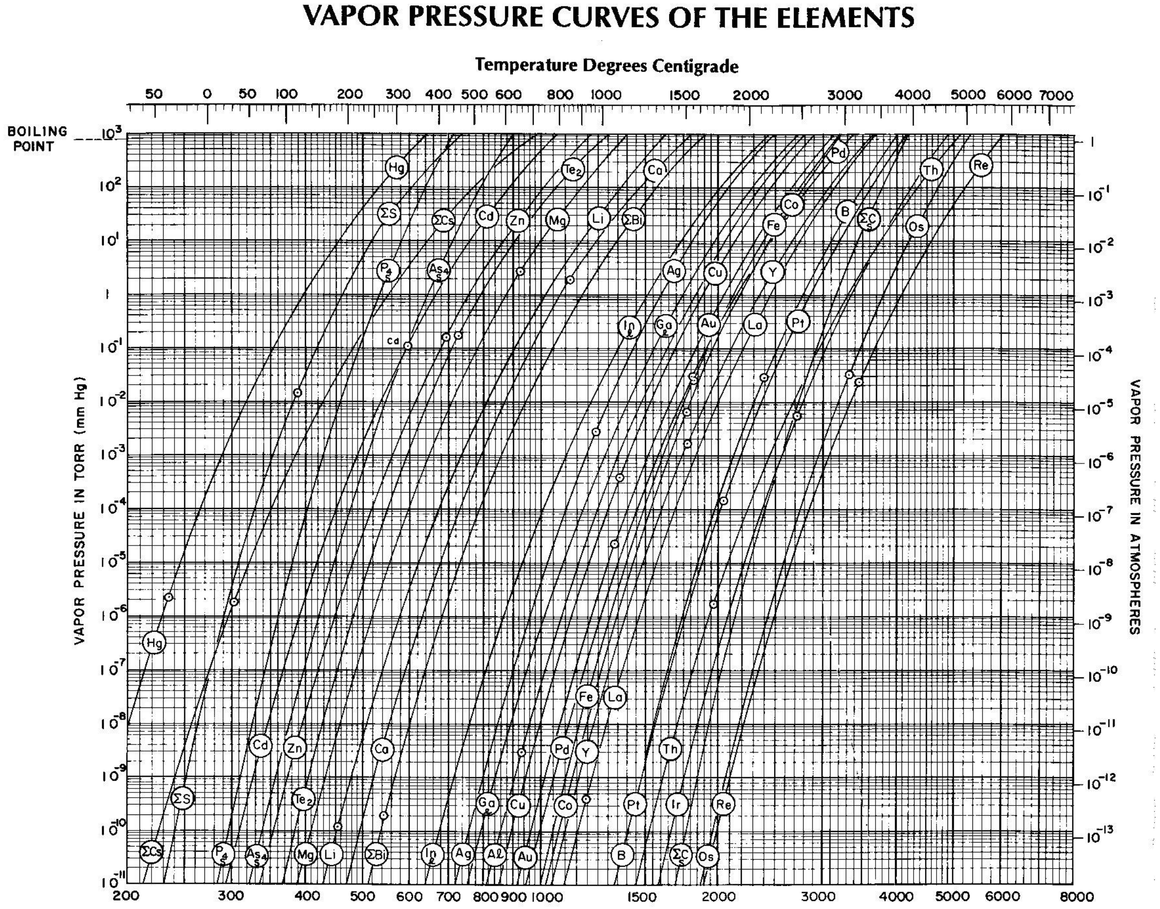

Figure 1.11[91]: A classic Honig Vapor Pressure Diagram of different elements shows that Zn has a high vapor pressure at low in relation to other elements

Table 1.1[26]: Properties of Different Carbon Fiber

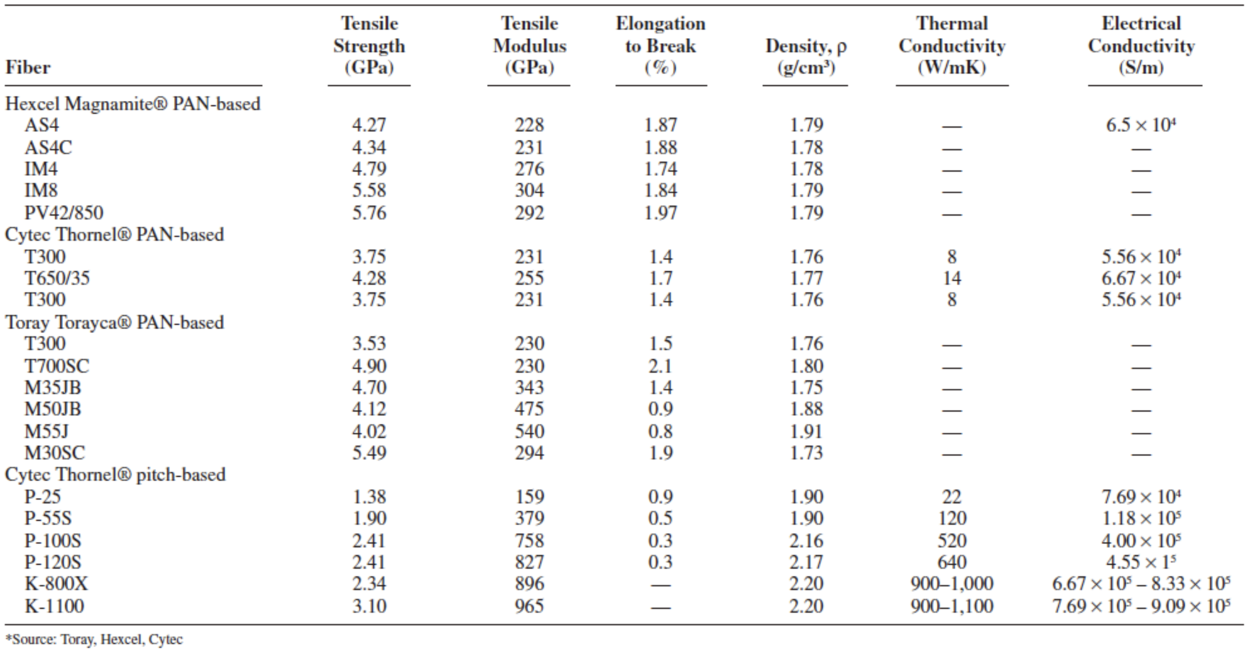

Fiber	Tensile Strength (GPa)	Tensile Modulus (GPa)	Elongation to Break (%)	Density, ρ (g/cm³)	Thermal Conductivity (W/mK)	Electrical Conductivity (S/m)
Hexcel Magnamite® PAN-based						
AS4	4.27	228	1.87	1.79	—	6.5×10^4
AS4C	4.34	231	1.88	1.78	—	—
IM4	4.79	276	1.74	1.78	—	—
IM8	5.58	304	1.84	1.79	—	—
PV42/850	5.76	292	1.97	1.79	—	—
Cytec Thornel® PAN-based						
T300	3.75	231	1.4	1.76	8	5.56×10^4
T650/35	4.28	255	1.7	1.77	14	6.67×10^4
T300	3.75	231	1.4	1.76	8	5.56×10^4
Toray Torayca® PAN-based						
T300	3.53	230	1.5	1.76	—	—
T700SC	4.90	230	2.1	1.80	—	—
M35JB	4.70	343	1.4	1.75	—	—
M50JB	4.12	475	0.9	1.88	—	—
M55J	4.02	540	0.8	1.91	—	—
M30SC	5.49	294	1.9	1.73	—	—
Cytec Thornel® pitch-based						
P-25	1.38	159	0.9	1.90	22	7.69×10^4
P-55S	1.90	379	0.5	1.90	120	1.18×10^5
P-100S	2.41	758	0.3	2.16	520	4.00×10^5
P-120S	2.41	827	0.3	2.17	640	4.55×1^5
K-800X	2.34	896	—	2.20	900–1,000	$6.67 \times 10^5 - 8.33 \times 10^5$
K-1100	3.10	965	—	2.20	900–1,100	$7.69 \times 10^5 - 9.09 \times 10^5$

*Source: Toray, Hexcel, Cytec

Table 1.2: Basic ZnO properties[16]*

Chemical Name	**Zinc Oxide**
Chemical Formula	ZnO
Molecular Weight	81.38 g/mole
Melting point/boiling point (decomposes)	1975 C
Specific Gravity	5.607 (water=1)
Density	5.606 g/cm3
Appearance	White
Band gap	3.37eV
Refractive Index	2.0041

*ZnO properties are based off of the wurtzite crystal structure in (298K)

1.7. References:

1. Wang, Z. L.; Kang, Z. C., *Functional and smart materials: structural evolution and structure analysis*. Springer: 1998.
2. Mohammadi, F.; Khan, A.; Cass, R. B. In *Power generation from piezoelectric lead zirconate titanate fiber composites*, Materials Research Society Symposium Proceedings, Cambridge Univ Press: 2003; pp 263-270.
3. Dastjerdi, R.; Montazer, M., A review on the application of inorganic nano-structured materials in the modification of textiles: focus on anti-microbial properties. *Colloids and Surfaces B: Biointerfaces* **2010,** *79* (1), 5-18.
4. Shim, B. S.; Chen, W.; Doty, C.; Xu, C.; Kotov, N. A., Smart electronic yarns and wearable fabrics for human biomonitoring made by carbon nanotube coating with polyelectrolytes. *Nano letters* **2008,** *8* (12), 4151-4157.
5. Callister, W. D., Introduction to materials science and engineering. *John Wiley, New York, 1991) p* **2000,** *420*.
6. Gibson, R. F., A review of recent research on mechanics of multifunctional composite materials and structures. *Composite structures* **2010,** *92* (12), 2793-2810.
7. Nakamura, Y.; Katogi, S., Technology Trends and Future History of Semiconductor Packaging Substrate Material.
8. Falaki, H.; Mahajan, R.; Kandula, S.; Lymberopoulos, D.; Govindan, R.; Estrin, D. In *Diversity in smartphone usage*, Proceedings of the 8th international conference on Mobile systems, applications, and services, ACM: 2010; pp 179-194.
9. Park, Y.; Chen, J. V., Acceptance and adoption of the innovative use of smartphone. *Industrial Management & Data Systems* **2007,** *107* (9), 1349-1365.
10. Verkasalo, H.; López-Nicolás, C.; Molina-Castillo, F. J.; Bouwman, H., Analysis of users and non-users of smartphone applications. *Telematics and Informatics* **2010,** *27* (3), 242-255.
11. Hitchins, D. K., *Systems engineering: a 21st century systems methodology*. John Wiley & Sons: 2008.
12. Bakis, C.; Bank, L. C.; Brown, V.; Cosenza, E.; Davalos, J.; Lesko, J.; Machida, A.; Rizkalla, S.; Triantafillou, T., Fiber-reinforced polymer composites for construction-state-of-the-art review. *Journal of Composites for Construction* **2002,** *6* (2), 73-87.
13. MInus, M.; Kumar, S., The processing, properties, and structure of carbon fibers. *Jom* **2005,** *57* (2), 52-58.
14. Brown, M. E., ZnO-Rediscovered. **1957**.
15. Wang, Z. L., Zinc oxide nanostructures: growth, properties and applications. *Journal of Physics: Condensed Matter* **2004,** *16* (25), R829-R858.
16. Özgür, Ü.; Alivov, Y. I.; Liu, C.; Teke, A.; Reshchikov, M.; Doğan, S.; Avrutin, V.; Cho, S.-J.; Morkoc, H., A comprehensive review of ZnO materials and devices. *Journal of applied physics* **2005,** *98* (4), 041301.

17. Janotti, A.; Van de Walle, C. G., Fundamentals of zinc oxide as a semiconductor. *Reports on Progress in Physics* **2009,** *72* (12), 126501.

18. Park, J.-H.; Choi, Y.-J.; Park, J.-G., Synthesis of ZnO nanowires and nanosheets by an O< sub> 2</sub>-assisted carbothermal reduction process. *Journal of Crystal Growth* **2005,** *280* (1), 161-167.

19. Zha, M.; Calestani, D.; Zappettini, A.; Mosca, R.; Mazzera, M.; Lazzarini, L.; Zanotti, L., Large-area self-catalysed and selective growth of ZnO nanowires. *Nanotechnology* **2008,** *19* (32), 325603.

20. Chang, P.-C.; Fan, Z.; Wang, D.; Tseng, W.-Y.; Chiou, W.-A.; Hong, J.; Lu, J. G., ZnO nanowires synthesized by vapor trapping CVD method. *Chemistry of materials* **2004,** *16* (24), 5133-5137.

21. Unalan, H. E.; Wei, D.; Suzuki, K.; Dalal, S.; Hiralal, P.; Matsumoto, H.; Imaizumi, S.; Minagawa, M.; Tanioka, A.; Flewitt, A. J., Photoelectrochemical cell using dye sensitized zinc oxide nanowires grown on carbon fibers. *Applied Physics Letters* **2008,** *93* (13), 133116.

22. Skandani, A. A.; Masghouni, N.; Case, S.; Leo, D.; Al-Haik, M., Enhanced vibration damping of carbon fibers-ZnO nanorods hybrid composites. *Applied Physics Letters* **2012,** *101* (7), 073111.

23. Masghouni, N.; Al-Haik, M. In *Vibration Damping Enhancement of Fiber Reinforced Polymer Composites With Surface Grown Zinc Oxide Nanorods*, ASME 2013 International Mechanical Engineering Congress and Exposition, American Society of Mechanical Engineers: 2013; pp V009T10A037-V009T10A037.

24. Skandani, A. A.; Masghouni, N.; Al-Haik, M., Superior Damping of Hybrid Carbon Fiber Composites Grafted by ZnO Nanorods. In *Topics in Modal Analysis, Volume 7*, Springer: 2014; pp 187-193.

25. Endo, M., Grow carbon fibers in the vapor phase. *Chemtech* **1988,** *18* (9), 568-576.

26. Chand, S., Review carbon fibers for composites. *Journal of Materials Science* **2000,** *35* (6), 1303-1313.

27. Roberts, T., Rapid growth forecast for carbon fibre market. *Reinforced Plastics* **2007,** *51* (2), 10-13.

28. Gao, P. X.; Wang, Z. L., Nanoarchitectures of semiconducting and piezoelectric zinc oxide. *Journal of Applied Physics* **2005,** *97* (4), 044304.

29. Wang, Z. L.; Kong, X. Y.; Ding, Y.; Gao, P.; Hughes, W. L.; Yang, R.; Zhang, Y., Semiconducting and piezoelectric oxide nanostructures induced by polar surfaces. *Advanced Functional Materials* **2004,** *14* (10), 943-956.

30. Kamat, P. V.; Patrick, B., Photophysics and photochemistry of quantized zinc oxide colloids. *The journal of physical chemistry* **1992,** *96* (16), 6829-6834.

31. Koch, U.; Fojtik, A.; Weller, H.; Henglein, A., Photochemistry of semiconductor colloids. Preparation of extremely small ZnO particles, fluorescence phenomena and size quantization effects. *Chemical Physics Letters* **1985,** *122* (5), 507-510.

32. Coskun, C.; Look, D. C.; Farlow, G. C.; Sizelove, J., Radiation hardness of ZnO at low temperatures. *Semiconductor science and technology* **2004,** *19* (6), 752.

33. Ryu, Y.; Lee, T.-S.; Lubguban, J. A.; White, H. W.; Kim, B.-J.; Park, Y.-S.; Youn, C.-J., Next generation of oxide photonic devices: ZnO-based ultraviolet light emitting diodes. *Applied Physics Letters* **2006,** *88* (24), 241108.

34. Kong, X. Y.; Ding, Y.; Wang, Z. L., Metal−Semiconductor Zn−ZnO Core−Shell Nanobelts and Nanotubes. *The Journal of Physical Chemistry B* **2003,** *108* (2), 570-574.

35. Liu, J.; Zhang, Z.; Su, X.; Zhao, Y., From zinc nanowires to zinc oxide nanowires: a low substrate-temperature approach. *Journal of Physics D: Applied Physics* **2005,** *38* (7), 1068-1071.

36. Park, J.-H.; Park, J.-G., Synthesis of ultrawide ZnO nanosheets. *Current Applied Physics* **2006,** *6* (6), 1020-1023.

37. Zanotti, L.; Calestani, D.; Villani, M.; Zha, M.; Zappettini, A.; Paorici, C., Vapour‐phase growth, purification and large‐area deposition of ZnO tetrapod nanostructures. *Crystal Research and Technology* **2010,** *45* (6), 667-671.

38. Wriedt, H., The O− Zn (Oxygen-Zinc) system. *Journal of Phase Equilibria* **1987,** *8* (2), 166-176.

39. Phillips, J., *Bonds and bands in semiconductors*. Elsevier: 2012.

40. Ashrafi, A.; Jagadish, C., Review of zincblende ZnO: stability of metastable ZnO phases. *Journal of Applied Physics* **2007,** *102* (7), 071101.

41. Recio, J.; Blanco, M.; Luaña, V.; Pandey, R.; Gerward, L.; Olsen, J. S., Compressibility of the high-pressure rocksalt phase of ZnO. *Physical Review B* **1998,** *58* (14), 8949.

42. Jaffe, J.; Hess, A., Hartree-Fock study of phase changes in ZnO at high pressure. *Physical Review B* **1993,** *48* (11), 7903.

43. Dulub, O.; Diebold, U.; Kresse, G., Novel stabilization mechanism on polar surfaces: ZnO (0001)-Zn. *Physical review letters* **2003,** *90* (1), 016102.

44. Sekiguchi, T.; Miyashita, S.; Obara, K.; Shishido, T.; Sakagami, N., Hydrothermal growth of ZnO single crystals and their optical characterization. *Journal of Crystal Growth* **2000,** *214*, 72-76.

45. Sakagami, N.; Yamashita, M.; Sekiguchi, T.; Miyashita, S.; Obara, K.; Shishido, T., Variation of electrical properties on growth sectors of ZnO single crystals. *Journal of crystal growth* **2001,** *229* (1), 98-103.

46. Li, W.-J.; Shi, E.-W.; Zhong, W.-Z.; Yin, Z.-W., Growth mechanism and growth habit of oxide crystals. *Journal of crystal growth* **1999,** *203* (1), 186-196.

47. Gerward, L.; Olsen, J. S., The high-pressure phase of zincite. *Journal of synchrotron radiation* **1995,** *2* (5), 233-235.

48. Browne, M. E.; Browne, M. E., *Schaum's Outlines: Physics for Engineering and Science*. McGraw-Hill: 2010.

49. Ozgur, U.; Hofstetter, D.; Morkoc, H., ZnO devices and applications: a review of current status and future prospects. *Proceedings of the IEEE* **2010,** *98* (7), 1255-1268.

50. Look, D. C.; Reynolds, D. C.; Sizelove, J.; Jones, R.; Litton, C. W.; Cantwell, G.; Harsch, W., Electrical properties of bulk ZnO. *Solid state communications* **1998,** *105* (6), 399-401.

51. Nickel, N. H.; Terukov, E., *Zinc oxide-a material for micro-and optoelectronic applications*. Springer: 2005.

52. Soci, C.; Zhang, A.; Xiang, B.; Dayeh, S. A.; Aplin, D.; Park, J.; Bao, X.; Lo, Y.-H.; Wang, D., ZnO nanowire UV photodetectors with high internal gain. *Nano letters* **2007,** *7* (4), 1003-1009.

53. Hwang, D.-K.; Oh, M.-S.; Lim, J.-H.; Choi, Y.-S.; Park, S.-J., ZnO-based light-emitting metal-insulator-semiconductor diodes. *Applied Physics Letters* **2007,** *91* (12), 121113-121113-3.

54. Tomlins, G. W., Routbort, H. L., Mason, T. O., , Zinc self-diffusion, electrical properties, and defect structure of undoped, single crystal zinc oxide. *Journal of Applied Physics* **2000,** *87* (11).

55. Jagadish, C.; Pearton, S. J., *Zinc oxide bulk, thin films and nanostructures: processing, properties, and applications*. Elsevier Science: 2011.

56. Li, M.-K.; Wang, D.-Z.; Ding, S.; Ding, Y.-W.; Liu, J.; Liu, Z.-B., Synthesis and properties of aligned ZnO microtube arrays. *Applied surface science* **2007,** *253* (9), 4161-4165.

57. Yang, Y. H.; Chen, X. Y.; Feng, Y.; Yang, G. W., Physical Mechanism of Blue-Shift of UV Luminescence of a Single Pencil-Like ZnO Nanowire. *Nano letters* **2007,** *7* (12), 3879-3883.

58. Zhang, D.; Gao, R.; Ma, H., Burstein shift and UV photoresponse in IBAD-deposited transparent conducting ZnO films. *Thin Solid Films* **1997,** *295* (1), 83-86.

59. Zhao, M.-H.; Wang, Z.-L.; Mao, S. X., Piezoelectric characterization of individual zinc oxide nanobelt probed by piezoresponse force microscope. *Nano letters* **2004,** *4* (4), 587-590.

60. Zhao, Y.; Li, D.; Ma, X.; Yang, D., The effect of the ramping rate on oxygen precipitation and the denuded zone in heavily doped Czochralski silicon. *Journal of Physics: Condensed Matter* **2004,** *16* (9), 1539-1545.

61. Tzou, H.; Natori, M., Piezoelectric materials and continua. *in-Chief: Simon, Ed., ed Oxford: Elsevier* **2001**, 1011-1018.

62. Chan, H. L. W.; Unsworth, J., Simple model for piezoelectric ceramic/polymer 1-3 composites used in ultrasonic transducer applications. *Ultrasonics, Ferroelectrics and Frequency Control, IEEE Transactions on* **1989,** *36* (4), 434-441.

63. Young, D. J., High temperature oxidation and corrosion of metals: Corrosion series. **2008**, 81-96.

64. Pierson, H. O., *Handbook of chemical vapor deposition: principles, technology and applications*. William Andrew: 1999.

65. Baruah, S.; Dutta, J., Hydrothermal growth of ZnO nanostructures. *Science and Technology of Advanced Materials* **2009,** *10* (1), 013001.

66. Porter, D. A.; Easterling, K. E., *Phase Transformations in Metals and Alloys, (Revised Reprint)*. CRC press: 1992.

67. Philibert, J., One and a half century of diffusion: Fick, Einstein, before and beyond. *Diffusion Fundamentals* **2005,** *2* (1), 1-10.

68. Fick, A. E., *Poggendorff's Annalen* **1885,** *94* (59).

69. Kim, K. S., *Ph.D. thesis, Massachusetts Institute of Technology* **1971**.

70. Smeltzer, W.; Young, D., Oxidation properties of transition metals. *Progress in Solid State Chemistry* **1975,** *10*, 17-54.

71. Shen, G.; Bando, Y.; Lee, C.-J., Synthesis and Evolution of Novel Hollow ZnO Urchins by a Simple Thermal Evaporation Process. *The Journal of Physical Chemistry B* **2005,** *109* (21), 10578-10583.

72. Rackauskas, S.; Nasibulin, A. G.; Jiang, H.; Tian, Y.; Statkute, G.; Shandakov, S. D.; Lipsanen, H.; Kauppinen, E. I., Mechanistic investigation of ZnO nanowire growth. *Applied Physics Letters* **2009,** *95* (18), 183114.

73. Khanlary, M. R.; Vahedi, V.; Reyhani, A., Synthesis and characterization of ZnO nanowires by thermal oxidation of Zn thin films at various temperatures. *Molecules* **2012,** *17* (5), 5021-9.

74. Ding, Y.; Lin Wang, Z.; Sun, T.; Qiu, J., Zinc-blende ZnO and its role in nucleating wurtzite tetrapods and twinned nanowires. *Applied physics letters* **2007,** *90* (15), 153510-153510-3.

75. Pan, Z. W.; Dai, Z. R.; Wang, Z. L., Nanobelts of semiconducting oxides. *Science* **2001,** *291* (5510), 1947-9.

76. Huang, M. H.; Mao, S.; Feick, H.; Yan, H.; Wu, Y.; Kind, H.; Weber, E.; Russo, R.; Yang, P., Room-temperature ultraviolet nanowire nanolasers. *Science* **2001,** *292* (5523), 1897-1899.

77. Park, J.-H.; Choi, H.-J.; Choi, Y.-J.; Sohn, S.-H.; Park, J.-G., Ultrawide ZnO nanosheets. *Journal of Materials Chemistry* **2004,** *14* (1), 35-36.

78. Tang, H.; Zhu, L.; Ye, Z.; He, H.; Zhang, Y.; Zhi, M.; Yang, F.; Yang, Z.; Zhao, B., Synthesis of two kinds of ZnO nanostructures by vapor phase method. *Materials Letters* **2007,** *61* (4), 1170-1173.

79. Tang, H.; Chang, J. C.; Shan, Y.; Ma, D. D. D.; Lui, T.-Y.; Zapien, J. A.; Lee, C.-S.; Lee, S.-T., Growth mechanism of ZnO nanowires via direct Zn evaporation. *Journal of Materials Science* **2008,** *44* (2), 563-571.

80. Yi, G.-C.; Wang, C.; Park, W. I., ZnO nanorods: synthesis, characterization and applications. *Semiconductor Science and Technology* **2005,** *20* (4), S22.

81. Calestani, D.; Zha, M.; Mosca, R.; Zappettini, A.; Carotta, M.; Di Natale, V.; Zanotti, L., Growth of ZnO tetrapods for nanostructure-based gas sensors. *Sensors and Actuators B: Chemical* **2010,** *144* (2), 472-478.

82. Polley, T.; Carter, W.; Poker, D., Deposition of zinc oxide thin films by combustion CVD. *Thin Solid Films* **1999,** *357* (2), 132-136.

83. Polley, T.; Carter, W., Zone model for zinc oxide deposited by combustion chemical vapor deposition. *Thin Solid Films* **2001,** *384* (2), 177-184.

84. Zhang, Y.; Mu, J., Controllable synthesis of flower-and rod-like ZnO nanostructures by simply tuning the ratio of sodium hydroxide to zinc acetate. *Nanotechnology* **2007,** *18* (7), 075606.

85. Kim, Y.-J.; Lee, J.-H.; Yi, G.-C., Vertically aligned ZnO nanostructures grown on graphene layers. *Applied Physics Letters* **2009,** *95* (21), 213101.

86. Pan, Z. W.; Mahurin, S. M.; Dai, S.; Lowndes, D. H., Nanowire array gratings with ZnO combs. *Nano letters* **2005,** *5* (4), 723-727.

87. Liu, Y.; Gorla, C.; Liang, S.; Emanetoglu, N.; Lu, Y.; Shen, H.; Wraback, M., Ultraviolet detectors based on epitaxial ZnO films grown by MOCVD. *Journal of Electronic Materials* **2000,** *29* (1), 69-74.

88. Park, J.-H.; Choi, H.-J.; Park, J.-G., Scaffolding and filling process: a new type of 2D crystal growth. *Journal of Crystal Growth* **2004,** *263* (1–4), 237-242.

89. Atkins, P.; De Paula, J., *Elements of physical chemistry*. Oxford University Press: 2012.

90. DeHoff, R., *Thermodynamics in materials science*. CRC Press: 2006.

91. Honig, R. E.; Kramer, D. A., VAPOR-PRESSURE DATA FOR THE SOLID AND LIQUID ELEMENTS. **1970**.

92. Lim, Y.; Park, J.; Hong, S.-T.; Kim, J., Carbothermal synthesis of ZnO nanocomb structure. *Materials Science and Engineering: B* **2006,** *129* (1), 100-103.

93. Park, J.-H.; Choi, Y.-J.; Park, J.-G., Evolution of nanowires, nanocombs, and nanosheets in oxide semiconductors with variation of processing conditions. *Journal of the European Ceramic Society* **2005,** *25* (12), 2037-2040.

94. Carlsson, J.-O., Processes in interfacial zones during chemical vapour deposition: Aspects of kinetics, mechanisms, adhesion and substrate atom transport. *Thin solid films* **1985,** *130* (3), 261-282.

95. Carlsson, J.-O.; Jansson, U., Progress in chemical vapor deposition. *Progress in Solid State Chemistry* **1993,** *22* (4), 237-292.

96. Krishna, R.; Wesselingh, J., The Maxwell-Stefan approach to mass transfer. *Chemical Engineering Science* **1997,** *52* (6), 861-911.

97. Wagner, R.; Ellis, W., Vapor‐liquid‐solid mechanism of single crystal growth. *Applied Physics Letters* **1964,** *4* (5), 89-90.

98. Givargizov, E. I., Highly anisotropic crystals. **1987**.

Chapter 2: Evolvement of ZnO Hybrid Nanostructures through Zinc Thermal Oxidation

2.1. Introduction

Like most anisotropic materials, ZnO has been investigated extensively and synthesized for its unique properties and micro/nano structures[1,2]. ZnO nanostructures include wires[3,4,5], tubes[6,7], sheets[8,9,10], and hierarchical structures[11]. Zinc oxide's wide band gap, piezo potential and wide range of micro/nanostructures[12] has allowed this material to be used in a wide array applications[13,14]. Current goals for ZnO are aimed to understand quantum size affects, to increase the surface to volume ratio, and to develop hybrid nanostructures that combine multiple nanostructures. The quantum size effect has been shown to increase the number of carriers causing a blue shift in catholuminesence when structures reach below 50nm[15]. A higher surface to volume ratio has been shown to increase photo absorption, catalytic activity, and compliancy for piezoelectricity[12]. This work focuses on the development of a hybrid nanostructure though transient thermal conditions during synthesis.

Most of the available ZnO synthesis techniques such as: thermal oxidation[16,17], chemical vapor deposition (CVD)[18], hydrothermal processing[19], thermal evaporation[20], and carbothermal reduction[21], are performed through isothermal processes. Isothermal processes are designed to grow specific nanostructures. However, to develop ZnO hybrid nanostructures, transient parameters are required.

Thermal oxidation is a well-established ZnO fabrication technique and received a revival in attention for its ability to grow nanowires[22] at low cost and low temperatures. This technique is also versatile; modification can be made for transient parameter changes. Thermal oxidation experiments have been conducted in two primary ways[22a]: thermal oxidation at slow temperature rates (<5°C/min) and thermal oxidation at rapid temperature rates (>200°C/min). Not surprisingly, the results are different for both techniques because the heating rate affects the growth morphology. Thus for better control of ZnO morphology growth through thermal oxidation, heating rates must be controlled.

Zinc whiskers and nano structures will be used as starting materials for thermal oxidation. These structures can be synthesized through thermal evaporation followed by vapor transport. They are hexagonal closed packed materials with lattice parameters: a=2.66 Å and c=4.95 Å[23] . Through vapor deposition, performed in inert environment, zinc forms into wires and platelets[24,25]. Their size can be dictated by controlling the evaporation temperature and substrate temperature. At higher evaporation temperatures, zinc crystals form finer structures. Note in the case with substrate temperature, lower deposition temperatures allow for thin zinc structure formation, whereas elevated deposition temperatures promote the growth of zinc whiskers and larger zinc particles.

Using classic transition metal oxidation studies, the Zn/ZnO system can be easily explained[26]. Under an oxygen environment, transition metals almost instantaneously form an oxide layer between a few angstroms to thousands of angstroms thick. Zinc is no different; it develops an oxide layer almost immediately and will continue to grow through zinc interstitial diffusion. In low temperature environments, zinc surface atoms quickly oxidize and grow into an oxide film, but growth is effectively terminated until sufficient energy is provided for further Zn diffusion towards the surface. At higher temperatures, thermal oxidation causes the formation of oxide scales due to multiple ZnO nucleation sites. The introduction of grain boundaries provides more direct paths for zinc to migrate towards the surface. Oxidation can even occur above the melting temperature of Zn (420°C) where an oxide layer will form over molten Zn[27].

To synthesize a hybrid nanostructures, a thermal oxidation setup was assembled for stable and dynamic growth experiments. Zinc nano structures synthesized through zinc powder evaporation and condensation would serve as precursors for ZnO nanostructure synthesis. Zinc nanowires and platelets were synthesized in low temperature (~100°C) conditions and developed into ZnO microtubes upon oxygen exposure. Faceted zinc particles and whiskers were synthesized in higher temperature environments (~250°C); upon oxidation, ZnO nanowires and nanosheets were synthesized on the facets of the Zn precursor structures. Through a transient substrate heating experiment under thermal oxidation, a unique ZnO structure was observed. It combines a hexagonal microtube with highly organized nanowire and nanosheet branches. Growth mechanism interpretations for this structure are discussed.

2.2. Experimental Setup

To develop hybrid ZnO structures, independent heating for the source, transport region, and the substrate were combined in a thermal oxidation setup. The independent source and substrate heating take advantage of a large range of temperatures (source heating: up to 1000°C; and substrate heating: up to 350°C). Independent heating also allows a wide range of ramping temperature and cooling rates (up to 200°C/sec). A wide range of ramp rates for the source allows for continuous evaporation, burst or intermittent evaporation, and gradient evaporation. The independent stage heating for the substrate allows for heating experiments, heat treatments, and effective quenching.

This system's main body is composed of a 1" outer diameter quartz tube, housed inside a tube furnace, capable of reaching 950°C. High vacuum components and a mechanical rotary pump were used to achieve an ultimate vacuum of 2×10^{-3} torr. Mass flow controllers managed the system's transport gas and reactive gas pressures. The arrows inside the tube indicate the flow direction, which includes both the carrier gas (argon) and reactive gas (oxygen). The source (zinc) was placed inside an alumina tube wrapped in a tungsten filament. The substrate was seated on a heater assembled by an alumina platform and a NiCr filament. Thermocouples were attached to a LabVIEW data acquisition unit for the monitoring and recording of the source, furnace, and substrate temperatures. These combined components allowed our system to achieve high temperature, high vacuum, quick assembly, reduced experimental cycle time (2.5 hours/sample including cool down time), and electrical configuration flexibility.

The experiment was prepared with 0.2 grams of commercial 99.9% purity/100 mesh zinc powder placed in the alumina crucible. A RCA cleaned 0.5cm^2 Si (111) substrate was placed on the substrate heater. Both the crucible and the substrate were placed and housed in the quartz tube on opposite ends while being situated 1.5cm outside the furnace ends. This placement was crucial because it would keep the initial temperature settings of the crucible and the substrate consistent. The system was pumped down, followed by 10 minutes of nitrogen purging to stabilize the system and achieve 0.002 torr. (Despite these measures, oxygen would inevitably be present in our system.) Argon was then introduced at 133 standard cubic centimeters per minute (sccm) to be used as a transport vapor and elevate the pressure (P) to 0.300 torr. Finally, the furnace temperature (T_{fur}) was raised to 650°C at a rate of 35°C/min. Due to the furnace's radiative heat, the source temperature (T_{evap}) and substrate temperature (T_{sub}) reached 100°C before the Zn thermal evaporation. Once the furnace had reached 650°C, the independent heating source was heated to 700°C±10 to thermally evaporate Zn for 20 seconds and with a heating ramp rate of (55±5)°C/second to evaporate zinc for deposition. The independent controls allowed us to quickly turn on and off the zinc source by giving us a fast ramp rate period and a fast cool down period. Some variance was taken into consideration because the thermocouples are less stable at temperatures above 550^{o}C. Also Zn evaporation flux could not be measured.

Five different sets were produced in this experiment shown below in Table 1. Oxygen flow and substrate temperature were varied to produce Zn and ZnO micro and nanostructures. In the first two sets, A and B, only Zn deposition through thermal evaporation followed by vapor transport was performed on Si (111) substrates. No oxygen gas flow was provided. The substrate temperatures of Sets A and B were isothermally held at 100^{o}C and 250^{o}C respectively. After Zn deposition, the substrate temperature remained for 10 minutes before cooling. Sets A and B were designed to validate the system's capabilities and understand the temperature effect on Zn growth. These two temperatures would help create the lower and upper bounds for growth conditions.

In the next sets, 1 and 2, Zn was deposited on Si (111) substrates with temperatures of 100^{o}C and 250^{o}C respectively. After 20 seconds of zinc deposition, oxygen flow was immediately introduced at 10sccm for 10 minutes. According to the pressure gauge, the pressure increased to 440mTorr. The respective substrate temperatures were isothermally held during the 10-minute oxidation period. Set 1 and 2 would build upon the previous sets and observe the effect of oxidation on lower and upper temperature conditions.

Set 3 was designed to study the transient heating effect during oxidation. The substrate temperature started at 100^{o}C and heated until it reached 250^{o}C. For 20 seconds, Zn was deposited onto a Si (111) substrate heated to 100^{o}C (as Set 1). Oxygen flow at 10 sccm followed for 10 minutes. During the thermal oxidation period, the substrate was heated progressively in

20^{o}C/min increments until it reached 250^{o}C. The temperature remained constant at 250^{o}C for the final 2.5 minutes. Set 3 was designed to combine Set 1 and 2's growth conditions and explore possible combinations of ZnO nano morphologies developed specifically for the lower and upper bound temperatures.

The sets were characterized using the Nova Nano 230 Scanning Electron Microscopy (SEM) with Energy Dispersive x-ray Spectroscopy (EDS) for microstructure and chemical analysis. Detailed characterization was performed using the TF20 and Titan 300 kV Transmission Electron Microscopes (TEM) for further magnification and crystallographic inquiry. TEM sample preparation involved physically removing the Zn/ZnO particles from the Si substrates and collecting them onto TEM grids with a carbon support film.

2.3 Results and Discussion

The Zn/ZnO structures ranged in size and morphology due to the oxidation and substrate temperature parameters. All of the results are summarized below in Table 2. Sets A and B provided a basis of temperature effects on zinc morphologies. These results would assist Sets 1-3 observation of important key features such as morphology, dimension, surface features, and composition. Amongst these sets, only Set 3 utilized the full capabilities of our system. Through Set 3's transient thermal oxidation experiment, a hybrid nanostructure was produced. All the other sets' products were grown under isothermal conditions to help correlate established temperatures and oxygen flows with Zn/ZnO structures.

Set A, shown in Figure 1a, displayed a dense network of zinc wires and few amount of platelets with lengths measured up to 5μm and diameters ranging from 100nm to 400nm. The observation is in good agreement with the work done by Coleman[24] and Yan[23]. Coleman described the variation of Zn particles through thermal evaporation. Given our setup, some variance in Zn evaporation was taken into consideration because it was not possible to measure Zn evaporation flux. EDS results revealed that a small amount (1-3%) of oxygen was present in the Set. This is not surprising because the oxidation is a combination of our system's limited vacuum and atmospheric exposure before SEM and TEM characterization. As far as oxide formation over zinc nanowires, Yan showed that zinc oxide formation could occur at minimum oxygen levels.

Confirmation of this oxidation is shown using TEM analysis. Figure 1b shows a typical Zn wire and Figure 1c shows a typical platelet; both show thin oxide layers. Diffraction patterns were taken of each particle. Both revealed spots for hexagonal closed packed (HCP) metallic Zn and wurtzite (WZ) ZnO where the lattice parameters for Zn are: a=2.66Å and c=4.95Å; and parameters for ZnO (WZ) include: a=3.25Å and c=5.20Å[12]. The wire's diffraction pattern showed a foil direction of $[2\bar{1}\bar{1}0]$, indicating that the Zn wire grew in the [0001] direction. For the platelet, Figure 1c showed a [0001] foil direction of the platelet, indicating that the platelet grew in the $[2\bar{1}\bar{1}0]$ direction. Highlighted ZnO (WZ) and Zn (HCP) reflections of the wire include: (0002), $(0\bar{1}11)$, and $(01\bar{1}0)$; likewise, highlighted reflections for the platelet include $(11\bar{2}0)$, $(10\bar{1}0)$, and $(01\bar{1}0)$. The cell parameters of the oxide and the metallic show a 22% mismatch[12]. Yan also reported Zn and ZnO epitaxial relation was $(10\bar{1}0)Zn \parallel (10\bar{1}0)ZnO$ with an 18% mismatch.

Set B showed Zn plate-like particles, ranging from 1-5μm in diameter and 1-15 μm in length. Figure 2a shows that the majority of these structures were interconnected plate-like particles of zinc, but occasionally larger whiskers would appear. These larger structures also showcased well-defined hexagonal facets and slip planes. It appears that the substrate temperature played a role in particle morphology growth while also annealing the structures through surface rearrangement. The difference between Sets A and B can be explained by Givargizov[2] and Coleman[24]. Higher temperature of the substrate allowed the zinc to grow into larger, well-defined faceted particles and whiskers. Occasional smaller platelets, arrowed in Figure 2b, will branch from a larger particle.

Set 1 showed ZnO tubes. According to literature, zinc diffuses faster in zinc oxide than in oxygen diffusing into Zn. This difference in diffusion rates results in a Kirkendall effect: Zn diffusion into ZnO leads to void formation. Thus Zn wires develop into hollowed ZnO tubes[28]. As an oxide layer develops, Zn diffuses through the oxide and oxidizes as it reaches the surface. Through SEM analysis in Figure 3a, these morphologies were measured up to 5μm in length and 100 to 400nm in diameter.

The size of the particle morphologies is in good correlation between Set 1 and Set A because the substrate temperatures were both heated to 100°C. At higher magnification, Figure 3b shows rough surfaces of the particle morphologies, indicating that Zn wires were indeed oxidized. These particles were confirmed to be tubes under TEM observation shown in Figures 3c and 3d. In Figure 3c, multiple tubes are shown with metallic zinc cores. Under higher magnification, Figure 3d reveals an oxide thickness about 35 ± 15 nm, which is an order of magnitude greater than the ZnO layer observed in Set A. Figure 3e, shows the EDS spectra of Set 1 showing a non-stoichiometric ratio between the two elements. Between zinc and oxygen, EDS calculations showed $63 \pm 10\%$ zinc content compared to $37 \pm 10\%$ oxygen content. This validates the observation of the zinc cores from the earlier Figures. The existence of the zinc cores means that the oxidation was not completed for the given condition.

Set 2 produced ZnO particles after zinc deposition was followed by elevated temperature of 250°C and controlled oxidation. These particles had two noteworthy characteristics: first, the particles were larger particles (3±1μm) with defined facets; and second, highly oriented nanowires covered the surfaces of the particles. As expected, Set 2 correlates well to Set B, due to similar substrate temperature of 250°C. The size and the facet steps of the ZnO particles can be attributed to the elevated temperature that allowed zinc particles to grow and to anneal. Figure 4a shows the consistency in particle sizes (3μm in diameter) and is similar to Set B's particles. Under elevated temperature and oxidation, one would simply expect that all Zn oxidation would result in the formation of shells. However, higher magnification reveals nanowires covering well-defined facets (encircled in Figure 4b) of ZnO particles. All of these nanowires are highly oriented because they are normal to the facet surface. The nanowires were measured to be 10 nm in width and 100 nm in length, spaced around 10-30 nm apart. This gives a high density of 2500 nanowires/μm^2. Further magnification showed highly organized nanowires and nanosheets (Figure 4c); these morphologies were unexpected. An interpretation of the nanosheets formation is provided later in Set 3 discussion.

ZnO nanowire growth mechanism could be explained through a series of events shown schematically in Figure 4d. After Zn was deposited on the Si substrate, the particles were allowed to grow and develop into well-defined facets upon a heated substrate. Controlled oxygen flow was then introduced causing many ZnO grains to form on the Zn faceted surface. The elevated temperature and oxygen presence at the ZnO surface created a mechanical and chemical driving force for zinc migration towards the surface. Zinc migration towards the surface is represented by the void formation in Figure 4d. Zinc reached the surface in two ways: some zinc would interstitially diffuse through the ZnO grains and some would diffuse through the newly formed ZnO grain boundaries. For each grain boundary, a new ZnO grain would form at the surface. Literature suggests that these newly formed ZnO grains continue to grow in the basal direction, perpendicular to the surface[29-30]. Growth in the basal plane allows these surface grains grow quicker than the grains below in the direction away from the surface. These grains eventually become nanowires because the remaining metallic zinc continues to diffuse towards the surface through the grain boundary. Upon reaching the bottom of the newly formed surface grains, zinc interstitially diffuses in the grains' basal direction. As the Zn reaches the grains' surface, oxidation occurs, effectively adding more material to the new grains. ZnO nanowires are then created through the repeated zinc interstitial diffusion and oxidation steps. The process continues until the metallic zinc supply, beneath the oxide, is exhausted.

The nanowire growth direction perpendicular ZnO particle with well-defined facets was caused by the combination of an elevated substrate temperature, faceted surfaces, grain boundary diffusion, and surface grains growing in the basal direction. The high density of nanowires was caused by the formation of many ZnO grain boundaries during initial oxidation. Many reported works have shown ZnO nanowires formed through thermal oxidation such as Yuvaraj[29] and Yu[30], but none have demonstrated nanowires grown perpendicularly to the annealed facet orientations.

The nanosheets between the nanowires were unexpected because the nanosheets were grown through thermal oxidation, not chemical vapor deposition. In reported CVD experiments[8,9,10], the gaps between the nanowires created favorable deposition sites. The close proximity of the nanowires would trap zinc vapors to create a localized supersaturated zinc vapor environment. These reports also emphasize that sheet formation is also highly influenced by the ratio of reactant gases and transport gases. In our case, the 10 sccm of oxygen with 133 sccm of argon was supplied. In our thermal oxidation setup, zinc vapor was not intentionally supplied. However, when our stage was heated, our deposited zinc produced zinc vapor.

According to Gibbs Thomson potential[27], high zinc vapor partial pressure was produced when the zinc was nearly exhausted. Thus at the final stage of oxidation, the conditions were suitable for nanosheet formation. There was zinc vapor, the correct oxygen/argon flow ratio, and gaps between the nanowires to create a supersaturated environment.

Set 3 exhibited a new ZnO hybrid structure showcasing hexagonal microtubes with highly organized nanowire and nanosheet branches. Though microtubes, nanowires and nanosheets are well known, the combination of these structures has not yet been reported, regardless of synthesis method. The hybrid structures' dimensions range between 200-400nm in diameter and 0.5-15µm in length, which can be seen in figure 5a. At higher magnification (Figure 5b) cross sections of Set 3 products could be observed. The hybrid structures exhibit hexagonal characteristics with nano-branches growing from the hexagonal vertices. TEM analysis, in Figure 5c, reveals that the ZnO hybrid structures were hexagonal tube with organized nanowires and nanosheets along the hexagonal vertices. The nanowires were then measured to be 10-30 nm in diameter and 100-300 nm in length. Under higher magnification shown in Figure 5d, closer observation was made of the nanosheets. The nanosheets appeared to be thinner and shorter than the nanowires. The sheets are 5-10 nm in thickness, 100-200 nm in width, and 50-200 nm in length. Comparison between the nanowire and nanosheet was straightforward because the nanosheets are situated in-between the nanowires and are more transparent than the nanowires. Selected area diffraction (area is circled) was taken of the particle showing a zone axis of $[\bar{1}2\bar{1}3]$ with highlighted reflections of $(0\bar{1}11)$, $(\bar{1}010)$ and $(\bar{1}10\bar{1})$. Two important observations were noted in this diffraction pattern: no metallic zinc reflections were identified and satellite spots beyond the first order diffraction indicate that the particle is not a single crystal.

In order to explain the ZnO hybrid structure's growth mechanism from Set 3, interpretations of Sets 1 and 2's results are combined. From Sets 1's results, it was shown that low that temperature oxidation encourages tubes formation. Set 2's results show higher temperature oxidation encourages nanowire and nanosheet formation. Under Set 3's heating experiment, both conditions were met starting with low temperature oxidation. As a result, hybrid structures were created featuring tubes with nanowires and nanosheets can be formed. The evolvement of the ZnO hybrid structure is shown in Figure 6a where a zinc wire transforms into a ZnO tube with highly organized nanowire and nanosheet branches. Figure 6a includes images of a zinc wire from Set A, tubes from Set 1, and the hybrid structure from Set 3. A schematic (Figure 6b) is provided for better clarity of the hybrid ZnO structure evolvement.

The transformation began when initial zinc wires quickly developed into ZnO tube upon low temperature oxidation. The dimensions of Set A, Set 1, and Set 3's products were found to be similar both in diameter and length. As temperature increased, the tubes diameter began take a hexagonal shape, which is common for ZnO tubes. During this process, cracks were formed at the ZnO tube's hexagonal vertices. These cracks would allow trapped metallic zinc to migrate towards the surface through grain boundary diffusion. Upon reaching the surface, the zinc would quickly oxidize and develop into ZnO nanowires. According to the Gibbs Thomson potential, zinc vapor was produced as the metallic zinc became exhausted. These zinc vapors would condense with oxygen at the corners of the nanowires bases and the tube. As more vapor condensed, sheets would form between the nanowires. Nanowires and nanosheets are characteristic of higher temperature (250^{o}C) oxidation as seen in Set 2. As result of this heating experiment, ZnO hybrid structures were produced, showcasing hexagonal tubes with highly organized nanowires and nanosheet branches.

2.4. Conclusion

Interest in hybrid nanostructures is beginning to develop because these structures have multiple morphologies that have different properties. A new hybrid ZnO micro/nanostructure was developed through substrate heating in a Zn thermal oxidation experiment. This structure is composed of a ZnO hexagonal tube with highly organized nanowire and nanosheet branches. Nanosheets formed between the nanowires when the zinc source was nearly exhausted. Though there are ZnO hybrid structures in literature, none show the combination of a hexagonal tube with highly organized nanowire and nanosheet branches. These nanosheets are not common for thermal oxidation experiments, but given the available zinc vapor, oxygen flow, and small gaps between nanowires, the conditions became suitable for nanosheet formation. These hybrid structures can be used as more effective catalyst for their significant increased in surface area to volume ratio. In addition, these hybrid structures can be possibly used as effective light filters because the combination of a larger tube, nanowire, and nanosheet will allow for a larger spectrum of photo absorption. As the synthesis of hybrid ZnO nanostructures continues to develop, future work must focus on correlating specific structures to specific properties.

2.5. Figures and Tables

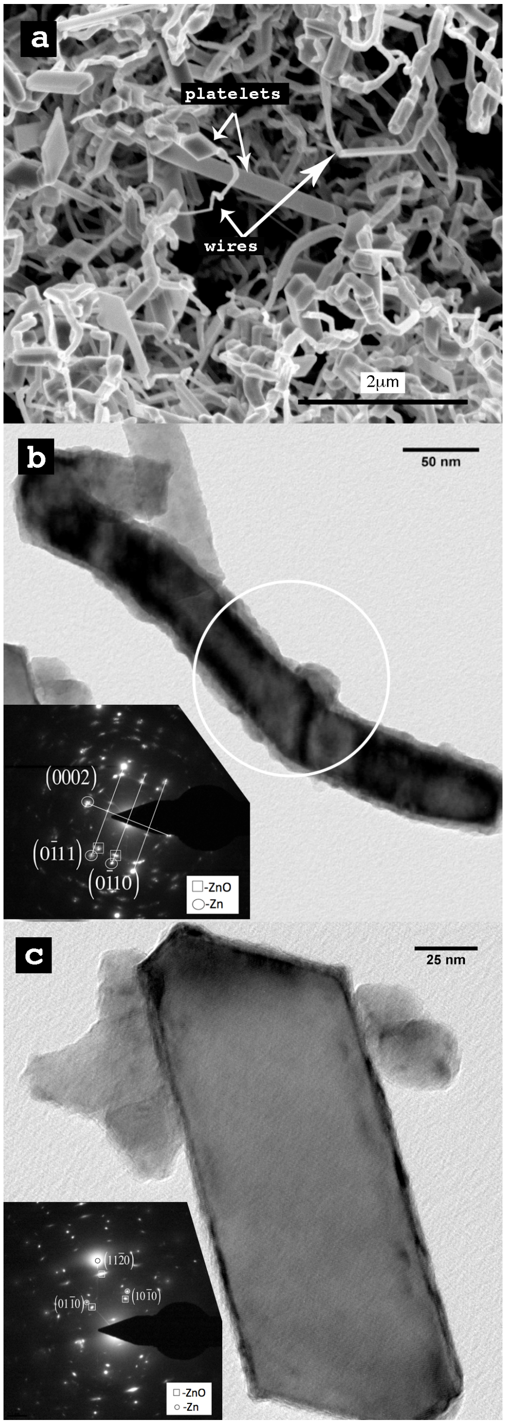

Figure 2. 1: Zn particle morphologies (Set A) synthesized via thermal evaporation followed by vapor transport. (a) SEM image shows zinc nanowires and nano-platelet (arrows). (b) TEM of zinc nanowire, with selected area diffraction. (c) TEM image of a zinc nano-platelet and its related selected area diffraction. The aligned Zn (HCP) and ZnO (WZ) patterns show the epitaxial formation of a ZnO film on a Zn platelet.

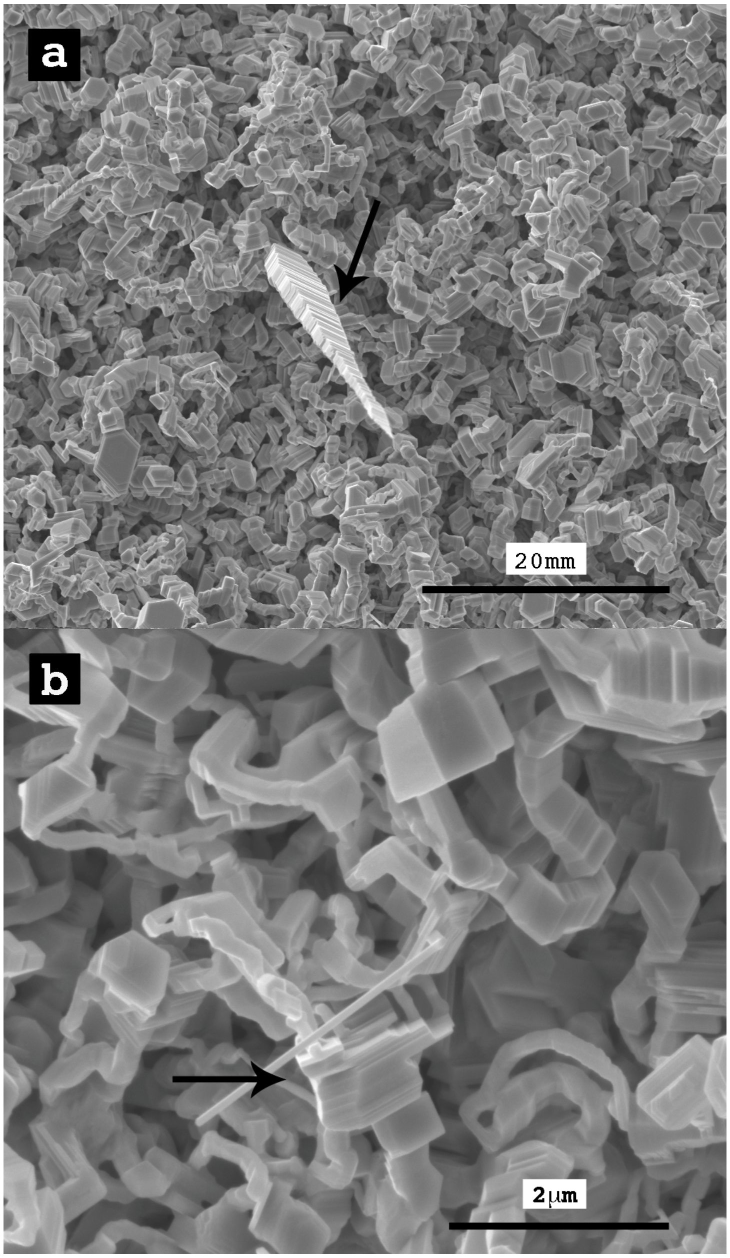

Figure 2. 2: Set B shows zinc deposition followed by a 10-minute heat treatment at 250°C. These products are about **7** ± **2** times larger than Sdet A's products. a) Zn morphologies shows interconnected hexagonal zinc plates and occasional zinc whiskers (arrowed). b) Higher magnification shows well-defined facets on the zinc particles and a small, elongated platelet branch (arrowed).

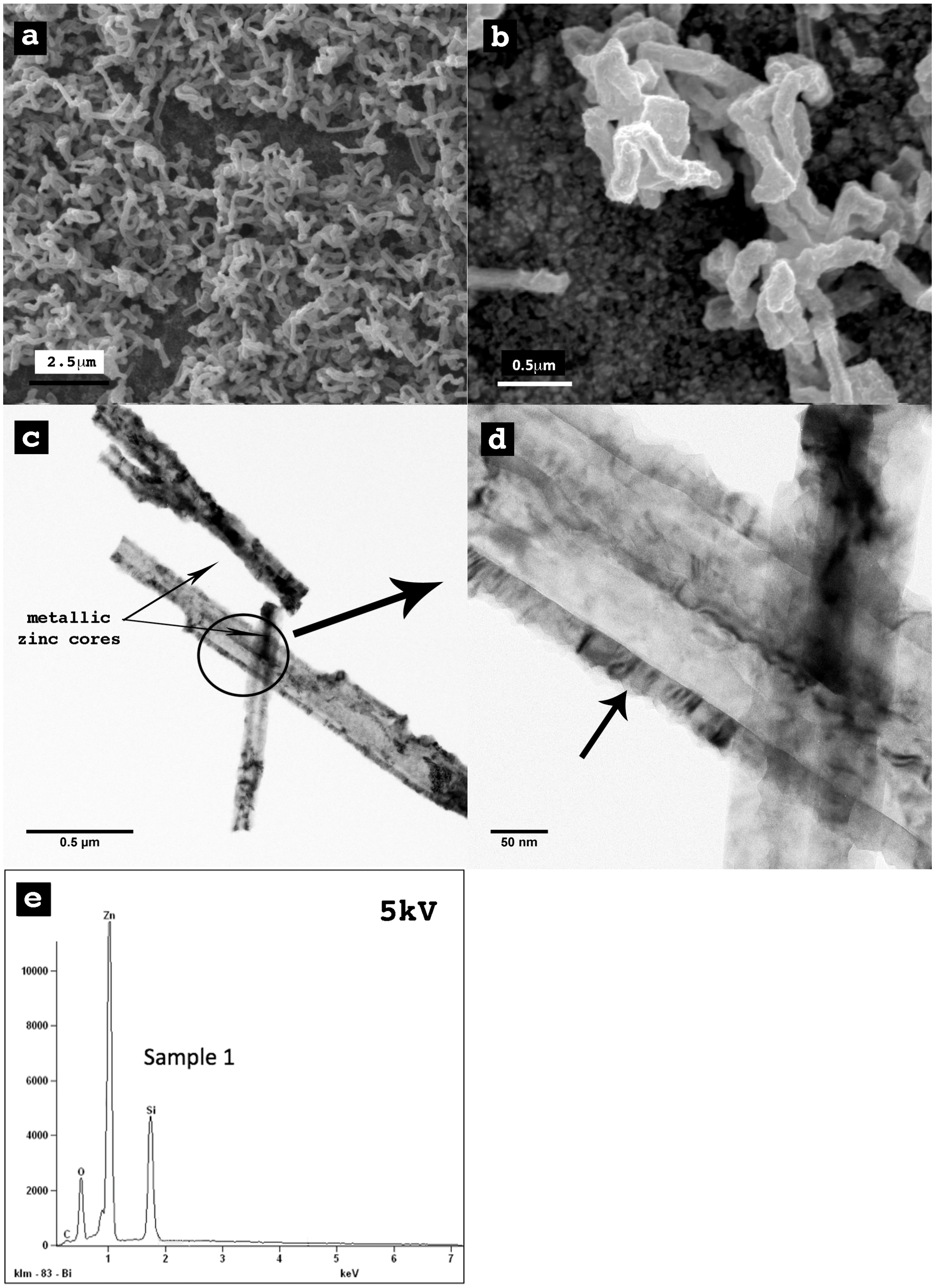

Figure 2. 3: Zn and ZnO particles morphologies (Set 1) formed after from Zn particle morphologies were exposed to controlled oxygen flow. (a) Wire morphologies are similar to Set A's wires; no platelets were found in Set 1. (b) Higher magnification shows particle's rough surfaces compared to Set A's particles. (c) TEM image shows zinc oxide tubes; dark metallic zinc cores (arrowed) can be seen. (d) Higher magnification showing the oxide layer (arrowed). (e) EDS spectra (taken at 5kV) show a non-stoichiometric ratio of zinc and oxygen.

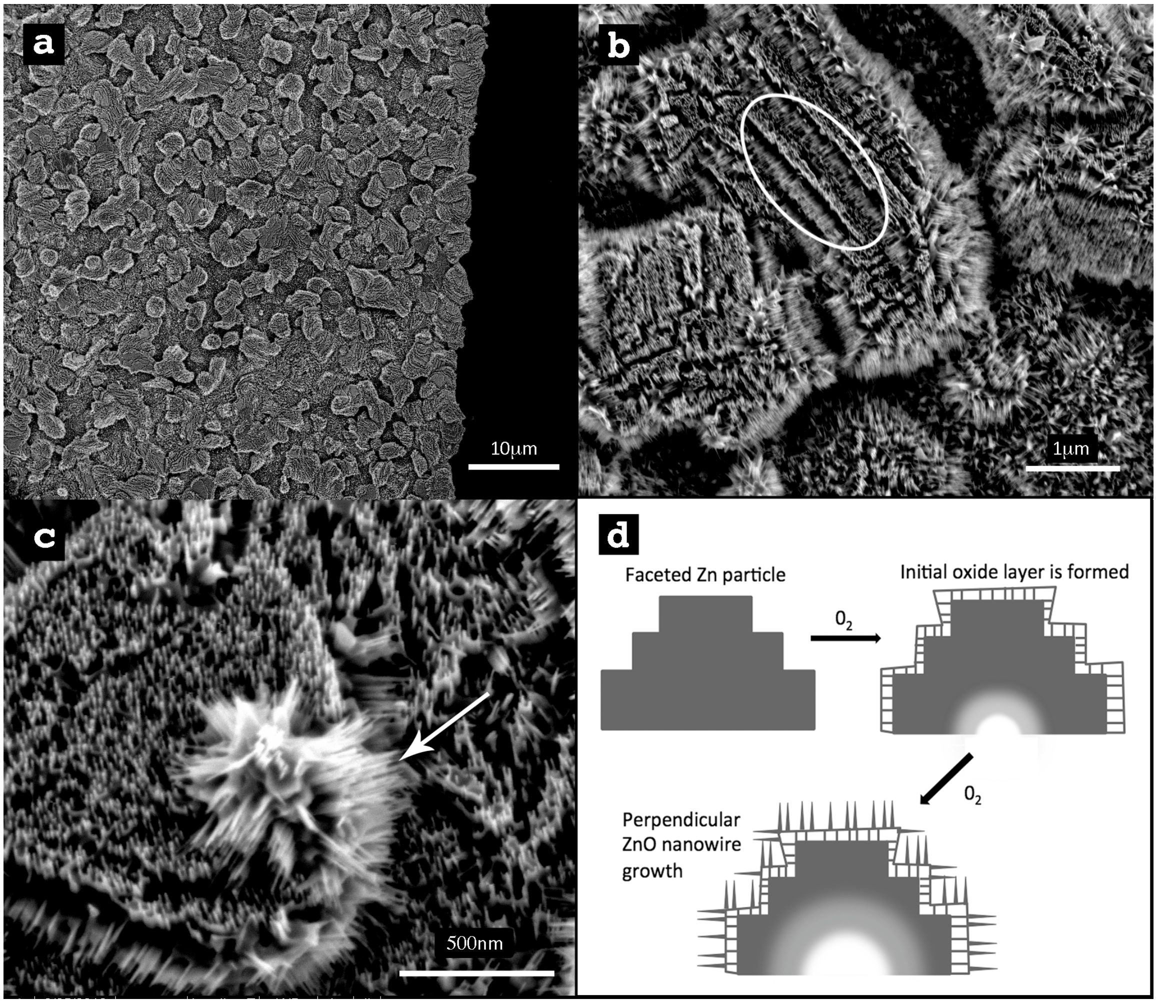

Figure 2. 4: Zinc deposition (Set 2) followed by a 250°C heat treatment and oxidation. (a) The sizes of Set 2's particle morphologies are similar to Set B's particles morphologies. (b) Higher magnification shows highly oriented zinc oxide nanowires perpendicular to well-defined faceted surfaces (circled). (c) Higher magnification shows nanosheets (arrowed) between the nanowires. (d) Schematic of a faceted Zn particle developing a non-uniform ZnO shell. Nanowires are developed through Zn diffusion through ZnO grain boundaries and Zn interstitial diffusion in the newly formed, surface ZnO grains (crystal).

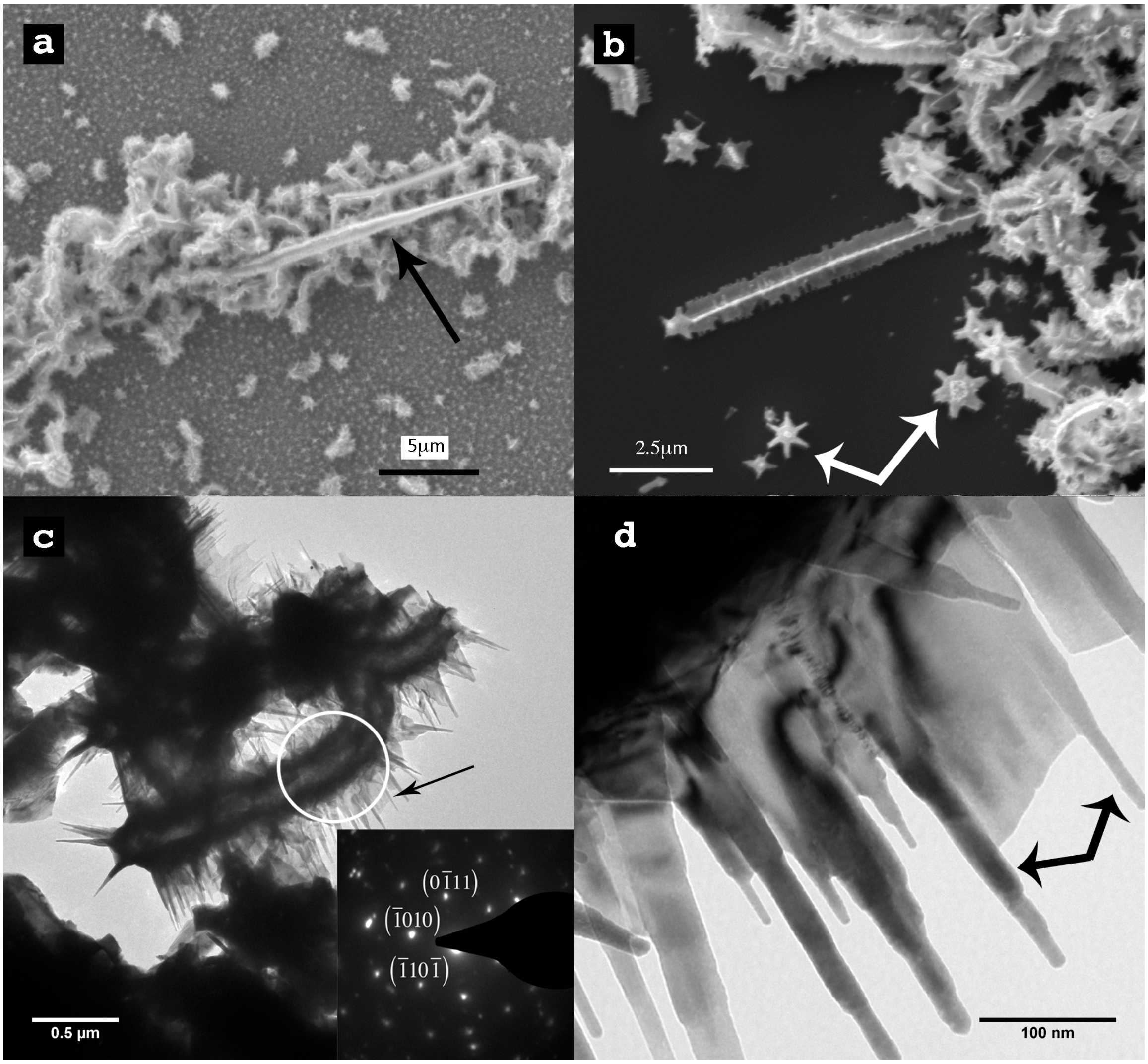

Figure 2. 5: Set 3 shows zinc oxide tubes with highly organized nanowires and nanosheets, developed though VCTO. (a) SEM shows ZnO particle morphologies with similar dimensions to Set A and Set 1, but also features long whiskers (arrowed). (b) Higher magnification shows hexagonal cross section of the observed particle morphologies. (c) TEM image shows the ZnO particle morphology is a tube with highly organized nanowires and nanosheets. No reflection corresponding to metallic zinc patterns were identified in the selected area diffraction (circled). Area of investigated nanowires and nanosheet is arrowed. (d) Higher magnification shows a nanosheet grown between nanowires (arrowed).

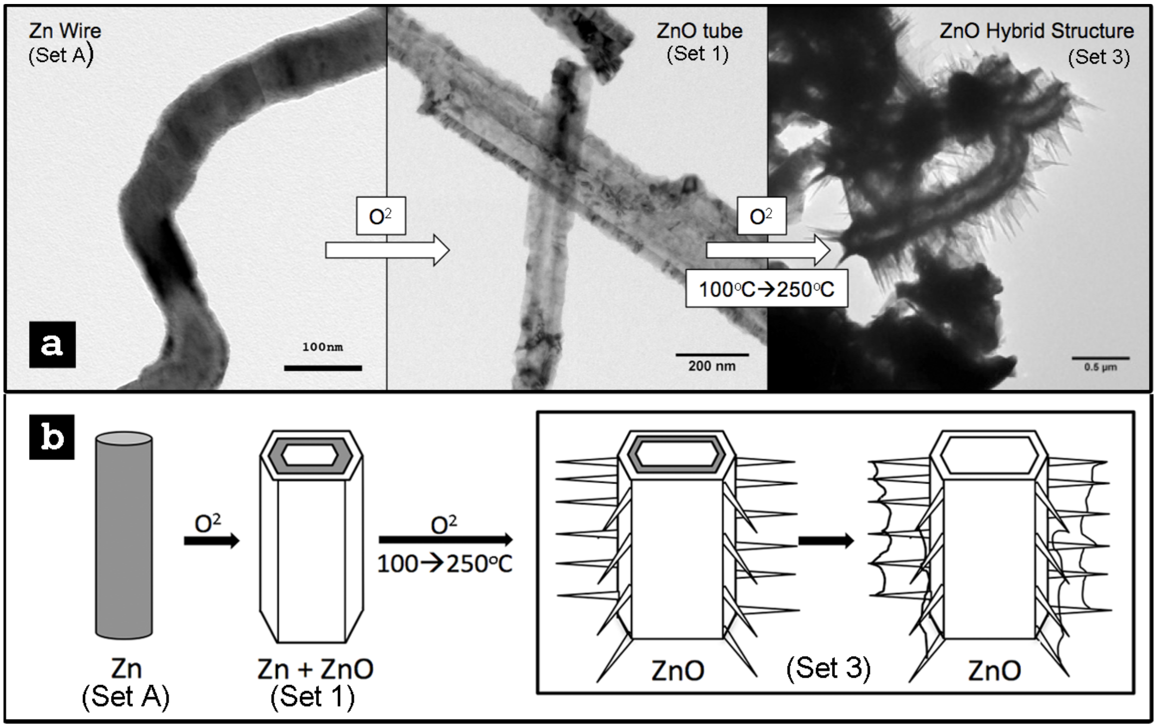

Figure 2. 6: The evolvement of ZnO hybrid structure during thermal Oxidation. a) A Zinc wire (from Set A) transforms into a ZnO tube (from Set 1) during low temperature oxidation and becomes a ZnO hybrid structure (from Set 3). b) A schematic of hybrid ZnO morphology evolution: a zinc wire transforming into a tube with highly organized nanowires and nanosheets.

Table 2. 1: Experimental Parameters

Set	T_{evap} (C)	Deposition time (sec)	T_{fur} (C)	P_1 (mTorr)	T_{sub} (C)	Oxygen flow after deposition (sccm)	P_2 (mTorr)	Oxygen flow time (min)
A	700	20	650	300	100	0	300	10
B	700	20	650	300	250	0	300	10
1	700	20	650	300	100	10	440	10
2	700	20	650	300	250	10	440	10
3	700	20	650	300	100->250 (20oC/min)	10	440	10

P_1 = Pressure before Zn deposition

P_2 = Pressure during oxygen flow (after deposition)

Table 2. 2: The results display the EDS results and the Morphology of the Zn/ZnO structures for each set.

Set	Material	Morphology
A	Zn + (1-3% ZnO)	Wires[23] and few platelets[24]
B	Zn + (1-3% ZnO)	Faceted particles[2] and few whisker[24]
1	ZnO + Zn	Microtubes[6,7] with metallic Zn core
2	ZnO	Faceted particles with Nanowires[22] and nanosheets[8,9,10]
3	ZnO	Microtubes with nanowires and nanosheets

2.6 References

1. Vayssieres, L.; Keis, K.; Lindquist, S.-E.; Hagfeldt, A., Purpose-Built Anisotropic Metal Oxide Material:□ 3D Highly Oriented Microrod Array of ZnO. *The Journal of Physical Chemistry B* **2001,** *105* (17), 3350-3352.
2. Givargizov, E. I., Highly anisotropic crystals. **1987**.
3. Yang, P.; Yan, H.; Mao, S.; Russo, R.; Johnson, J.; Saykally, R.; Morris, N.; Pham, J.; He, R.; Choi, H. J., Controlled Growth of ZnO Nanowires and Their Optical Properties. *Advanced Functional Materials* **2002,** *12* (5), 323-331.
4. Liu, J.; Zhang, Z.; Su, X.; Zhao, Y., From zinc nanowires to zinc oxide nanowires: a low substrate-temperature approach. *Journal of Physics D: Applied Physics* **2005,** *38* (7), 1068-1071.
5. McCune, M.; Zhang, W.; Deng, Y., High efficiency dye-sensitized solar cells based on three-dimensional multilayered ZnO nanowire arrays with "caterpillar-like" structure. *Nano letters* **2012,** *12* (7), 3656-62.
6. Kong, X. Y.; Ding, Y.; Wang, Z. L., Metal−Semiconductor Zn−ZnO Core−Shell Nanobelts and Nanotubes. *The Journal of Physical Chemistry B* **2003,** *108* (2), 570-574.
7. Xing, Y. J.; Xi, Z. H.; Zhang, X. D.; Song, J. H.; Wang, R. M.; Xu, J.; Xue, Z. Q.; Yu, D. P., Nanotubular structures of zinc oxide. *Solid State Communications* **2004,** *129* (10), 671-675.
8. Park, J.-H.; Choi, H.-J.; Park, J.-G., Scaffolding and filling process: a new type of 2D crystal growth. *Journal of Crystal Growth* **2004,** *263* (1–4), 237-242.
9. Park, J.-H.; Choi, H.-J.; Choi, Y.-J.; Sohn, S.-H.; Park, J.-G., Ultrawide ZnO nanosheets. *Journal of Materials Chemistry* **2004,** *14* (1), 35-36.
10. Pan, Z. W.; Mahurin, S. M.; Dai, S.; Lowndes, D. H., Nanowire Array Gratings with ZnO Combs. *Nano letters* **2005,** *5* (4), 723-727.
11. Cheng, C.; Liu, B.; Yang, H.; Zhou, W.; Sun, L.; Chen, R.; Yu, S. F.; Zhang, J.; Gong, H.; Sun, H.; Fan, H. J., Hierarchical Assembly of ZnO Nanostructures on SnO2 Backbone Nanowires: Low-Temperature Hydrothermal Preparation and Optical Properties. *ACS Nano* **2009,** *3* (10), 3069-3076.
12. Wang, Z. L., Zinc oxide nanostructures: growth, properties and applications. *Journal of Physics: Condensed Matter* **2004,** *16* (25), R829-R858.
13. Brown, M. E., ZnO-Rediscovered. **1957**.
14. Klingshirn, C.; Hauschild, R.; Priller, H.; Decker, M.; Zeller, J.; Kalt, H., ZnO rediscovered — once again!? *Superlattices and Microstructures* **2005,** *38* (4-6), 209-222.
15. Yang, Y. H.; Chen, X. Y.; Feng, Y.; Yang, G. W., Physical Mechanism of Blue-Shift of UV Luminescence of a Single Pencil-Like ZnO Nanowire. *Nano letters* **2007,** *7* (12), 3879-3883.
16. Shen, G.; Bando, Y.; Lee, C.-J., Synthesis and Evolution of Novel Hollow ZnO Urchins by a Simple Thermal Evaporation Process. *The Journal of Physical Chemistry B* **2005,** *109* (21), 10578-10583.

17. Ren, S.; Bai, Y. F.; Chen, J.; Deng, S. Z.; Xu, N. S.; Wu, Q. B.; Yang, S., Catalyst-free synthesis of ZnO nanowire arrays on zinc substrate by low temperature thermal oxidation. *Materials Letters* **2007,** *61* (3), 666-670.

18. Chang, P.-C.; Fan, Z.; Wang, D.; Tseng, W.-Y.; Chiou, W.-A.; Hong, J.; Lu, J. G., ZnO Nanowires Synthesized by Vapor Trapping CVD Method. *Chemistry of Materials* **2004,** *16* (24), 5133-5137.

19. Baruah, S.; Dutta, J., Zinc stannate nanostructures: hydrothermal synthesis. *Science and Technology of Advanced Materials* **2011,** *12* (1), 013004.

20. Lee, J.-S.; Park, K.; Kang, M.-I. L.; Park, I. L. W.; Kim, S.-W.; Cho, W. K.; Han, H. S.; Kim, S., ZnO nanomaterials synthesized from thermal evaporation of ball-milled ZnO powders. *Journal of Crystal Growth* **2003,** *254* (3-4), 423-431.

21. Lim, Y. S.; Park, J. W.; Hong, S. T.; Kim, J., Carbothermal synthesis of ZnO nanocomb structure. *Materials Science and Engineering: B* **2006,** *129* (1-3), 100-103.

22. (a) Rackauskas, S.; Nasibulin, A. G.; Jiang, H.; Tian, Y.; Kleshch, V. I.; Sainio, J.; Obraztsova, E. D.; Bokova, S. N.; Obraztsov, A. N.; Kauppinen, E. I., A novel method for metal oxide nanowire synthesis. *Nanotechnology* **2009,** *20* (16), 165603; (b) Luo, L.; Sosnowchik, B. D.; Lin, L., Room temperature fast synthesis of zinc oxide nanowires by inductive heating. *Applied Physics Letters* **2007,** *90* (9), 093101.

23. Yan, Y.; Liu, P.; Romero, M. J.; Al-Jassim, M. M., Formation of metallic zinc nanowires. *Journal of Applied Physics* **2003,** *93* (8), 4807.

24. Coleman, R. V., Caberra, N., Gilamn, J.J. (ed), The Art of Growing Crystals. **1963**, 3-28.

25. Gao, P. X.; Wang, Z. L., Nanopropeller arrays of zinc oxide. *Applied Physics Letters* **2004,** *84* (15), 2883.

26. Smeltzer, W. W.; Young, D. J., Oxidation properties of transition metals. *Progress in Solid State Chemistry* **1975,** *10, Part 1* (0), 17-54.

27. Young, D. J., High temperature oxidation and corrosion of metals: Corrosion series. **2008**, 81-96.

28. Liu, B.; Zeng, H. C., Direct growth of enclosed ZnO nanotubes. *Nano Research* **2009,** *2* (3), 201-209.

29. Yuvaraj, D.; Rao, K. N., Selective growth of ZnO nanoneedles by thermal oxidation of Zn microstructures. *Materials Science and Engineering: B* **2009,** *164* (3), 195-199.

30. Yu, H.; Zhang, Z.; Han, M.; Hao, X.; Zhu, F., A General Low-Temperature Route for Large-Scale Fabrication of Highly Oriented ZnO Nanorod/Nanotube Arrays. *Journal of the American Chemical Society* **2005,** *127* (8), 2378-2379.

Chapter 3: Consistent Large ZnO Nanosheet Synthesis at Lower Temperatures

3.1 Introduction

ZnO is a useful wide band gap (3.37eV) semiconducting material[1] with photoelectrochemical[2] and piezoelectric[3] properties. ZnO can be produced in bulk crystals[4], thin films[5,6], and a variety of nanostructures[7,8]. These nanostructures, which can be grown through Chemical Vapor Deposition (CVD) include nanowires, nanosheets, combs, ribbons, and tetrapods. These structures can be grown via Vapor Liquid Solid (VLS) or catalyst free. Nanostructures are particularly interesting because their size alters certain properties[9,10].

One particular nanostructure of interest is large ZnO freestanding ribbons[11] or often referred to as sheets[12]. Optical[13] and piezoelectric[10] properties have been investigated. Though VLS growth through the use of a catalyst[12] has been used, it showed little effect on ribbon growth[14]. These nanostructures can be grown in vapor through ZnO thermal evaporation at 1400°C[15,16]; carbothermal evaporation at 950°C[17]; or zinc evaporation at 650°C[14]. Each successive growth temperature experiment introduces improvements to the system's design that take advantage of Zn's vapor required conditions.

Despite the different temperatures, one thing that remained consistent is that ribbons and sheets grown in vapor are heavily influenced by the oxygen: argon flow ratios[14,18]. Oxygen is used as the reactant gas; and argon is used as the transport gas. Literature has suggested that two-dimensional ribbon and sheet grow under an oxygen: argon ratio range between 5:100-10:100. Below this ideal ratio, one-dimensional nanowires growth is quite dominant. At higher ratios between 10:100-20:100, three-dimensional structures' growth, such as multipods, is dominant. At ratios above 20:100, ZnO tetrapods are commonly found.

Some groups have discussed mechanism of the nanosheet growth under the VLS mechanism[12]. Park provides a schematic of sheet growth where a gold droplet catalyst would initiate nanowire nucleation and growth[12]. However ZnO ribbons and sheets have been grown without a catalyst. During the nanowire growth, secondary nanowires begin to grow from the side of the original nanowire growth. The pattern of these nanowires looks like a comb, which has been well documented. Between the secondary nanowires, heterogenous sites are formed for sheet growth. The sheets show a concaved meniscus between the nanowires, which corresponds to a capillary mechanism. The filling of the spaces helps lower the surface energy of the ZnO nanostructures. Literature has suggested that the main nanowire backbone grow in the [0001][19] direction. However, the growth of sheet can be in the [0001][15], $[10\bar{1}0]$[13], and $[21\bar{1}0]$[13] directions.

Reported ribbon and sheet growths grown through zinc evaporation were mixed with various nanostructures, such as nanowires and three dimensional nanostructures[14]. This was not seen in ZnO ribbon or sheet growth grown through ZnO evaporation or carbothermal evaporation. The variation in structures seen in Zn evaporation growth can be attributed to the variation in Zn vapor pressure. For ZnO evaporation and ZnO carbothermal evaporation, Zn vapors are not released until a certain temperature is released that helps keep the Zn vapor pressure consistent.

One approach to grow ZnO ribbons sheets at low temperature is to use flash heating for Zn evaporation to minimize the Zn vapor pressure variation. In addition, an extended oxygen outlet can be used inside a vacuum tube furnace to localize the reaction region. An extended oxygen outlet was used in a Zn evaporation experiment to mass-produce ZnO tetrapods[20]. This experiment showed that tetrapods were formed homogenously where the core would be produced at high temperature and would grow legs at lower temperature regions. Unfortunately, there was not a lot of uniformity in the tetrapod results because flash heating of Zn evaporation was not used. The gradient furnace heating caused a gradient in Zn’s vapor pressure. Without a constant vapor pressure, tetrapods of different sizes were created. An additional step of chromatography was required to separate the desired nanostructures.

To keep cost low, Zn evaporation CVD is still the most economically viable technique amongst CVD systems. However to lower the temperature of production, the growth chamber needs to be designed to meet Zn evaporation challenges.

3.2 Experimental Work

To grow ZnO nanosheets more efficiently, a vacuum tube furnace CVD system was assembled with a 25 cm long tubular clamshell furnace, 2.5 cm in diameter quartz tube, and separate gas flow controllers for argon and oxygen. The system used a roughing pump to reach a minimum pressure of 0.005 torr. The CVD system was adapted with a tungsten filament wound Al_2O_3 crucible and an extended gas outlet for oxygen flow. The filament wound crucible sat outside the back end of the furnace and connected to a power supply for independent heating for zinc. Argon was used as the carrier gas while as oxygen served as the reagent material. The argon outlet was positioned downstream of the crucible to carry the zinc vapors into the furnace region. The oxygen line was fitted with an alumina tube that extended inside the furnace region, bypassing the crucible. The outlet was also positioned near the end of the furnace so that it created an oxygen environment in the furnace's natural temperature gradient region.

The CVD system's assembly was designed to have three zones: the evaporation zone, stabilization zone, and the reaction zone. A diagram of the furnace, its components, and zones can be seen in Figure 3.1. The evaporation zone was positioned just outside the tube furnace and was controlled by the filament wound crucible. The speed of the evaporation provided a large injection of Zn into the tubular furnace. The tungsten filament wound crucible allowed for quick evaporation for Zinc, capable of a 200°C/s temperature rate versus the clamshell furnace's heating rate of 35°C/min. The stabilization zone is a 25cm pathway inside the tube furnace. The evaporated zinc is carried by the argon gas flow into the temperature stabilization zone, set at 700°C, and into the reaction zone. The reaction zone was 5cm long, which began at the tip of the oxygen gas inlet and ended at the tube furnace's edge. The temperature profile of the reaction zone ranged from 700°C at the inlet tip and 400°C at the furnace edge. The extended oxygen gas inlet is important because it allowed for synthesis reaction of ZnO at peak temperatures inside the furnace zone. The gas inlet extension also bypassed the crucible to minimize oxidation of the tungsten filament and to prevent an oxide layer formation over the zinc that could act as a barrier for zinc evaporation.

This design addressed the main concerns for Zn evaporation and reaction control. With a crucible wound by tungsten, temperatures of the crucible could reach 1100°C very quickly, enabling the production of a consistent Zn vapor pressure. The temperature of the Zn vapors was stabilized inside the heated chamber. The extended outlet for the oxygen prevented premature Zn exposure to oxygen. Only until the Zn vapors traveled past the oxygen outlet were the Zn vapors exposed to oxygen. The substrates were placed in this reaction region. The temperature gradient profile of the CVD's reaction zone was monitored with thermocouples and recorded with LABview.

To grow ZnO nanostructures, 0.100 grams of metal Zn powders (100 mesh) were placed in the crucible upstream of the tube furnace and two RCA cleaned Si (111) substrates were placed in the downstream of a tube furnace. One Si (111) substrate was placed in the area that reached 700°C and the other Si (111) substrate was placed at the end of the furnace that reached 400°C. No catalyst was introduced to the Si substrates. After the substrate and the precursors were placed inside the chamber, the system was pumped down to a pressure of 0.005 torr. To determine the concentration of oxygen:argon flow ratio, the oxygen flow was set to 2.5, 5, 7.5, 10 or 20 sccm and the argon's flow was set to 100 sccm. Afterwards, the tube furnace was brought to a temperature of 700°C at a rate of 25°C per minute.

When these parameters were determined, the Zn powders were heated in the crucible to reach a temperature of 1100°C in 30 seconds. The temperature of the crucible was held for 1 minute until all of the Zn powder evaporated. As the Zn vapor traveled downstream, the vapors' temperature would stabilize in the tube furnace region. As the vapors entered the reaction region, the vapors would begin to oxidize.

Characterization of the ZnO nanostructures were primarily observed through the Scanning Electron Microscopy (SEM). Energy Dispersive X-Ray Spectroscopy (EDS) was also used to monitor if any contaminants were found.

Upon discovery of produced nanosheets, the experimental procedures were repeated with the corresponding oxygen:argon flow ratio on RCA Si substrates with the facets (100) and (110). Si substrates with different crystal planes were intentionally used to help determine whether or not the surface energy for a particular facet plane made observable alterations to the growth of ZnO nanosheets.

Finally, Transmission Electron Microscopy (TEM) was used for higher magnification and crystallography analysis. TEM preparation required nanosheet transfer from the Si substrate to a holey carbon film copper grid. Selective Area Electron Diffraction (SAED) was also used to determine the growth direction of the ZnO backbone, comb nanowire offshoots, and the nanosheets that form between the nanowire offshoots.

3.3 Results

This experiment produced a variety of different catalyst free ZnO nanostructures that corresponded with the specific oxygen:argon flow ratio and temperature zones, shown in Figure 3.2. The temperature zones are created by the natural temperature gradient at the end of the furnace. The respective temperatures of the two Si (111) substrates were 700°C and 400°C.

For the lowest oxygen:argon flow ratios set at 2.5:100, the SEM images showed few ZnO nanostructures nanowires were found in the 700^{o}C and 400^{o}C regions. Most of the evaporated zinc was deposited on the walls of the quartz tube, outside the furnace region. The region showed a dark gray color which corresponded with lightly oxidized zinc. When the oxygen:argon flow was raised to 5:100, the primary nanostructures observed included nanosheets and nanowires. Similar nanosheets were also found when the oxygen/argon flow ratio was set to 7.5:100. In addition, three-dimensional structures that resembled tetrapods were also found. However, these tetrapods were not complete. They were not autonomous and appeared to have nucleated from the substrate. At an increased oxygen:argon flow ratio set at 10:100, no nanosheets were found and nanostructures that resembled tetrapods were primarily found. Many of these ZnO nanostructure clusters appeared to have connecting thin nanowires with a diameter measured to be 5nm. When the oxygen:argon flow ratio was set to 20:100, autonomous tetrapods and dendritic structures with many non-uniform offshoots were observed. These tetrapods had diameters of 100nm.

For all of these cases EDS showed only Si, Zn, and O peaks; where the substrate showed a Si peak and the nanostructures showed strong Zn and O peaks. No other peaks from other elements were found.

Based on the results from the (111) Si substrate experiment, the ribbon/nanosheet experiment at an oxygen:argon flow ratio of 5:100 was repeated for (100)Si and (110)Si substrates. Similar nanosheets were found on (100)Si and (110)Si substrates. The comparison can be seen in Figure 3.3. The nanosheets were found to have lengths of 5-60μm, widths of 500nm-20μm, and a thickness of less than 20nm. The thickness of a nanosheet can be seen in Figure 3.4(a). The nanosheet's thicknesses attributed to a translucency under the SEM is seen in Figure 3.4(b). The length of the sheets was dictated by a main backbone nanowire that were 5-60μm in length. Attached to the backbone nanowire were protruding parallel nanowires, which helped make the width of the nanosheet. Between these parallel nanowires were ZnO sheets.

These large sheets had a tendency to grow at the edge of the substrate. Along the edge, rough nucleation sites were more prevalent as seen in figure 3.5(a). For surface growth, ribbons/nanosheets were grown in dense clusters as seen Figure 3.5(b). Though not the dominant growth, there were also nanowires and thicker rods with tetrapod traits present in the clusters. The beginnings of new clusters were initiated by individual ZnO nanostructures heterogeneously nucleating on the surface of the substrate. These clusters could include as many as a few hundred sheets in a compacted area. There were very few areas where singular large nanosheets were observed.

SAED TEM was used to determine the growth direction of a nanosheet. Two diffraction patterns were found in the $(\bar{1}2\bar{1}3)$ zone and the $(2\bar{1}\bar{1}0)$ zone. The cross product of these zones suggested the sheet grew in the $[10\bar{1}0]$ or [210] direction. The TEM images are shown in Figure 3.6.

3.4 Discussion

A variety of similar structures were created in this work that consistently corresponded to similar ZnO evaporation and ZnO carbothermal oxygen:argon flow experiments. The change in CVD design allowed for increased processing efficiency in comparison to ZnO evaporation and ZnO carbothermal evaporation CVD designs. The design also allowed for less variation in nanostructures at lower oxygen flows due to the Zn flash evaporation. The nanosheets had similar dimensions, comb-like structures, and thicknesses. The nanostructures produced in this experiment corresponded to similar oxygen:argon flow ratios[17] shown in Park's paper. This work also distinguished itself from previous Zn evaporation oxygen:argon flow experiments because there was less variation in nanostructures. Nanostructures could be distinctly grown based on oxygen:argon flow because the Zn vapor pressure was consistent due to flash heating.

The new design of the CVD chamber allowed for a furnace chamber to be set at lower a temperature. For this work, the furnace was set to 700^{o}C which is 100^{o}C lower than required for carbothermal evaporation[12]; and 700^{o}C lower than the minimum temperature for ZnO decomposition. ZnO sheets were found on substrates that were measured at on both substrates set at 700^{o}C and 400^{o}C. This growth temperatures of this work falls below range as some groups that grew ribbons in the range of 650-750^{o}C[11,21].

The proposed growth mechanism for these nanosheets is similar to that of Park's theory. However, no metal catalyst was used to initiate heterogenous nucleation. Unlike previously reported nanosheet VLS growth, this work used no metal catalyst. Thus, the primary growth method for these nanosheets had to be VS growth. As Zn vapors entered into the oxygen region of the tube furnace, the vapors would begin to oxidize and deposit on the quartz tube and on the Si substrates. The deposition would create clusters of ZnO nanowires. As some of these nanowires few into long nanowires, they would experience dendritic growth off the side of the long nanowires. Eventually, the space between the nanowires would be filled which would ultimately create a sheet.

There was not much difference in the ZnO nanosheet morphology on the Si substrates with different planar surfaces. A look at the different planar spacing in Table 3.1 shows the lattice parameters for each plane and the corresponding epitaxial ratio difference to ZnO grown in the [0001] direction. It is clear that the ZnO heterogeneously nucleated without having coherency to the Si lattice in the (111), (100), and the (110) planar directions. ZnO is known to show epitaxial growth with substrates like sapphire in the [0001] or the $[01\bar{1}2]$ direction[22] However, ZnO is also known to heterogeneously nucleate on many different surfaces regardless of epitaxial matching.

Ultimately, this work showed a simple method to help reduced the required growth temperature of large ZnO nanosheet synthesis and fabrication. Based on the design of the system, the nanosheets grown in this work were produced between 400-700°C, which is up to 250°C lower than the previously recorded work on nanosheets[14]. This lower temperature growth of large nanosheets allowed for greater yield of ZnO nanosheets. This designed allowed for more discrimination of ZnO particles in a Zn thermal evaporation. Figure 3.7 shows a map of the nanostructures under specific temperature vs oxygen:argon flow ratios. The system took into account the reactive nature of Zn vapors upon interaction with oxygen. By using a filament wound crucible, zinc was able to evaporate quickly without variation in vapor pressure and stabilize its temperature inside the tube furnace region. An extended outlet for oxygen also prevented premature oxidation with zinc.

3.5 Conclusion

Catalyst free large ZnO nanosheets with lengths between 5-60mm, widths between 5-20mm, and a thicknesses of less than 20nm were created in a modified tube furnace CVD system set at 700°C and an oxygen:argon flow set at 5:100 and 7.5:100. This is the lowest reported temperature for large ZnO nanosheet growth for a CVD system. Large ZnO nanosheets have possible applications in piezoelectric, semiconductor, and photoelectric applications. However, more work is required because the photoelectrochemical and piezo electric properties of large ZnO nanosheets are not well known. The large nanosheets grown through this work are comparable to higher temperature systems. The lower reaction temperature of ZnO nanosheets fabrication required modifications to a traditional tube furnace CVD system to produce a consistent Zn vapor and prevent premature oxidation. Premature oxidation was prevented through an extended oxygen outlet to bypass the Zn evaporation and stabilization regions. In this lower temperature growth, it was found that nanosheet growth is highly dependent on oxygen flow ratios. This work also found that different planar silicon wafers had little effect on the nucleation and growth of the ZnO nanosheets. Through TEM, the nanosheets' growth direction was determined.

3.6. Figures

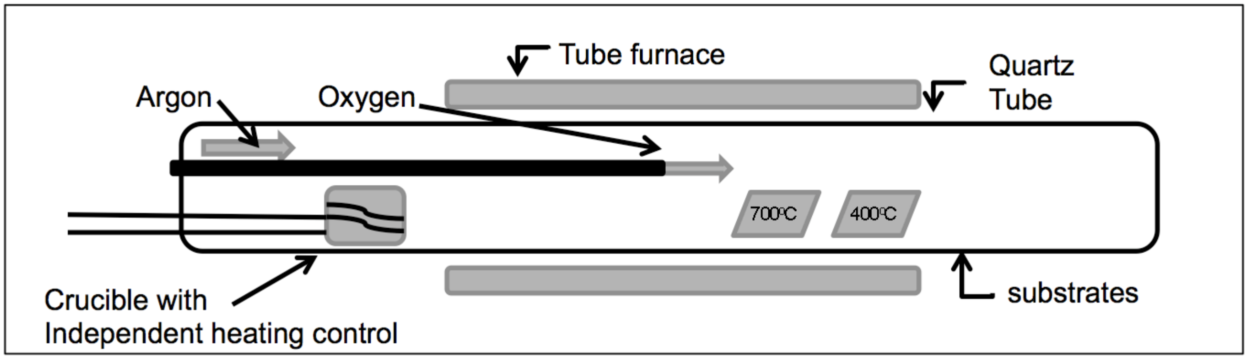

Figure 3. 1: A diagram of the tube furnace system is shown with an independent heating control for zinc vapors and separate Argon and Oxygen flows. The oxygen flow is injected in the furnace area to initiate the reaction area in the furnace region and minimize unintended oxidation of the zinc powders and the tungsten filament.

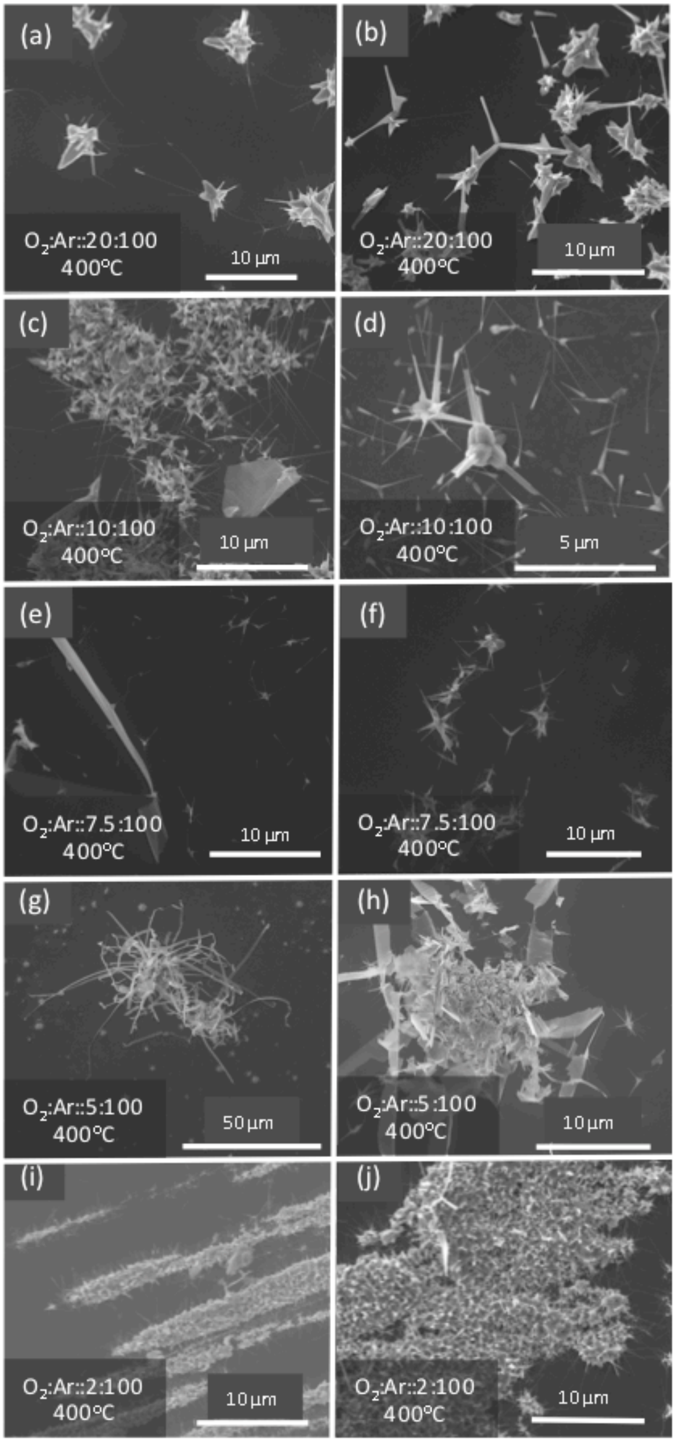

Figure 3. 2: This figure shows the variation of ZnO nanostructures grown in this system. The nanostructures are dictated by temperature and the Oxygen/:Argon flow ratio. At high O:Ar ratios that were greater than 1:10, three dimension ZnO nanostructures were commonly found. At O:Ar ratios between 1:20-1:10 freestanding ZnO nanosheets are commonly found. At O:Ar ratios below 1:20, ZnO nanowires are found.

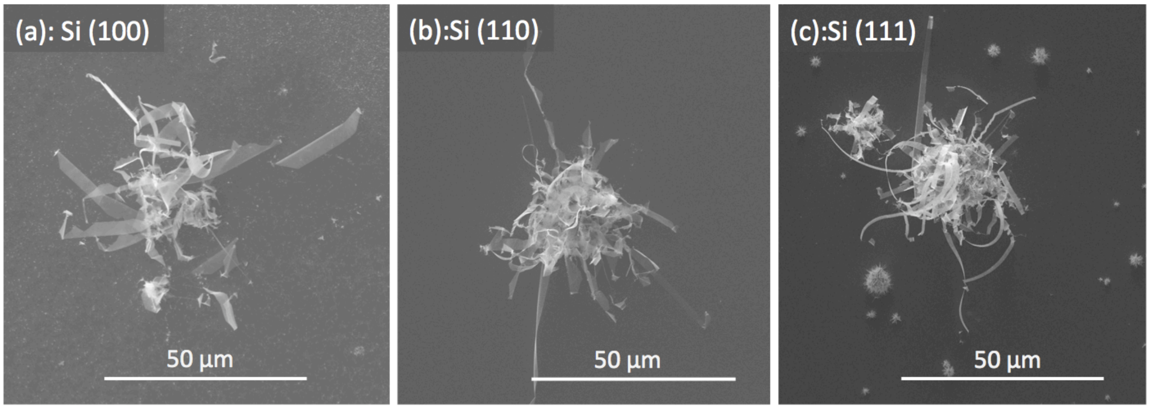

Figure 3. 3: The figure shows large freestanding ZnO nanosheet grown on silicon wafers with (100), (110), or (111) surface planes. The large freestanding ZnO nanosheets were not affected by the different surfaces.

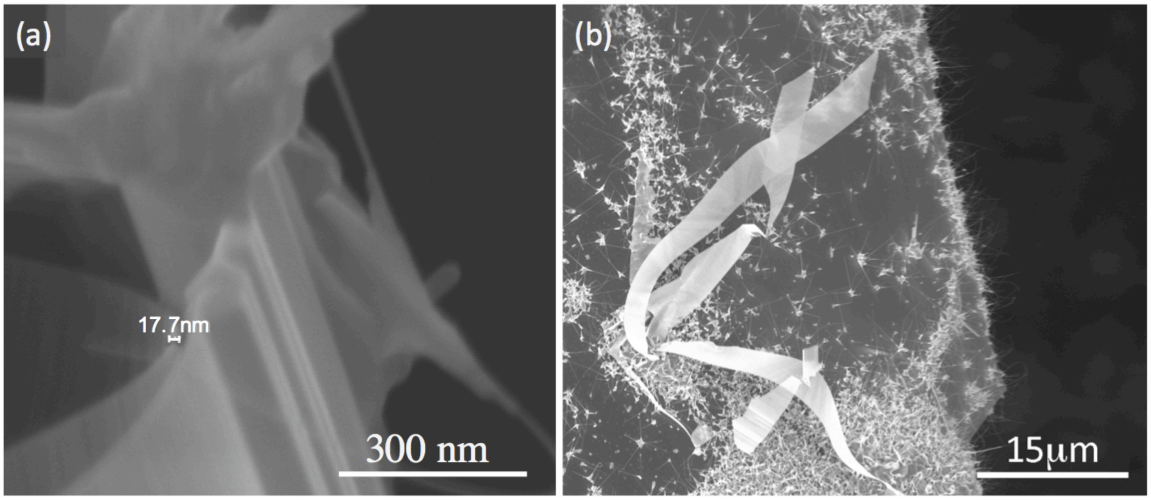

Figure 3. 4: The thicknesses of the nanosheets were measured to be less than 20 nm, which leads to their translucency under the SEM.

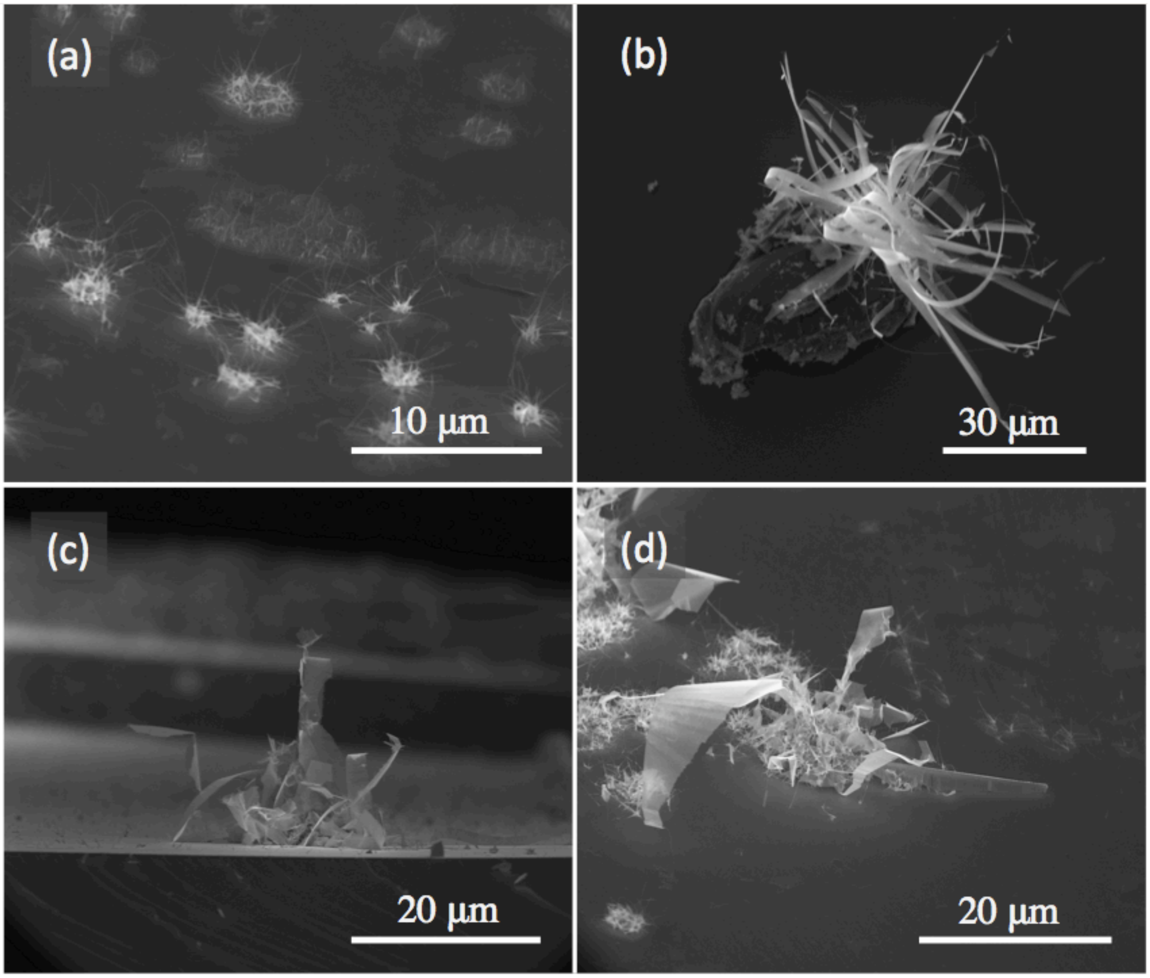

Figure 3. 5: (a) ZnO nanosheets would often grow in clusters that begin as nanowires, which tend to nucleate at rough areas such as edges of the Si wafer. (b) The figure shows a nanosheet cluster grew on Si particle. (c-d) The figures show the nanosheet clusters from different angles.

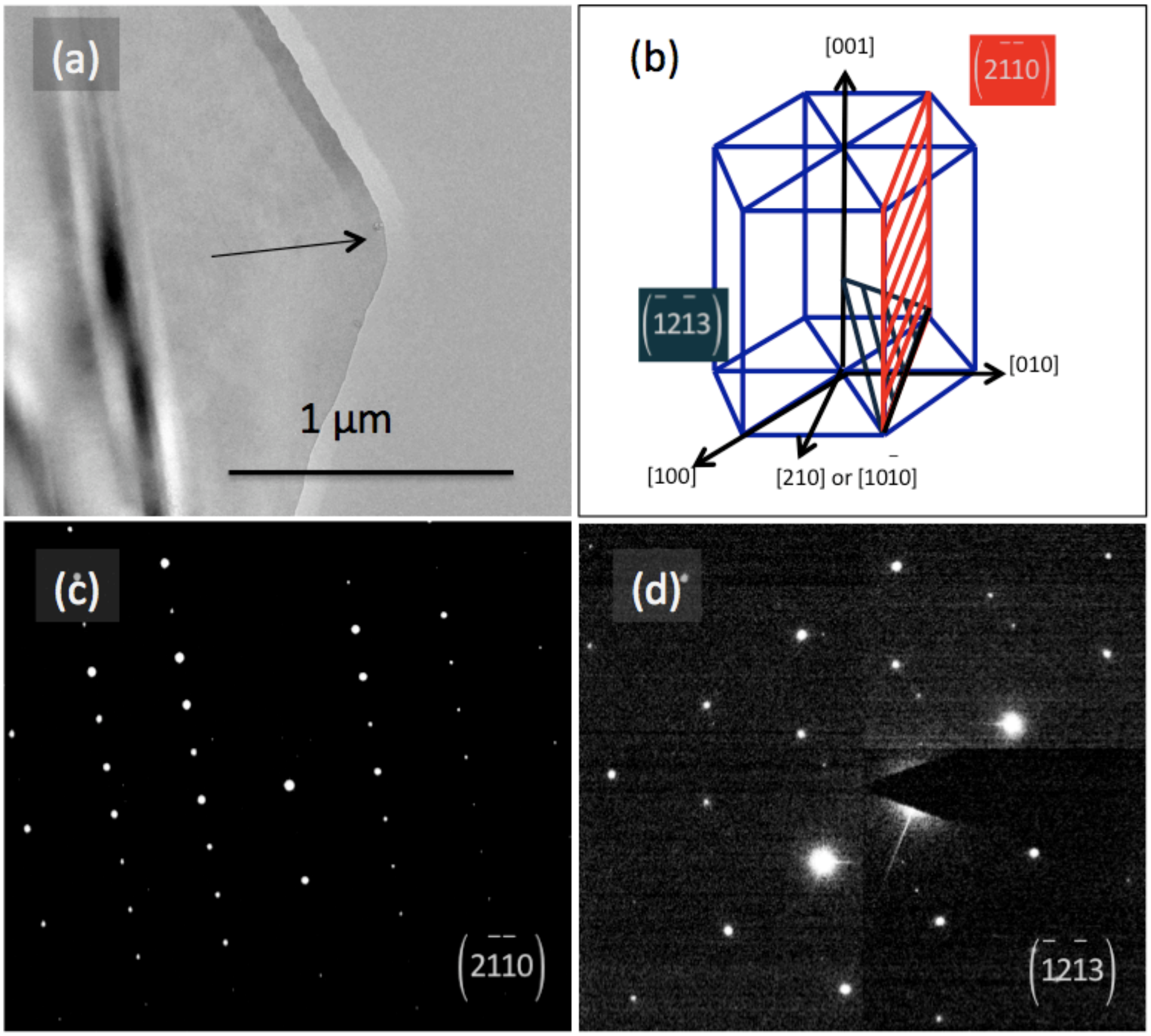

Figure 3. 6: A TEM images shows a nanosheet. SAED shows the (2110) and the (1213) zones. The cross product of the zones indicate that the nanosheet grew in the [210] direction.

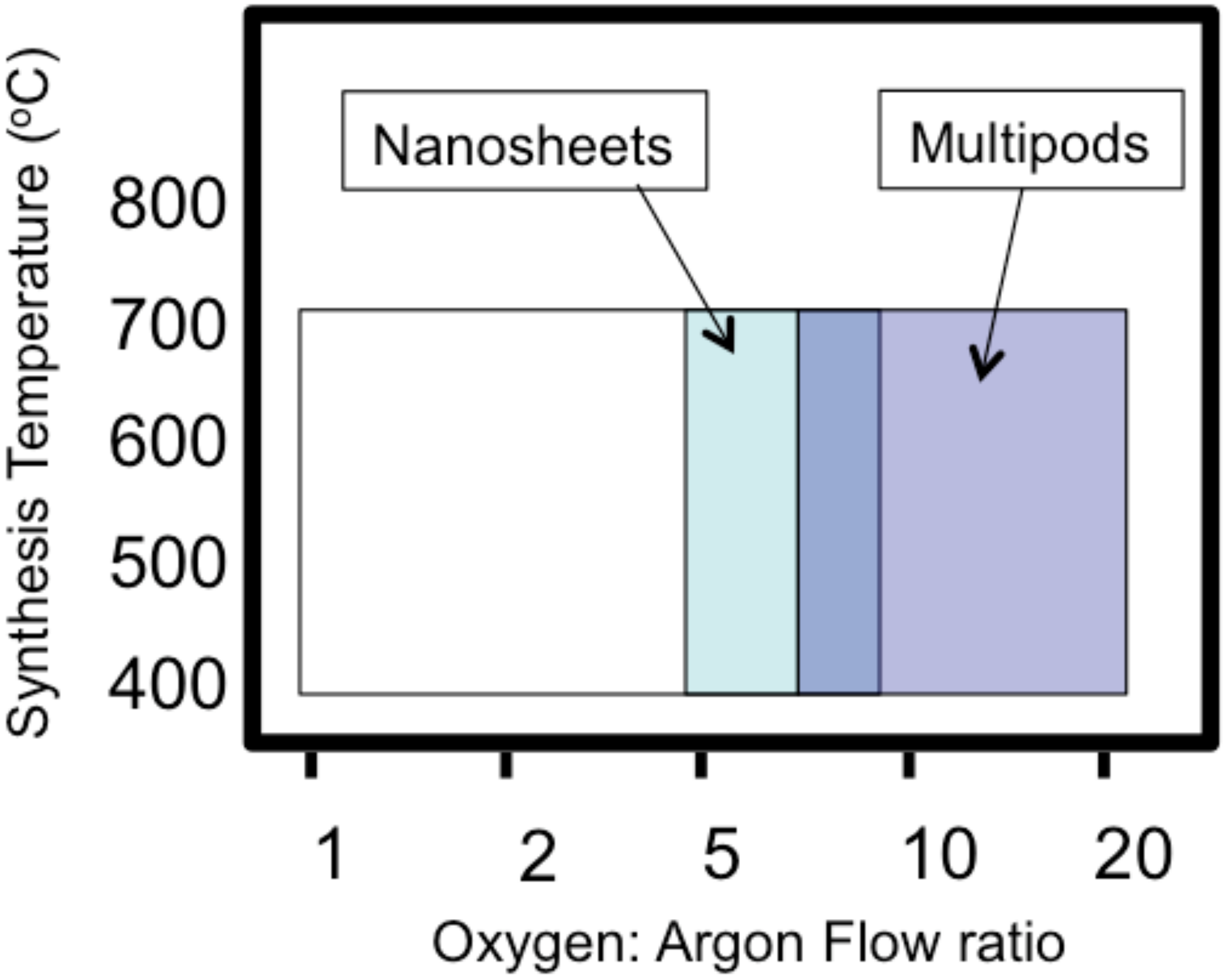

Figure 3. 7: A map of the observed ZnO nanostructures grown under different synthesis temperatures and Oxygen/Argon flow ratios.

Table 3. 1: Shows the Si spacing between different planes and the % difference between ZnO(1010): a=3.25Å.

Si	(100)	(110)	(111)
d (Å)	5.431	3.84	3.136
diff %	40.158	15.371	-3.649

3.7. References:

1. Özgür, Ü.; Alivov, Y. I.; Liu, C.; Teke, A.; Reshchikov, M.; Doğan, S.; Avrutin, V.; Cho, S.-J.; Morkoc, H., A comprehensive review of ZnO materials and devices. *Journal of applied physics* **2005,** *98* (4), 041301.
2. Keis, K.; Magnusson, E.; Lindström, H.; Lindquist, S.-E.; Hagfeldt, A., A 5% efficient photoelectrochemical solar cell based on nanostructured ZnO electrodes. *Solar Energy Materials and Solar Cells* **2002,** *73* (1), 51-58.
3. Wang, Z. L.; Kong, X. Y.; Ding, Y.; Gao, P.; Hughes, W. L.; Yang, R.; Zhang, Y., Semiconducting and piezoelectric oxide nanostructures induced by polar surfaces. *Advanced Functional Materials* **2004,** *14* (10), 943-956.
4. Janotti, A.; Van de Walle, C. G., Fundamentals of zinc oxide as a semiconductor. *Reports on Progress in Physics* **2009,** *72* (12), 126501.
5. Ghandhi, S. K.; Field, R. J.; Shealy, J. R., Highly oriented zinc oxide films grown by the oxidation of diethylzinc. *Applied Physics Letters* **2008,** *37* (5), 449-451.
6. Natsume, Y.; Sakata, H., Zinc oxide films prepared by sol-gel spin-coating. *Thin solid films* **2000,** *372* (1), 30-36.
7. Wang, Z. L., Zinc oxide nanostructures: growth, properties and applications. *Journal of Physics: Condensed Matter* **2004,** *16* (25), R829-R858.
8. Fan, Z.; Lu, J. G., Zinc oxide nanostructures: synthesis and properties. *Journal of nanoscience and nanotechnology* **2005,** *5* (10), 1561-1573.
9. Yang, Y. H.; Chen, X. Y.; Feng, Y.; Yang, G. W., Physical Mechanism of Blue-Shift of UV Luminescence of a Single Pencil-Like ZnO Nanowire. *Nano letters* **2007,** *7* (12), 3879-3883.
10. Zhao, M.-H.; Wang, Z.-L.; Mao, S. X., Piezoelectric characterization of individual zinc oxide nanobelt probed by piezoresponse force microscope. *Nano letters* **2004,** *4* (4), 587-590.
11. Yao, B.; Chan, Y.; Wang, N., Formation of ZnO nanostructures by a simple way of thermal evaporation. *Applied Physics Letters* **2002,** *81* (4), 757-759.
12. Park, J.-H.; Choi, H.-J.; Choi, Y.-J.; Sohn, S.-H.; Park, J.-G., Ultrawide ZnO nanosheets. *Journal of Materials Chemistry* **2004,** *14* (1), 35-36.
13. Leung, Y.; Djurišić, A.; Gao, J.; Xie, M.; Wei, Z.; Xu, S.; Chan, W., Zinc oxide ribbon and comb structures: synthesis and optical properties. *Chemical physics letters* **2004,** *394* (4), 452-457.
14. Zha, M.; Calestani, D.; Zappettini, A.; Mosca, R.; Mazzera, M.; Lazzarini, L.; Zanotti, L., Large-area self-catalysed and selective growth of ZnO nanowires. *Nanotechnology* **2008,** *19* (32), 325603.
15. Pan, Z. W.; Dai, Z. R.; Wang, Z. L., Nanobelts of semiconducting oxides. *Science* **2001,** *291* (5510), 1947-9.
16. Pan, Z. W.; Dai, Z. R.; Wang, Z. L., Nanobelts of semiconducting oxides. *Science* **2001,** *291* (5510), 1947-1949.

17. Park, J.-H.; Choi, H.-J.; Park, J.-G., Scaffolding and filling process: a new type of 2D crystal growth. *Journal of Crystal Growth* **2004,** *263* (1–4), 237-242.
18. Lim, Y. S.; Park, J. W.; Hong, S. T.; Kim, J., Carbothermal synthesis of ZnO nanocomb structure. *Materials Science and Engineering: B* **2006,** *129* (1-3), 100-103.
19. Pan, Z. W.; Mahurin, S. M.; Dai, S.; Lowndes, D. H., Nanowire Array Gratings with ZnO Combs. *Nano letters* **2005,** *5* (4), 723-727.
20. Zanotti, L.; Calestani, D.; Villani, M.; Zha, M.; Zappettini, A.; Paorici, C., Vapour‐phase growth, purification and large‐area deposition of ZnO tetrapod nanostructures. *Crystal Research and Technology* **2010,** *45* (6), 667-671.
21. <2003. zhang. Oxide-assisted semiconductor nanowire growth.pdf>.
22. Haga, K.; Kamidaira, M.; Kashiwaba, Y.; Sekiguchi, T.; Watanabe, H., ZnO thin films prepared by remote plasma-enhanced CVD method. *Journal of crystal growth* **2000,** *214*, 77-80.

Chapter 4: ZnO Nanostructure Combustion Synthesis for Hybridization of ZnO nanostructures on Carbon Fibers

4.1. Current Hybridization Methods of ZnO nanostructures on Carbon fiber and Metal Oxide Nanostructure Combustion Synthesis

Recent reports have shown successful hybridization of ZnO nanostructures on carbon fiber[1,2,3]. This has enabled photovoltaic and piezoelectric functionalities for carbon fiber composites. For applications, these will enable structural materials to have energy harvesting[2], sensing, and damping functionalities[4]. These efforts validate the opportunity for research in multifunctional materials.

The methods shown in the previous chapters about ZnO nanostructures growth have provided good fundamental understanding about ZnO nanostructure growth through vacuum thermal oxidation[5] and chemical vapor deposition (CVD)[6,7]. The fundamental understanding of ZnO properties and nanostructure provides a means to develop nanostructures for applications in semiconductor, actuators, and solar cell research. However, vacuum thermal oxidation and chemical vapor deposition setups are inherently expensive making initial cost for production costly. These systems also use high-temperature furnaces that were required considerable amount of energy and long processing times[8,9]. By their nature, vacuum systems are best suited for bench top testing. In addition, these systems have a limited allowable volume of operations because it must be relatively confined to maintain low pressure. Contrary to the high cost of traditional ZnO nanostructure growth, ZnO nanostructures growth was originally pursued for cost saving due to its low material cost. Thus if nanostructures growth is expensive, ZnO nanostructure production loses on of its original purpose. For future viability of ZnO nanostructure systems, a more robust, low-cost, and faster producing method for ZnO nanostructure growth is needed. A robust method that is out of vacuum for large quantity of ZnO nanostructure production should be considered.

The method must also determine effective ways to incorporate ZnO with carbon fiber. A few groups have tried a number of different methods. The first method was a post fabrication method where ZnO powders were incorporated into epoxy resin, which were then infused with the carbon fiber. Unfortunately, many of these nanoparticles were not anisotropic which is critical for useful piezoelectric applications. Groups have successfully grown aligned arrays of ZnO nanowires on carbon fiber by using carbon fiber as a substrate CVD[1] and hydrothermal processes[3]. A hybridized carbon fiber with ZnO nanowires through CVD can be seen in figure 4.1(a)[1] and a similar hybridized carbon fiber with ZnO nanowires through hydrothermal process is seen in figure 4.1(b)[10].

However, these methods are not economically friendly due their long processing time, high temperature apparatus, limited yield, and costly equipment. For CVD hybridization, it requires a furnace growth of 1020°C and a reaction period of 30 minutes to grow ZnO nanowires that reached 5µm[1] as seen in figure 4.1(a)[1]. The processing time does not include the furnace ramp and cool down period, which for most tube furnaces requires 2-3 hours. In addition, due to the hot oxygen-rich vacuum environment, carbon fiber intrinsic properties are compromised because graphitic carbon fiber begins to decompose at 300°C in oxygen environments[11]; a vacuum environment in a CVD chamber only accelerates that decomposition. To avoid the degradation of carbon fiber, groups have successfully grown ZnO nanowires on carbon fiber, using a hydrothermal reaction process[2,4]. The hydrothermal process helped preserve the carbon fiber's mechanical strength while still successfully showing the hybridization of ZnO nanowires on carbon fiber. However, this process is not economically viable due to its long cycle time taking 4-5 hours, required chamber temperature of 350^{o}C, and expensive precursor zinc acetate. In these hydrothermal hybridization process, it has yielded 2-5 µm long nanowires with 100 nm diameters as seen in figure 4.1(b)[10].

For over a century, mass ZnO production has been performed out of vacuum[12]. By heating zinc in atmospheric conditions, Zn vapors are produced and quickly react with the atmospheric oxygen. If need be, supplemental oxygen can be added. This process is known as Self-propagating High-temperature (combustion) Synthesis (SHS)[13]. The process consists of powder ignition, reaction with ambient or controlled gas systems, and a substantial heat release (exothermic reaction), which propagates further chemical reaction until all the reactants have been consumed. The benefits for SHS includes fast heating and cooling rates, optional inert or ambient conditions, lower costs setups, and faster processing times by orders of magnitude.

When heated too quickly, Zn has be possibility of becoming flammable where it has a high probability to burn. In the last two centuries, this method is known as the French method, which has helped produced a large amount of ZnO used for medicinal, pigment, and other general uses[12] . In this process, Zinc vapors are generated to react with the atmospheric oxygen[14]. Upon high enough temperature, enough Zn vapors are generated to form ZnO nuclei through homogenous nucleation[15]. If the temperatures are low enough, ZnO will deposit heterogeneously on other structures[16].

Zn burning or Zn combustion, has been well documented. By definition, combustion is the action of ignition and burning[17]. For metals, the combustion sequence consists of melt, evaporation, and reaction. The metal must first absorb enough heat to break the metallic bonds priming it as free vapor particles. Different modes of energy transfer can trigger ignition, such as: hot surfaces, sparks, and mechanical impacts. In this process, metal vapors are generated and rapidly react with atmospheric oxygen. Like previous Zn reactions shown in vacuum thermal oxidation and CVD, the chemical reaction still remains:

$$Zn + \frac{1}{2}O_2 \rightarrow ZnO$$

The oxidation reaction is also highly exothermic and the heat of combustion is 700KJ/mol[2]. The approximate combustion temperature that has been suggested is 1,800°C[18].

Under atmospheric conditions, the oxygen content is 20% at 1atm[19]. This provides an oxygen concentration of 8.7 moles/m^3. Thus for every 0.1gram of zinc, it requires a minimum of 6,000cm^3 for there to be enough oxygen for full explosive thermal oxidation.

Some groups have taken advantage of SHS and have found clever methods produced ZnO nanostructures through resistive heating and flame synthesis. In both cases, they also used an out of vacuum approach and performed their work in ambient conditions. The atmospheric elemental breakdown can be seen in the table 4.1 which shows the atmosphere is primarily composed of nitrogen and oxygen.

When Zn is heated or burned in atmospheric conditions, one possibility of concern is the forming of Zinc Nitride (Zn_3N_2), not ZnO[20]. Normally this is an area of concern for metallic combustion because there could be a lot of byproducts during atmospheric ZnO nanostructure synthesis. However, it is difficult to create Zn_3N_2 in atmospheric conditions. Zinc nitride must be formed in an oxygen free environment where Zn is only exposed to ammonia, above a temperature of 600°C. If the possibility occurred where Zn nitride is created, Zinc nitride will then thermally decompose in the presence of water vapor and form ZnO and ammonia[21].

$$Zn_3N_2 + 3H_2O \rightarrow 3ZnO + 2NH_2$$

Thus ZnO is the primary material produced under Zn burning under atmospheric conditions.

Another possible set of by-product concerns is zinc carbides. However, binary zinc carbides do not form unless exposed to high pressure (>8.0GPa) and high temperature (>1600°C)[22]. Due to this requirement, ZnO nanowires can be synthesized in carbon based flame synthesis without creating Zn carbide compounds[23]. Characterization has shown no forms of Zinc carbide. Flame synthesis has become a popular method of ZnO nanowire synthesis because it can produce large quantities of ZnO nanostructures without expensive apparatus.

By understanding metal (including Zn) atmospheric and compound reactions, a group has used a simple resistive heating experiment of metal wires and produced arrays of metal oxide nanowires via thermal oxidation[24,25]. Figure 4.2[24] shows SEM and TEM images of their various Fe_2O_3, V_2O_5, CuO, and ZnO nanowires.

For ZnO nanowire arrays, the group connected a zinc wire to a power supply. As power was introduced, the Zn wire began to generate heat. If the Zn wire is heated too quickly, a flame will then be created, consuming the metallic wire to the point where the wire breaks and shorts. If the wire was heated too slowly, oxidation of the wire through the surface as current continues to run through the wire. Upon a heating rate that lied between a destructively fast rate and a slow oxidizing rate, the wire will develop a small flame to generate nanowires without destroying the wire. According to their proposed nanowire array model, an oxide coat made up of ZnO scales was initially generated. The measured wire's temperature was reported as 700°C with an IR pyrometer**.** Scales were created when zinc was exposed to high temperatures; low temperature heating required a uniform oxide layer. The metallic zinc would diffuse to the surface through the grain boundaries rather than through the scales. At the surface, Zn quickly becomes an oxide. The newly formed oxide served as a seed for nanowire growth. The metallic zinc, behind the newly formed oxide, diffused through the oxide seed to become a nanowire.

Figure 4.3[25] shows an illustration of the group's propose growth mechanism behind the ZnO nanowire growth. They suggested through their TEM characterization that the nanowire grew in the basal direction because it had the highest directional diffusion constant for ZnO wurtzite.

This grain boundary diffusion and eventual nanowire growth (through newly formed ZnO seeds) occurs all over the wire where the density of nanowires was 100/mm. For this experiment, it was shown that nanowire growth was generated from thermal oxidation, a diffusion growth based model.

4.2 Combustion Theory

Zinc is a well-known combustible material[19]. Before combustion, zinc, like other metals, will melt and evaporate. Combustion is the process when a material reacts violently with oxygen both in pressure and temperature.

$$fuel + oxygen \rightarrow oxides + heat$$

If combustion is performed in ambient conditions, the oxygen concentration is set at 20%[19] at 8.7 mol/m^3. The chemical reaction is highly exothermic and usually last no more than 2-3 seconds. The combustion sequence is ignition, propagation, and consumption. Ignition is the initial step for combustion, which is an energy transfer process from one system to another. Ignition can occur through various means: heat transfer, electrical discharge, or mechanical shocks. Once ignition occurs, the chemical reaction increases the local temperature, which affects surrounding particles to become more reactive. This process will continue as it propagates throughout the whole system until the reactants is consumed. Under typical combustion, the reaction does not stop unless all the reacts are consumed or the reaction is not violent to transfer the sufficient heat to the reactant material. There are two major considerations for combustion: Thermodynamics and Kinetics. Thermodynamics defines the necessary conditions for the combustion ignition and propagation. Kinetics determines the required heat transfer rate to set of an ignition reaction.

4.2.1 Thermodynamics

To calculate the thermodynamic conditions required for combustion, it is important to assume adiabatic conditions. Due to the highly exothermic reaction, the system can be assumed to be thermally isolated where there is little time for heat to disperse to surrounding and be affected by external heat to enter[13,26]. This is not perfect assumption but it provides a good model for combustion. The max temperature that the product reaches is the adiabatic temperature, T_{ad}.

The state function, Enthalpy, can be used to help quantify the required energy for combustion:

$$\Delta H^0 = \Delta H^0_{f,298} + \int_{298}^{T_{ad}} \Delta C_p(product)dT$$

where $\Delta H^0_{f,298}$ is identified as the standard enthalpy of the product formation at 298K, ΔC_p is the change in heat capacity for the product formation. ZnO is known to have a standard enthalpy of formation at -350 $KJmol^{-1}$ at 298K[27]. The heat capacity values can be identified in a thermodynamic database[28].

When the system is assume to be thermally isolated (adiabatic system) there is no heat exchange where $\Delta H^0=0$. The previous equation can be simplified:

$$-\Delta H^0_{f,298} = \int_{298}^{T_{ad}} \Delta C_p(product)dT$$

If combustion occurs at the melting point of species, where $T_{ad}=T_{mp}$, the standard enthalpy of product formation must consider a fraction v of the species turns to a liquid state. This can be expressed as:

$$-\Delta H^0_{f,298} = \int_{298}^{T_{ad}} \Delta C_p(product)dT + v\Delta H_m$$

where ΔH_m is the heat of fusion. For Zn, the heat of fusion is known to be 7.32 kJ/mol^{-1}.

For zinc, combustion does not occur until zinc vapors are generated. Thus the temperature of the system must be above the melting temperature where $T_{ad}>T_{mp}$. An addition component of the change in the heat capacity of the liquid state must be taken into account. Thus for Zinc, the standard enthalpy of formation of ZnO can be expressed through the following equation:

$$-\Delta H^{0}_{f,298} = \int_{298}^{T_{mp}} \Delta C_p(product, solid)dT + \upsilon \Delta H_m + \int_{mp}^{T_{ad}} \Delta C_p(product, liquid)dT$$

where the change of heat capcities are speicific for each state. For ignition to occur through heat transfer, there is often preheating which will elevate the temperature. Thus the ignition enthalpy of formation of ZnO can be expressed through the following equation.

$$-\Delta H^{0}_{f,T_{ig}} = \int_{T_{ig}}^{T_{mp}} \Delta C_p(product, solid)dT + \upsilon \Delta H_m + \int_{mp}^{T_{ad}} \Delta C_p(product, liquid)dT$$

The adiabatic temperature can be calculated through constants found in literature and data tables. However, it is difficult to assume that the calculated adiabatic temperature is in agreement with the combustion temperature because many factors that need to be considered and are difficult to isolate.

4.2.2. Kinetics

In combustion studies, it was found that the kinetics plays a role in combustion.

If a hot surface is the source of metal powder combustion, the rate at which heat is transferred must be taken into consideration[29,30]. The heat transfer rate, R_S, must be sufficient to meet the thermodynamic requirement and also faster than the reaction rate, R_G. If the reaction rate is below the minimum heat transfer rate, diffusion is the dominant oxidation mechanism, not combustion. Heat transfer rates above this threshold will cause the powders to become instable, resulting in combustion, an exothermic reaction.

Kamenetskii[31] presented his findings through the following rate equations: R_G is defined by the following equation:

$$R_G = \frac{QC_{OS}Dfexp\left(-\frac{E}{RT}\right)}{D + fexp\left(-\frac{E}{RT}\right)}$$

where Q is the heat of reaction (700KJ/mol)[19], C_{OS} is the oxygen concentration, D is the thermal diffusion rate constant, f is the pre exponential or frequency factor, E is the activation Energy (J/mol), R is the gas constant 8.314 (J/mol K), T is the absolute temperature. For zinc, the thermal diffusion rate[32] can be calculated:

$$D(\frac{m^2}{s}) = \frac{\kappa}{\rho c_p} = \frac{113\left(\frac{W}{m\times K}\right)}{6.57\ \left(\frac{g}{cm^3}\right)\times 0.382\left(\frac{kJ}{kg\times K}\right)} = 4.50E^{-5}(m^2/s)$$

where κ is the thermal conductivity, ρ is the density, and c_p the heat capacity.

Likewise, R_s can be defined by the following equation:

$$R_S = h(T - T_0)$$

where h is the heat transfer coefficient, T is the temperature of the carbon fiber, and T_0 is the ambient temperature.

When mapping out R_R vs different R_S curves, important information can be predicted to thermal oxidation and combustion. If R_S to the right of the R_R curve, no combustion occurs. There is a competing oxide diffusion mechanism. If the R_S is to the left of the curve, the Zn vapors are generated before the creation of an oxide layer. Thus Zn vapors are allowed to leave the system and react with the oxygen. This reaction also causes an exothermic reaction which helps propagates other Zn vapors to form. A representation of three different heat transfer curves and the reaction curve can be seen in figure 4.4[31].

4.2.3. Geometry and Size

For metal combustion, geometry and size play a role in the reactivity of the material. The more surface area leads to more reactant sites. Kamenetskii calculated the influence of particle geometry on reactivity. In his equation, geometries are associated with a specific reactivity constant δ[31].

$$\delta = \frac{h_P - h_F}{\lambda}\frac{E}{RT_w^2}r_0^2\rho f exp(\frac{-E}{RT})$$

The higher the value of δ, the more reactive it is for combustion due to the increase surface area. This can be attributed to increased surface area to volume ratio, The constants for simple geometries are shown in Table 4.2. Amongst these geometries, it was found that materials that have a spherical form have a higher reactivity than other objects.

The combustion sequence is further expedited when spherical metals are reduced to powder form[33]. Powder explosives are more violent than their bulk counterpart because the increased surface area offers more locations for vapor generation and reaction[19]. The sequence for an explosion includes initiation, propagation, and termination. Due to this higher risk of combustion, many studies have looked into the flammability of metal powders: Zn is included in this list. Like many metal powders, zinc powder is considered an explosive because it will rapidly combust upon ignition. Zinc powder is classified as a Class-2[19] explosive meaning which will only burst and burn violently at a local level. At the bulk level, the minimum ignition temperature is 680°C. In powder form, the minimum temperature is 460°C[34].

4.3 Experimental Plan

To demonstrate that SHS (combustion) as a possible process for an efficient and robust method for the hybridization of ZnO nanostructures on carbon fiber, a heat transfer method will be used to ignite and combust zinc powder on carbon fiber. The source of the heat transfer will be carbon fiber through resistive heating. As was mentioned in chapter 1, carbon fiber was chosen because it is a good material for structural applications. Properties such as low density, high tensile strength, and high modulus make carbon fiber attractive. Carbon fiber also has good electoral conductivity. The carbon fiber under investigation is Cytec T300 which has a resistivity of 18 μΩm[35]. Thus upon subjected current flow, carbon fiber will experience joule heating. This will allow for carbon fiber to be used as the substrate and as the heat transfer source[36]. The set up would require the carbon fiber to be connected to a D.C. current through two electrodes. A diagram of this experimental setup is shown in figure 4.5.

Joule heating is defined by the Heat and Ohm's law equations[37]:

$$H(J) = C_p m \Delta T$$

$$P = \dot{U} = VI = I^2 R \ (Watt)$$

$$U = Pt = VIt = C_p m \Delta T$$

where H is the heat generated, C_p is the heat capacity under constant pressure, m is the mass, and ΔT is the change in temperature. Ohm's law shows the power relation to the energy rate ($\dot{U}$), Voltage (V), current (I), and resistance (R). This can then be related back to energy (U)[38]. The resistance can be determined when the length, L_S, and the cross sectional area, A_S, are known.

$$R = \rho L_s / A_S$$

Temperature vs power and resistance curves were measured and are displayed in figure 4.7. A digital pyrometer and a standard laboratory digital multi-meter were used to make the respective temperature and electrical measurements. The temperature of joule-heated carbon fiber reaches above 800°C which is above the necessary temperature to ignite Zn at the bulk and powder through heat transfer.

The zinc precursor used in this work comes from galvanizing spray paint composed of zinc powders with diameters less than 2-10μm. The spray paint is 93% pure zinc and contains trace elements. For inorganic paint, Zn powders are mixed in with silicates. Specialized lithium or potassium silicates are used for self-curing applications[18].

A topic of concern for Zn combustion on carbon fiber is the possibility of galvanic reaction between the Zn and carbon fiber. Carbides are very prevalent amongst metals especially aluminum. Fortunately for this system, Zn does not form carbides. Thus there will not be any reaction between Zn and carbon. However, successful hybridization via combustion still needs to be proven followed by characterization to prove that Zn carbides and Zn nitrides are not formed.

Ultimately, a combustion process is the key for the scaling up the hybridization of ZnO nanostructures on carbon fiber. The method is performed in atmospheric conditions where the substrate (carbon-fiber) serves as the heating source and transfers heat to the zinc powers. The oxygen supply would come from the atmospheric conditions that were shown in table 4.1. The precursor as already mentioned comes from galvanizing spray paint. This can be found in local hardware stores. The production time is reduced from hours to a matter of minutes (including preparation time) for each sample. The reaction time takes place in a manner of seconds, which is up to four-orders for magnitude faster than the reaction period for CVD and Hydrothermal reaction.

4.4. Conclusion

This change in method approach will reduce the cost of hybridization of ZnO nanostructures on carbon fiber. This method eliminates the need for vacuum or autoclave components, uses a common material as a precursor material, and reduces production time. The next 2 chapters discuss the results of ZnO hybridization on carbon fiber. Chapter 5 will discuss importance of the heat transfer rate to ignite the zinc powder. The results will be characterized by scanning electron microscopy (SEM), transmission electron microscopy (TEM), and X-Ray Diffraction (XRD). Chapter 6 will discuss possible mechanism of the nanostructure observed in the joule heating hybridization of ZnO nanostructures on carbon fiber. Many of these nanostructures can be related to the work performed through vacuum thermal oxidations and CVD methods.

4.5. Figures

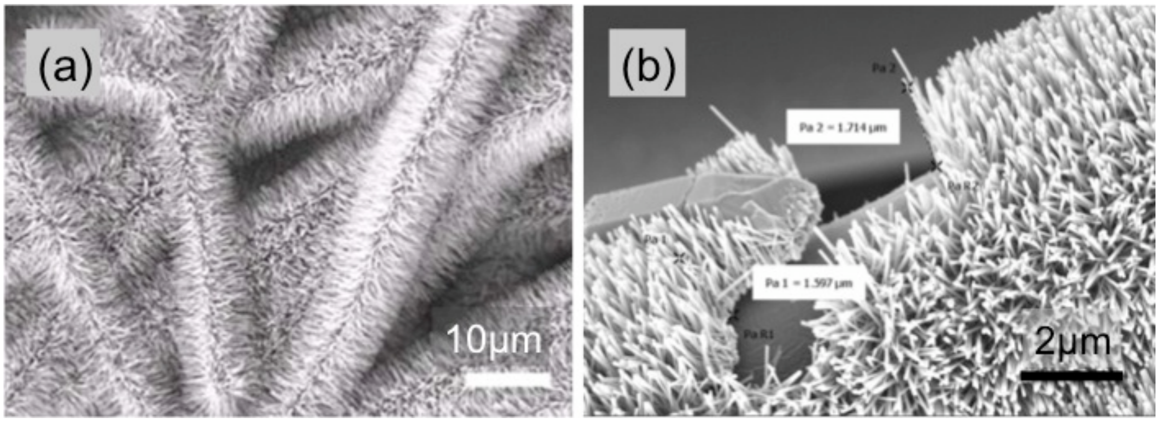

Figure 4. 1: (a) An SEM image shows carbon fiber hybridized with a uniform array of ZnO nanowires through a CVD method[1]. (b) A SEM image shows a similar carbon fiber hybridized with a uniform array of ZnO nanowires developed through a hydrothermal process[10].

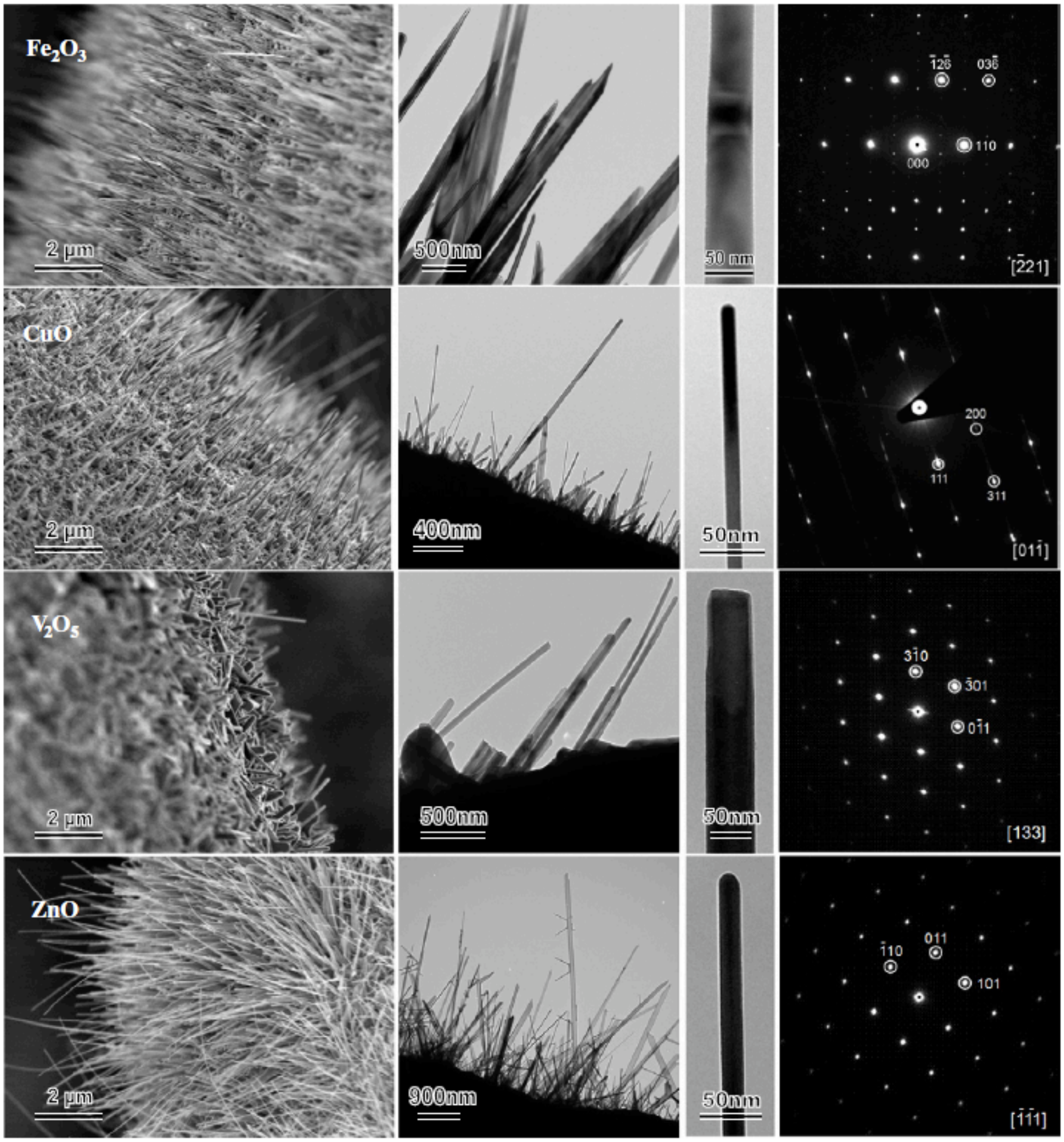

Figure 4. 2[24]: SEM and TEM images of metal oxide nanostructure grown through resistive heating.

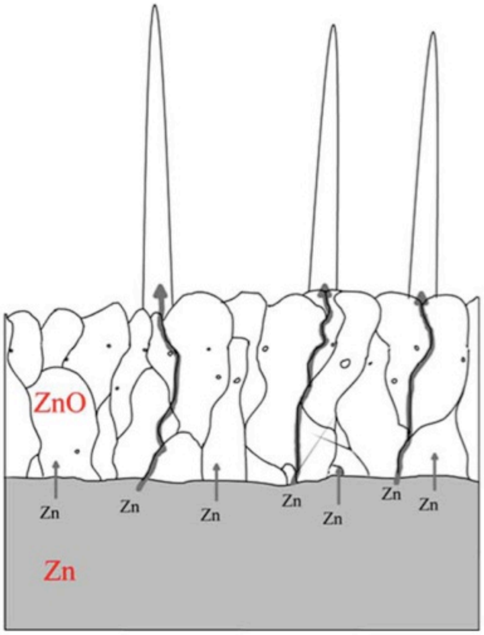

Figure 4. 3[25]: The figure shows ZnO nanowire growth through a two-step growth mechanism. Zn ions diffuse through the ZnO grain boundaries. At the surface, the ions begin to diffuse ZnO seeds. ZnO TEM pictures from Figure 4.2 shows the nanowires grew in the [0001] direction.

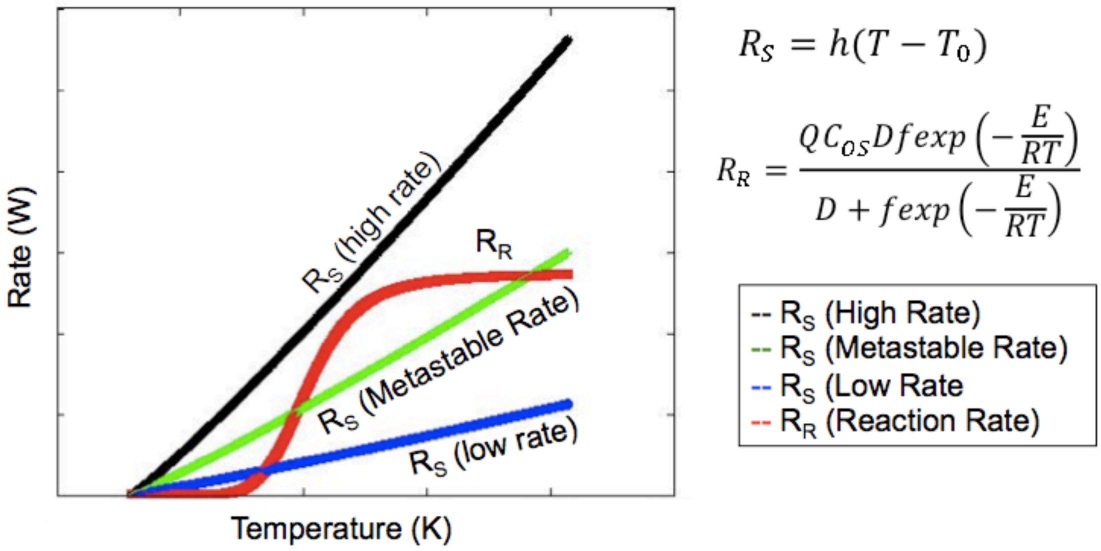

Figure 4. 4[31]: The first heat transfer curve is left the reaction curve indicating combustion. The lowest heat transfer curve is to the right of the reaction curve, representing a diffusion (oxidation) reaction. The curve that penetrates the reaction curve is in a region that is in a metastable region where both combustion and diffusion (oxidation) reactions occur.

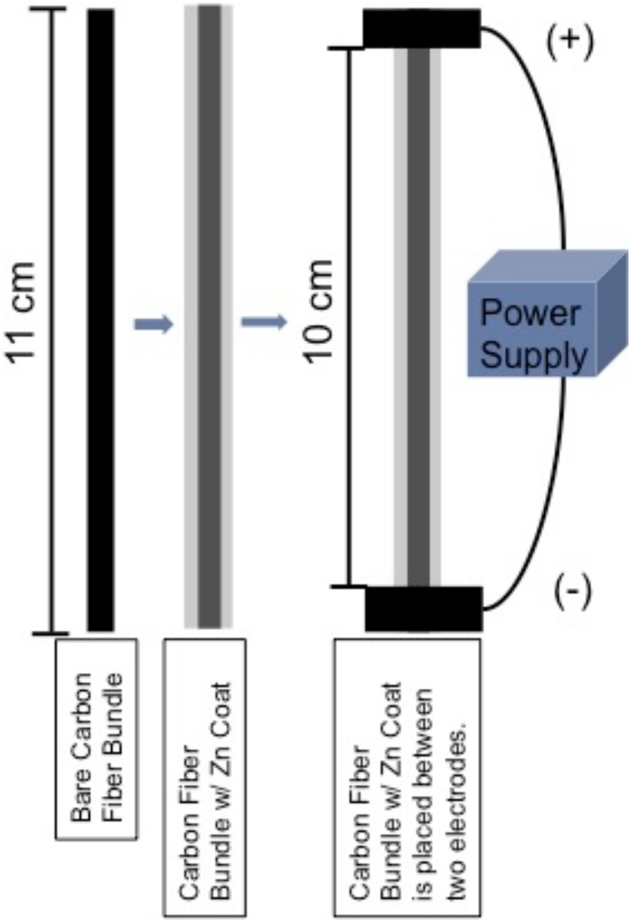

Figure 4. 5: A diagram of experiment shows bare carbon fiber bundles coated with the zinc powders. The coated carbon fiber is then placed between two electrodes and subjected to joule heating.

Table 4. 1: Elemental and molecular breakdown of the atmospheric contents.

Element	**Percentage**
Nitrogen	78.083
Oxygen	20.945
Ar	0.934
CO2	0.035
Ne	0.001818
H2	0.000055
Kr	0.000114
He	0.000524
CH4	0.0001745
Sum	**100.000**

Table 4. 2[31]: Kamenetskii's reactivity values for different geometries

Geometry	δ
Infinite Slab	0.88
Infinite Rod	2
Spherical object	3.32

4.6. References

1. Unalan, H. E.; Wei, D.; Suzuki, K.; Dalal, S.; Hiralal, P.; Matsumoto, H.; Imaizumi, S.; Minagawa, M.; Tanioka, A.; Flewitt, A. J., Photoelectrochemical cell using dye sensitized zinc oxide nanowires grown on carbon fibers. *Applied Physics Letters* **2008,** *93* (13), 133116.
2. Chen, H.; Zhu, L.; Liu, H.; Li, W., Growth of ZnO nanowires on fibers for one-dimensional flexible quantum dot-sensitized solar cells. *Nanotechnology* **2012,** *23* (7), 075402.
3. Alipour Skandani, A.; Masghouni, N.; Case, S.; Leo, D.; Al-Haik, M., Enhanced vibration damping of carbon fibers-ZnO nanorods hybrid composites. *Applied Physics Letters* **2012,** *101* (7), 073111-073111-4.
4. Skandani, A. A.; Masghouni, N.; Al-Haik, M., Superior Damping of Hybrid Carbon Fiber Composites Grafted by ZnO Nanorods. In *Topics in Modal Analysis, Volume 7*, Springer: 2014; pp 187-193.
5. Shen, G.; Bando, Y.; Lee, C.-J., Synthesis and Evolution of Novel Hollow ZnO Urchins by a Simple Thermal Evaporation Process. *The Journal of Physical Chemistry B* **2005,** *109* (21), 10578-10583.
6. Wang, Z. L., Zinc oxide nanostructures: growth, properties and applications. *Journal of Physics: Condensed Matter* **2004,** *16* (25), R829-R858.
7. Yao, B.; Chan, Y.; Wang, N., Formation of ZnO nanostructures by a simple way of thermal evaporation. *Applied Physics Letters* **2002,** *81* (4), 757-759.
8. Merzhanov, A.; Borovinskaya, I., A New Class of Combustion Processes†. *Combustion Science and Technology* **1975,** *10* (5-6), 195-201.
9. Sheppard, L., Powders That" Explode" Into Materials. *Adv. Mater. Process.* **1986,** *2* (2), 25-32.
10. Skandani, A. A.; Masghouni, N.; Case, S.; Leo, D.; Al-Haik, M., Enhanced vibration damping of carbon fibers-ZnO nanorods hybrid composites. *Applied Physics Letters* **2012,** *101* (7), 073111.
11. Quintiere, J. G.; Walters, R. N.; Crowley, S., *Flammability Properties of Aircraft Carbon-Fiber Structural Composite*. Office of Aviation Research and Development, Federal Aviation Administration: 2007.
12. Brown, M. E., ZnO-Rediscovered. **1957**.
13. Yi, H.; Moore, J., Self-propagating high-temperature (combustion) synthesis (SHS) of powder-compacted materials. *Journal of materials Science* **1990,** *25* (2), 1159-1168.
14. Cyr, H. M., Zinc oxide. US Patent 2,200,873: 1940.
15. Zanotti, L.; Calestani, D.; Villani, M.; Zha, M.; Zappettini, A.; Paorici, C., Vapour‐phase growth, purification and large‐area deposition of ZnO tetrapod nanostructures. *Crystal Research and Technology* **2010,** *45* (6), 667-671.
16. Zha, M.; Calestani, D.; Zappettini, A.; Mosca, R.; Mazzera, M.; Lazzarini, L.; Zanotti, L., Large-area self-catalysed and selective growth of ZnO nanowires. *Nanotechnology* **2008,** *19* (32), 325603.

17. Beever, P. F., Self-heating and spontaneous combustion. *The SFPE Handbook of Fire Protection Engineering* **1995,** *2*, 2-189.

18. Porter, F., Zinc Handbook: properties, processing, and use in design. *Marcel Dekker, Inc, 270 Madison Ave, New York, New York 10016, USA, 1991. 629* **1991**.

19. Eckhoff, R., *Dust Explosions in the Process industries*. 2 ed.; Butterworth Heinemann: Oxford, 1997.

20. Zong, F.; Ma, H.; Ma, J.; Du, W.; Zhang, X.; Xiao, H.; Ji, F.; Xue, C., Structural properties and photoluminescence of zinc nitride nanowires. *Applied Physics Letters* **2005,** *87* (23), 233104-233104-3.

21. Bloxam, C. L.; Lewis, S. J., *Chemistry, inorganic and organic, with experiments*. Blakiston: 1913.

22. Shulzhenko, A.; Ignatyeva, I. Y.; Osipov, A.; Smirnova, T., Peculiarities of interaction in the Zn–C system under high pressures and temperatures. *Diamond and related materials* **2000,** *9* (2), 129-133.

23. Xu, F.; Liu, X.; Tse, S. D.; Cosandey, F.; Kear, B. H., Flame synthesis of zinc oxide nanowires. *Chemical Physics Letters* **2007,** *449* (1), 175-181.

24. Rackauskas, S.; Nasibulin, A. G.; Jiang, H.; Tian, Y.; Kleshch, V. I.; Sainio, J.; Obraztsova, E. D.; Bokova, S. N.; Obraztsov, A. N.; Kauppinen, E. I., A novel method for metal oxide nanowire synthesis. *Nanotechnology* **2009,** *20* (16), 165603.

25. Rackauskas, S.; Nasibulin, A. G.; Jiang, H.; Tian, Y.; Statkute, G.; Shandakov, S. D.; Lipsanen, H.; Kauppinen, E. I., Mechanistic investigation of ZnO nanowire growth. *Applied Physics Letters* **2009,** *95* (18), 183114.

26. Gaskell, D. R., *Introduction to the Thermodynamics of Materials.* CRC Press: 2008; Vol. 2.

27. Dean, J. A., Lange's chemistry handbook. *McGraw-Hill, Inc* **1999,** *4*.

28. Barin, I., Thermodynamic Data of Pure Substances, 1989. *VCH, New York*.

29. Zeldovich, Y.; Semenov, N., Kinetics of chemical reactions in flames. **1946**.

30. Thorne, P., The physics of fire extinguishment. *Physics in Technology* **1985,** *16* (6), 263.

31. Frank-Kamenetskii, D. A. b. *Diffusion and heat exchange in chemical kinetics*; University press: 1955.

32. Hetnarski, R. B.; Eslami, M. R., *Thermal Stresses--Advanced Theory and Applications: Advanced Theory and Applications*. Springer: 2008; Vol. 158.

33. Mitsui, R.; Tanaka, T., Simple Models of Dust Explosion. Predicting Ignition Temperature and Minimum Explosive Limit in Terms of Particle Size. *Industrial & Engineering Chemistry Process Design and Development* **1973,** *12* (3), 384-389.

34. Jacobson, M.; Cooper, A. R.; Nagy, J. *Explosibility of metal powders*; DTIC Document: 1964.

35. THORNEL® T-300 PAN-BASED FIBER TECHNICAL DATA SHEET. Cytec, Ed. 2012; p 2.

36. Fukai, J.; Hamada, Y.; Morozumi, Y.; Miyatake, O., Effect of carbon-fiber brushes on conductive heat transfer in phase change materials. *International Journal of Heat and Mass Transfer* **2002,** *45* (24), 4781-4792.
37. Browne, M. E.; Browne, M. E., *Schaum's Outlines: Physics for Engineering and Science*. McGraw-Hill: 2010.
38. Gupta, A.; Harrison, I., New aspects in the oxidative stabilization of PAN-based carbon fibers. *Carbon* **1996,** *34* (11), 1427-1445.

Chapter 5: ZnO Nanostructures Grown on Carbon-Fiber through Joule-Heating

5.1. Introduction

Multifunctional composites offer new opportunities to reduce the weight of structural materials[1]. Fiber reinforced composites (FRCs), over the last few decades, have been popular candidates for structural applications to help reduce weight for many applications especially in the aerospace industry. Compared with metal alloys, FRCs offer improved tensile strength, modulus, and lower density. However, applications continue to demand for greater weight reduction, requiring new materials research and engineering. One approach to help reduce weight is through multifunctional composites or smart materials. Analogous to the smartphone revolution (where a multifunctional device has the same capabilities but has less collective weight in comparison with separate singular functional devices)[2]. A multifunctional composite has the same potential to offer an overall weight reduction by eliminating redundancies through added functionalities. A good example of a recent multifunctional composite is carbon fiber hybridized with carbon nanotubes (CNT). The CNTs offer addition functionality through additional strength, capacitance, catalyst, and piezoresistivity.

Like CNTs, Zinc Oxide is a promising candidate for added functionality to FRCs[3-4]. For the past century, ZnO has been a material of interest for its wide-ranging properties. ZnO is a stoichiometric material. Its most common phase, wurtzite (WZ) has a natural perovskite structure based on its lattice parameters a=3.2494Å and c=5.2038Å[5]. ZnO a natural piezoelectric material because its c/a ratio is 1.602, which is off from the ideal hexagonal c/a ratio of 1.633[6]. This offset creates a natural polarization which makes ZnO a piezoelectric. In addition, ZnO has a high bandwidth of 3.7eV making it a strong candidate for ultraviolet photovoltaics[7]. Although ZnO's properties have been known for nearly a century, ZnO research has made significant progress in the past decade to understand ZnO's anisotropic nature and its wide-ranging scope of nanostructures[8] including: sea-urchins, nanowires, sheets, tetrapods. These nanostructures offer more surface area to volume ratio, which results in more efficient and tunable properties.

Many fabrication techniques and substrates have been used for ZnO nanostructure synthesis[9]. Some techniques include: thermal oxidation[10], chemical vapor deposition[11], hydrothermal deposition[12], and flame synthesis[13]. Each technique offers a specific set of advantages and disadvantages. Various substrates have been used to understand ZnO nanostructure growth[10-13]. Those efforts have showed a lack of substrate selectivity for successful ZnO nanostructure nucleation and growth. This has spurned the idea of using carbon fiber as a substrate to introduce photovoltaic functionalities in carbon fiber composites. Groups have demonstrated successful hybridization of ZnO nanowires using CVD[14] and hydrothermal processes[3]. Unfortunately, these hybridization processes are expensive, time consuming, and low yielding.

A low-cost and robust fabrication technique to produced ZnO nanostructures on carbon fiber that has not yet been explored in depth is Zn powder combustion under atmospheric conditions[15]. Zn powders are well known dust explosives[16]. The Zn explosion is heavily influenced by a variety of factors, which include: Zn high vapor pressure (0.1 torr at 419°C), available oxygen, and particle size, and ignition source. The Zn combustion reaction is driven by a highly exothermic reaction with Zn and O_2[16]. Despite the similarity of the basic Zn oxidation/ combustion reaction equation, shown below:

$$Zn + \frac{1}{2}O_2 \rightarrow ZnO$$

combustion is different than oxidation because it requires an ignition source which can come through sufficient heat transfer or sparks. Without an ignition source, oxidation will occur through a diffusion mechanism.

In this work, carbon fiber is coated with Zn powders. Then the carbon fiber is joule-heated to heat and ignite the Zn powder. The required heating rate through joule-heating for combustion and the ZnO nanostructures associated with this reaction are to be determined. At sufficient loads of joule-heating, Zn will ignite and explode. The explosion will cause the Zn to vaporize and react with the atmospheric O_2 while giving off a sudden burst of localized heat for short duration until the metallic Zn is consumed.

5.2. Experimental Setup

The materials used in this experiment include: commercial Cytec T300 carbon fiber (3K) bundle and commercial galvanization spray paint (93% pure Zn). The carbon fiber bundles were prepared in 11 cm strips and lightly coated with commercial galvanizing spray paint until no visible carbon fiber was present. The carbon fiber bundle would serve as the joule-heating source as well as the substrate for the ZnO nanowire synthesis. The heat capacity of carbon fiber is 0.19 Cal/g x °C the electrical resistivity of carbon fiber is known to be 1.7 x 10^{-3} $\Omega \times$cm[19].

To transform the Zn coat into ZnO nanostructures on the carbon fiber bundle, joule-heating was performed on the Zn-coated commercial fibers bundles. The ends of the bundles were placed between two electrodes of a standard laboratory power supply. The contact length between the carbon fiber and the electrode was 0.5cm. The exposed length of the Zn-coated carbon fiber was 10cm. A diagram of the experimental setup is shown in figure 1.

The Zn-coated carbon fiber bundles were heated at three joule-heating amperage rates: 0.05amp/s, 0.06 amp/s, or 0.07 amp/s. This translates into respective nonlinear power rates of -

0.0117(W/s^3)+0.045(W/s^2), -0.0169(W/s^3)+0.065(W/s^2), and -0.02303(W/s^3)+0.088(W/s^2). The respective internal bundle temperature rates, measured through a pyrometer, were found to be 24.8^{o}C/s, 28.6^{o}C/s, and 35.2^{o}C/s. The power supply was terminated if the Zn particles fully combusted or reached a maximum current of 1.7 amps. The synthesis was performed in ambient conditions.

In-situ measurements of the current, voltage, and temperature were recorded during the joule-heating experiments. The voltage and current were monitored by a digital multi-meter at a rate of 10 recordings per second. The current and voltage would enable determination of the power input in the system as well as the resistance using Ohm's law. The temperature of the surface of the zinc was recorded through LabVIEW using k-type thermocouples at a rate of 20 recordings per second. Due to the limitations of the thermocouple both in contact and in measurement, the absolute temperatures were not measured. However, the thermocouples did provide sharp contrast in the heating rates from the joule heating and from the combustion reaction. This sharp contrast was used as a time marker to indicate when the moment of ignition. It must be noted that this contrast could not be observed by the pyrometer due to different emissivity values of the carbon fiber and the zinc particles. From the time scale of the reaction, the electrical measurements could be correlated to temperature changes produced by Zn combustion.

Weight measurements, Scanning Electron Microscopy (SEM) and Powder X-ray Diffraction (XRD) characterization were performed on each bundle before and after joule-heating. The weight measurements were used to measure the weight gain/loss from the reaction through a precision scale. Since the reaction region's length was 10cm, the preheated specimen weights were extrapolated for 10cm specimens. SEM was used to observe the microstructure of the Zn powder, morphology changes of the Zn powders from joule-heating; and measure the thickness of the Zn coat, and the diameters of the carbon fibers, Zn powders, and ZnO products. Within the SEM, the chemical composition was analyzed through Energy- Dispersive X-ray Spectroscopy (EDS). For crystallographic information, XRD (Cu $\lambda_{\kappa\alpha}$=1.5418Å) was used to measure the Zn to ZnO transformation, using Zn's known lattice parameter of 2.660Å.

Upon discovery of ZnO nanostructures, transmission electron microscopy (TEM) was used to analyze the growth direction of the Zn oxide nanostructures. TEM sample preparation involved the physical removal of ZnO from the carbon fiber onto a holey carbon film copper grid.

5.3. Results

Prior to joule-heating, the microstructure and crystallographic characterization of the carbon fiber and the Zn-coated carbon fiber were observed and are shown in figure 2. In figure 2a, the SEM, the Commercial Cytec T300 carbon fiber appeared to be a tight bundle, covered with sizing. The fibers were measured to be 5µm in diameter. The Zn pigment coat, shown in figure 2b, consisted of Zn powders, 2-20µm in diameter. The average thickness of the Zn coat was measured to be 60µm. For the most part, the coat appeared to have fully covered the fiber bundle. However, not all of the fibers were coated evenly. The inner fibers in the bundle were not covered by Zn particles. Higher magnification reveals that the Zn particles were coated in an adhesive organic binder. Under higher magnification shown in Figure 2c, the Zn particles appeared to have smooth surfaces with some surface oxidation. The oxidation layer appeared rougher and in some cases form hexagonal snowflake-like shapes, which can be related to ZnO's wurtzite structure. According to EDS (figure 2d), the binder, excluding had trace elements consisting of Al, Si, K, and Ca that make up less that 8% of the metal composition.

The trace elements are common for self-curing zinc paint. (frank porter) The XRD results, shown in figure 2e, verified the pre -heating oxidation of the Zn coated carbon fiber. The figure showed strong Zn peaks: $(10\bar{1}0)$, (0002), $(10\bar{1}1)$, and $(10\bar{1}2)$; and two small ZnO wurzite peaks: $(10\bar{1}0)$ and (0002). The peaks ratio indicated that there was little oxidation which compliments the SEM image shown in figure 2d. There were no diffraction peaks of crystalline carbon or other trace elements or compounds to be found.

5.3.1. Effect of Heating Rate on Combustion Behavior

The joule-heating experiment on Zn-coated carbon fiber produced two distinct results and an intermediate state. The first distinct result came from the lowest internal bundle joule heating-rate was 24.8^{o}C/s. No combustion occurred Zn-coated carbon fiber even when the carbon fiber glowed red and reached maximum-recorded temperature of 800^{o}C. The second distinct result came from the internal bundle joule heating-rate set at 35.2^{o}C/s; full combustion Zn combustion occurred. A surface temperature spike, and a visual bright flame identified this reaction. The distinct results were evident by visible discoloration, weight, resistance, reaction temperature, morphology, and crystallography. The intermediate result came from the heating where the internal bundle joule heating-rate was set at 28.6^{o}C/s. The Zn-coated carbon fiber experienced partial combustion occurred, where only some of the exposed region ignited, propagated, and terminated.

Visual observations on joule-heated Zn-coated fibers were denoted by color changes. The original Zn-coated carbon fiber had a light metallic finished. For joule-heating conducted at 24.8^{o}C/s, the Zn coat had developed a darker tarnished color, indicating oxidation occurred. For joule-heating conducted at 28.6^{o}C/s, the same darker tarnish color was observed with sporadic white spots. The white areas were areas of Zn combustion that had ignited but not fully propagated throughout the entire Zn-coated carbon fiber. Finally, for joule-heating conducted at 35.2°C/s, the metallic Zn coat on the carbon fiber transformed into a white powdery coat. Fueled by the atmospheric oxygen, the combustion sequence underwent ignition, propagation, and termination. As a result of full combustion, no tarnished metallic coat was found in the reaction region. Due to the combustion, some of the Zn material was expelled from the carbon fiber as white powder. The white powder is a strong indication of ZnO. An important note, only the exposed region showed discoloration, the section beneath the electrodes did not show accelerated oxidation. A schematic of these results are shown in figure 1.

In every case of joule-heating, a small trace of smoke would be produced at 100°C. The smoke could be traced back to the removal of sizing. Without the sizing, individual fibers would begin to separate from the carbon fiber bundle. However, individual fibers did not separate from the carbon fiber bundle when the there was a ZnO coat layer. It appears that the ZnO held the fiber bundle together despite the burning of the sizing.

There were clear weight differences between the preheated and the joule-heated specimens. Table 1 showed the average weights of the Zn-coated carbon fiber before joule heating, average weights after joule-heating, and percent of weight loss. For the specimens that underwent 24.8°C/s joule-heating, little change in weight was observed. The little change could be corresponded to the net effect between the loss of the sizing and adhesive of the carbon fiber bundle and the Zn pigment and the gain of oxygen through zinc oxidation. In the case with the joule-heating that underwent the highest tested heating rate of 35.2°C/s, an average 28% loss of mass was observed. This could be correlated to the explosive nature of zinc combustion. A violent force propelled particles to be expelled from the carbon fiber bundle. As for the joule-heating of 28.6^{o}C/s, mixed results were observed. Due to the partial combustion, a smaller portion of the original Zn coat was expelled.

The resistance and the corresponding outer surface temperature profiles of the three joule-heating age rates are shown in figure 3. The point of ignition was designated by a sudden shift in the heating rate. On the recorded time scale, the point of ignition was marked at zero. Prior to ignition, it was found that as the power increased, the resistance decreased. However, at the point of ignition of the Zn-covered carbon fiber, there was an inflection in resistance curve. As combustion continued, the resistance began to rise. In the first case where the internal heating rate is 24.6^{o}C, the surface heating-rate was measured to be 6.5^{o}C/s (shown in figure 6.3a). There was no temperature spike or inflection in the resistance curve indicating a combustion reaction, as seen in figure 6.3b. As expected, the current and temperature continued to increase there was a decrease in resistance.

In the joule-heating case with the internal bundle heating rate at 35.2^{o}C/s, the surface temperature profile showed combustion through a sharp change in the surface heating-rate from 16^{o}C/s to 400^{o}C/s. The point of ignition had been marked at the zero second, as seen in figure 3e. According to figure 3f, the resistance began to decrease with the increase in current, but began to increase at the point of ignition.

The intermediate joule-heating, at the internal bundle heating-rate at 28.6^{o}C/s, resulted in a metastable combustion reaction where some of the samples would combust and some would oxidize without combustion. When combustion occurred, like the case with the internal bundle heating-rate at 28.6^{o}C/s, the temperature profile showed a sharp change in heating rate. Correspondingly, the resistance began to increase when ignition occurred. For the samples that did not combust, like the case with the internal heating rate of 24.8^{o}C/s, the heating rate and the resistance did not have an inflection point. These rate changes or lack of rate changes can be seen in figure 3c and 3d.

5.3.2. Effect of Heating Rate on ZnO Microstructure

From a microscopic perspective, there were dramatic differences in the microstructure and nanostructures between the non-combusted and combusted samples. For the non-combusted samples resulting from the internal bundle heating-rate at 24.8^{o}C/s, the Zn particles showed significant oxidization through increased surface roughness and pitting (figure 4a) in comparison with the original Zn balls shown in figure 2d. Under higher magnification, small nanowires were found protruding from the oxidized Zn balls, shown in figure 4b. The thickness of the nanowires were10-50nm and the lengths were measured to be 100-500nm. The clusters and placement of these nanowires were sporadic where the density was 10/µm^2.

At the highest internal bundle heating-rate at 35.2^{o}C/s, the carbon fiber bundle was covered by ZnO nanostructures primarily composed of tetrapods and nanowires (figure 4g). No oxidized Zn balls with the rough surface and pits were found. The nanowires varied in diameter, ranging form 40- 200nm; and the lengths ranged from 500nm-5µm. At higher magnification, shown in figure 4h, the tetrapods appeared to be detached from the carbon fiber bundles and sat above a layer of ZnO nanowires. The legs of the tetrapods were very thin and were measured to be less than 50nm in diameter.

The intermediate internal bundle heating-rate at 28.6^{o}C/s, both types of morphologies were present, oxidized Zn particles and ZnO micro/nanostructures. A low magnification image (figure 4c) showed a section of the carbon fiber bundle where both the non-combusted and combusted portion were present. In the areas that had not combusted, oxidized Zn particles were found with surface roughness and pitting, as seen in figure 4d. Upon higher magnification, nanowires protruding from the oxidized Zn particles. The density of nanowires from the oxidized particles present was higher in comparison with the samples from the 0.05amps/s joule-heating rate. In the areas that had ignited, ZnO whiskers and nanostructures were present, as seen in figure 4e. The ZnO whiskers looked similar to the ZnO nanowires found in the samples heated by the internal bundle heating-rate at 35.2°C/s. At higher magnification, the nanowires were thicker in comparison with the nanowires, seen in figure 4f. The nanowires had diameters ranging from 200nm-1μm with lengths up to 15μm to be thicker. Surprisingly, tetrapods were not found readily available in intermediate case.

Under XRD, the relative intensities of ZnO peaks increased for each increase in joule-heating rate while the intensities of Zn peaks decreased in comparison with the preheated samples. The XRD results are shown in figure 5. The identified ZnO peaks included: $(10\bar{1}0)$, (0002), $(10\bar{1}1)$, $(10\bar{1}2)$, $(10\bar{1}3)$, $(2\bar{2}00)$, $(11\bar{2}2)$, and $(2\bar{2}01)$; and previous mentioned, the identified Zn peaks included: (0002), $(10\bar{1}0)$, $(10\bar{1}1)$, and $(10\bar{1}2)$. In the internal bundle heating-rate at 24.8°C/s sample set, shown in figure 5a, the rise in ZnO peak intensity could be attributed to the oxidation of the Zn particles. Likewise, the decease in Zn peak intensities could be accounted for the consumption of Zn through oxidation. For the internal bundle heating-rate at 28.6°C/s sample set, shown in figure 5b, the futher rise in ZnO peak intensity could be attributed to partial combustion that had transform Zn into Zn oxide nanostructures. Finally, in the internal bundle heating-rate at 35.2°C/s sample set, shown in figure 5c, there were only ZnO peaks present; no Zn peaks were identified. The Zn combustion thoroughly consumed all of the Zn and transformed them into ZnO nanostructures.

Though there had been a tremendous amount of TEM work on ZnO nanowires and its growth direction, it was nonetheless important to verify the growth direction for these nanowires produced by Zn combustion through joule-heating. Figure 6 showed a TEM image of a ZnO nanowire produced from the internal bundle heating-rate at 35.2°C/s specimen. Using double stage rotation, selected area electron diffraction (SAED) was taken of the particle showing two different zone-axis electron diffraction patterns were found: $[2\bar{1}\bar{1}0]$ and $[01\bar{1}0]$. Using the g vector, the nanowire was found to grow in the [0002] direction where $[2\bar{1}\bar{1}0] \perp [0002]$ and $[01\bar{1}0] \perp [0002]$. There were no identifiable metallic Zn reflections identified for this particular nanowire.

5.4. Discussion

The experimental results showed that the respective internal bundle heating-rates at 24.8°C/s, 28.6°C/s, and 35.2°C/s, produced stable oxidation, metastable combustion, and combustion results. The results of the these heating rates are well representative of Frank Kamenetskii's work on heat transfer and heat of reaction graph[18] shown in figure 7. For many systems, not just Zn particles, fast heating rates cause combustible materials to explode. At slow heating rates, stable reaction in the form of diffusion occurs. The precursor ignites when the heat of reaction (R_R) becomes equal or less than the heat supply rate (R_S). According to Kamenetskii, the rate of reaction describes the amount of heat released per unit surface area per unit time and will rise exponentially as temperature is increase. As temperature further decreases, the curve enters into the diffusion region where the reaction rate only slightly increases because it is dependent on the flow of gases. Using this model, the heating rate boundary conditions for auto-ignition of Zn combustion can be established.

R_R is defined by the following equation:

$$R_R = \frac{QC_{OS}Dfexp\left(-\frac{E}{RT}\right)}{D + fexp\left(-\frac{E}{RT}\right)}$$

where Q is the heat of reaction (700KJ/mol)[18], C_{OS} is the oxygen concentration, D is the thermal diffusion rate constant, f is the pre exponential or frequency factor, E is the activation Energy (J/mol), R is the gas constant 8.314 (J/mol K), T is the absolute temperature. Likewise, R_s can be defined by the following equation:

$$R_S = h(T - T_0)^n$$

where h is the heat transfer coefficient, T is the temperature of the carbon fiber, T_0 is the ambient temperature, and n is the exponential constant.

For this work, the internal bundle heating-rate at 24.8°C/s produces the curve R_S(oxidation), which is placed on the right side of the R_R curve; the internal bundle heating-rate at 28.6°C/s produces the curve R_S(metastable), which intersects with R_R curve at three points; and internal bundle heating-rates at 35.2°C/s produces the curve R_S(combustion), which is on the left side of the R_R curve. The joule-heating rate curves R_S(oxidation) and R_S(combustion) serve as the boundary conditions for thermal oxidation combustion reaction, or a metastable reaction. For joule-heating rates that are greater than the R_S(combustion) curve, the prepared Zn-coated carbon fiber always resulted in full combustion. In cases of heating rates that are below the R_S(oxidation) curve, the prepared Zn-coated carbon fiber always resulted in full oxidation. The joule-heating was terminated before the specimens decomposed. Between these boundary heating rate conditions, the Zn-coated carbon fiber reaction was metastable, where both thermal oxidation and combustion occurred.

When correlating these observations to the characterization results, there is a clear understanding of why low heating rates of Zn particles do not result in explosive combustion. Upon looking at the microstructures through SEM, the increase surface roughness and pitting of the Zn balls implies thermal oxidation occurred, where atomic diffusion was the major mechanism. As Zn was consumed by thermal oxidation, less material was susceptible for combustion. In addition, the growing oxide shell acted as a barrier for the trapped Zn to vaporize and spontaneous ignite and explode. From the XRD, readings, it was clear that there was still Zn, not all of it had been consumed. Thus, even at high temperature exposure that would have normally ignited Zn particles, there was either not enough Zn to be vaporized or the Zn was trapped behind the ZnO barrier. In the case with higher heating rates, it was clear through the SEM, the Zn combustion produced ZnO nanostructures. This nanostructure growth technique has been well known in the ZnO industry, but hybridization with carbon fiber through the joule-heating has not been attempted. XRD also showed that the combustion was thorough with Zn consumption as no Zn reflection peaks were obtained.

From the weight measurements, there was an observed lack of weight conservation. In the non-combusted material, the final weight showed loss between 2-8%. Interestingly, despite the reaction of the oxygen during oxidation, the weight did not increase. Instead, the net weight loss could be accredited to the burning of the sizing and adhesive. For the fully combusted samples, there was a 25-35% weight loss. This higher percentage loss was derived from the ejected powder. Since Zn is a Class-2 explosive, mass transfer from shock forces was part of the nature of combustion. From SEM analysis, the powders appeared to be independent ZnO tetrapods. For the partial combusted samples, the weight lost was between these two extremes. A lack of tetrapods could explain the lower loss in mass.

The XRD findings showed no other reflections from other elements or compounds. There are a couple of possibilities for the lack of trace elements that were found through EDAX. First, the adhesive of the paint could have been amorphous, thus showing no reflections based on periodicity. Second, the pigment adhesive, like the sizing, could have burnt off during joule-heating.

It was found in this report, the averaged measured ignition temperatures was 270°C, well below the known Zn's melting temperature of 419°C. According to many pure Zn data sheets, explosivity or flammability is not expected until the temperature reaches the melting temperature**.** Based on joule-heating of the carbon fiber and the zinc powders, the calculated temperature reached more than 800°C at the point of ignition. This is well above the required temperature to melt and vaporize the zinc powders, which is required for Zn combustion. The difference in the recorded temperature and the calculated values could be a lack of direct contact with the thermocouple and the carbon fiber. The zinc powder layer acted as a barrier between the carbon fiber and the thermocouple. Despite the lack of direct contact, the thermocouple provided a direct time measurement that was used to locate the ignition and ultimate combustion.

In this effort, ZnO nanostructures were successfully grown on carbon fiber through joule-heating of zinc-coated carbon fiber bundles in atmospheric conditions. This technique offers a simple method to hybridized ZnO nanostructures on carbon fiber bundles, without expensive laboratory apparatus. In addition the processing time is seconds in comparison with other techniques that requires multiple hours. This hybridization process can also be potentially used for woven textile fabrics that possess resistive heating capabilities. Before these carbon fiber can be utilizes as effective multifunctional composites, the hybridization of ZnO nanostructures on carbon fiber bundles produced through joule-heating will need further study. These research areas include: growth mechanisms, mechanical properties, carbon fiber preservation, capacitance and piezo properties, and the interfaces of matrix materials and the hybridized carbon fibers for composite layup. These factors are important when considering potential industrial scale up production.

5.5. Conclusion

Joule-heating was applied on Zn-coated carbon fiber bundles to produce a layer of ZnO nanoparticles. This method is fast, simple, and inexpensive and can be applied to advance textiles for the creation of multifunctional composite applications. If the rate of joule-heating is below the threshold requirement, undesired oxidized zinc is produced. If the joule-heating rate is in the metastable region, there is only partial combustion of Zn. Thus, to produce, consistent layers of ZnO nanoparticles on carbon fiber bundles through combustion, sufficient a joule-heating rate must be applied. The thermal oxidized, metastable combusted, and fully combusted specimens were characterized chemically and microscopically through XRD, SEM, EDS, and TEM.

5.6. Figures

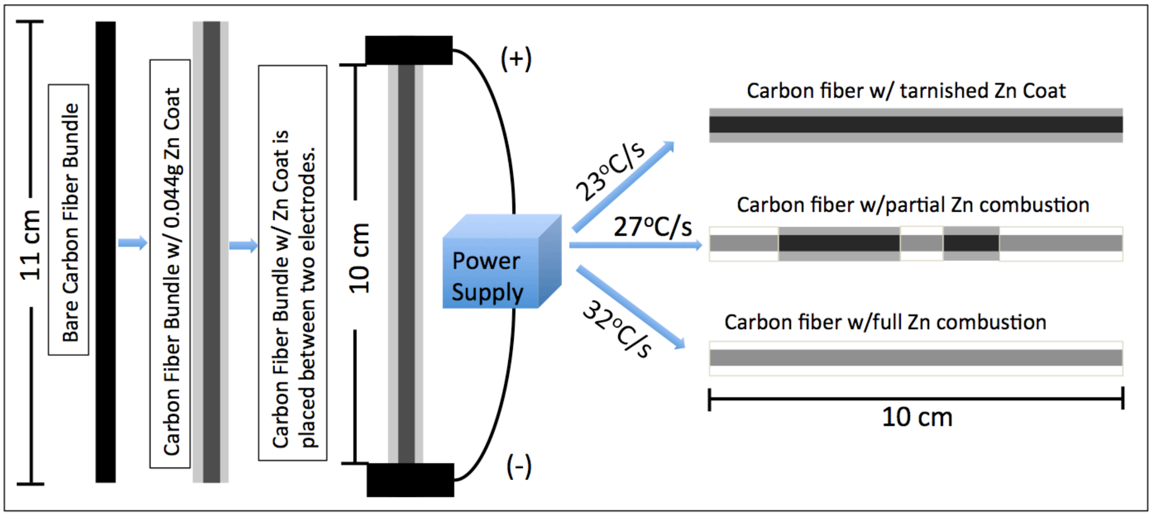

Figure 5. 1: This shows the experimental schematic where a bare carbon fiber is coated with zinc powders. It is then subjected to resistive heating at one of three amperage rates. The resulting reactions are either thermal oxidation, combustion, or a mixture of the reactions.

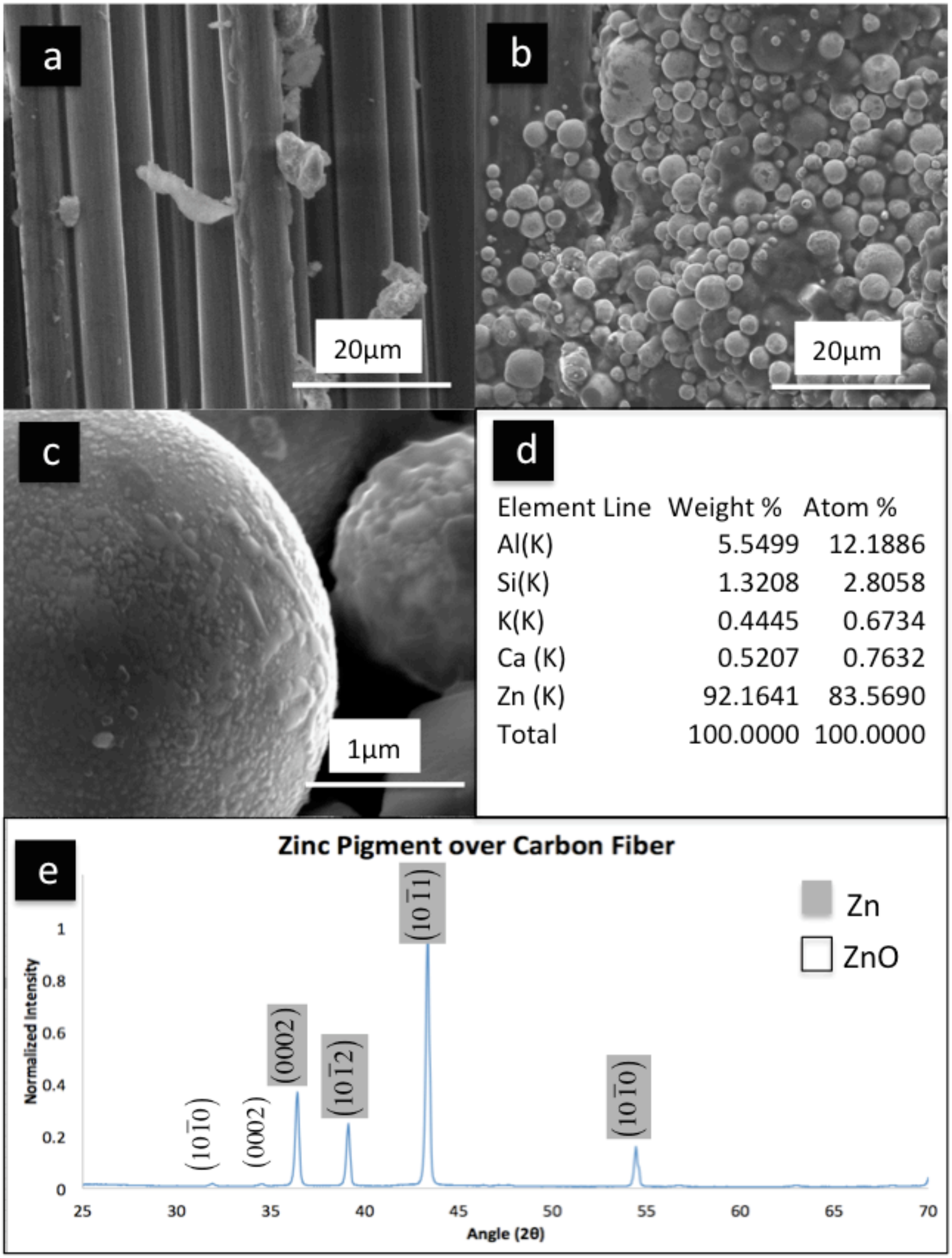

Element Line	Weight %	Atom %
Al(K)	5.5499	12.1886
Si(K)	1.3208	2.8058
K(K)	0.4445	0.6734
Ca (K)	0.5207	0.7632
Zn (K)	92.1641	83.5690
Total	100.0000	100.0000

Figure 5. 2: Preliminary Characterization of the carbon fiber and zinc powders were taken before joule heating. The carbon has a diameter of 5µm and is covered in sizing. The zinc powders range from 1-10µm in diameter. At high resolution, surface oxidation can be observed. EDX was taken of the zinc powders (carbon was excluded). XRD showed only metallic Zn and ZnO peaks of the carbon fiber coated with Zn powders.

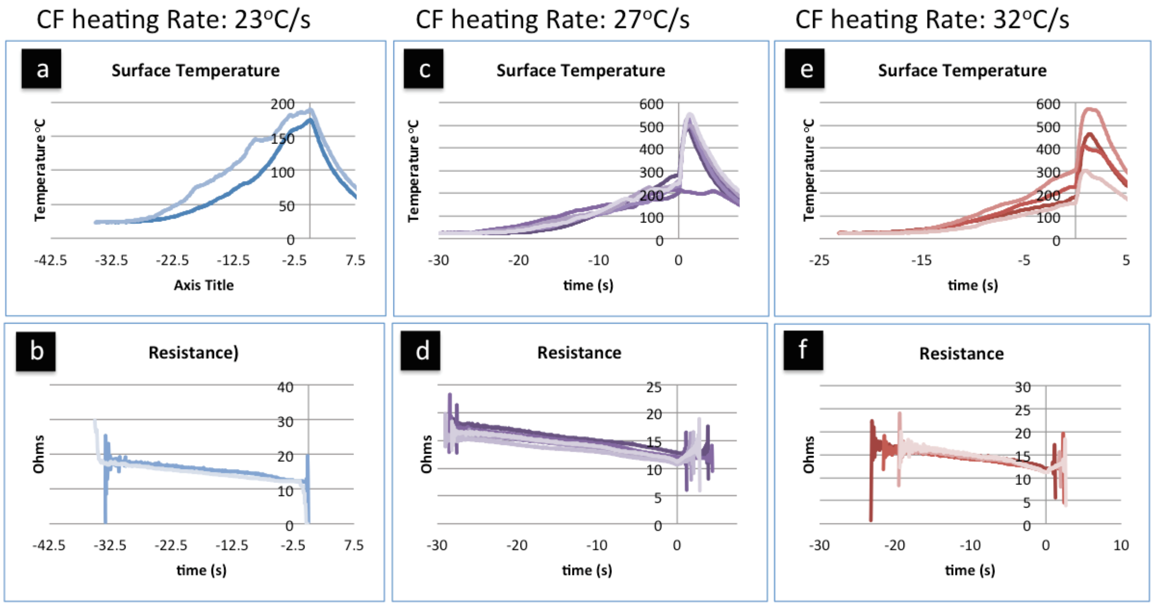

Figure 5. 3: This shows the surface temperature and resistance profile for the three different carbon fiber heating rates. Combustion is noted by an abrupt increase in the surface heating rate and an increase in the resistance. The lowest heating rate had no indication of combustion. The highest heating rate always indicated combustion occurred. The intermediate heating rate showed mixed results, indicating a metastable combustion.

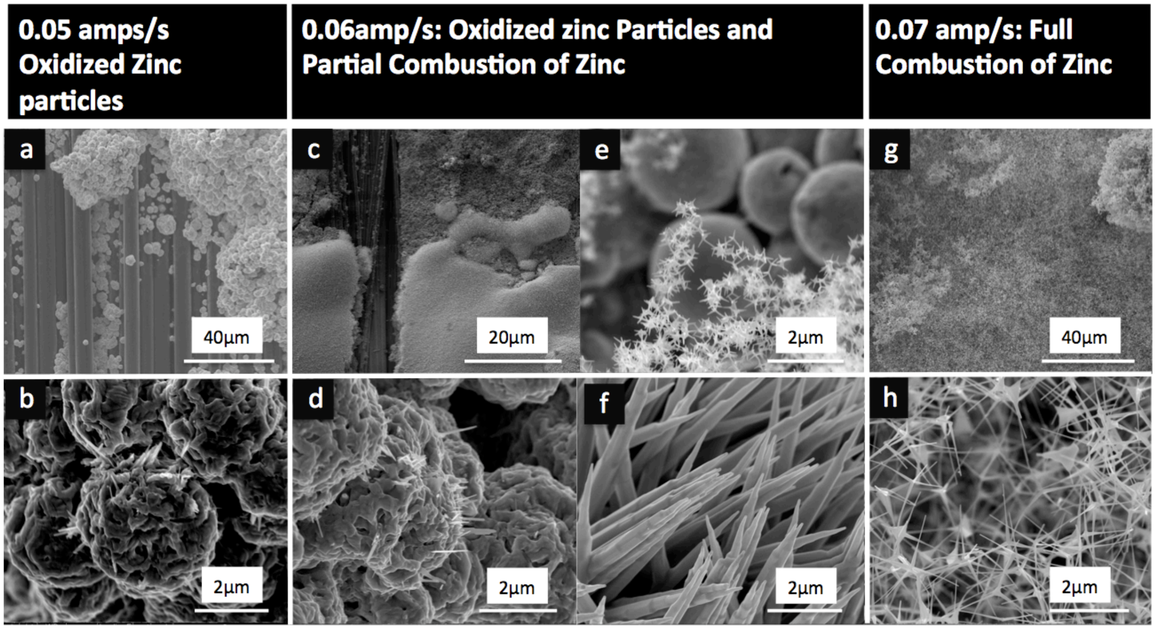

Figure 5. 4: SEM Profile of microstructure and nanostructures produced through joule heating of the Carbon fiber coated with Zn powder. At the lowest rate, the zinc powders show accelerated oxidation through the pitting on the surface. Small nanowires through diffusion growth are seen. At the middle rate, some areas show thermal oxidation through surface pitting, and some areas show combustion through ZnO nanostructures. At the highest rate, only ZnO nanostructures were found.

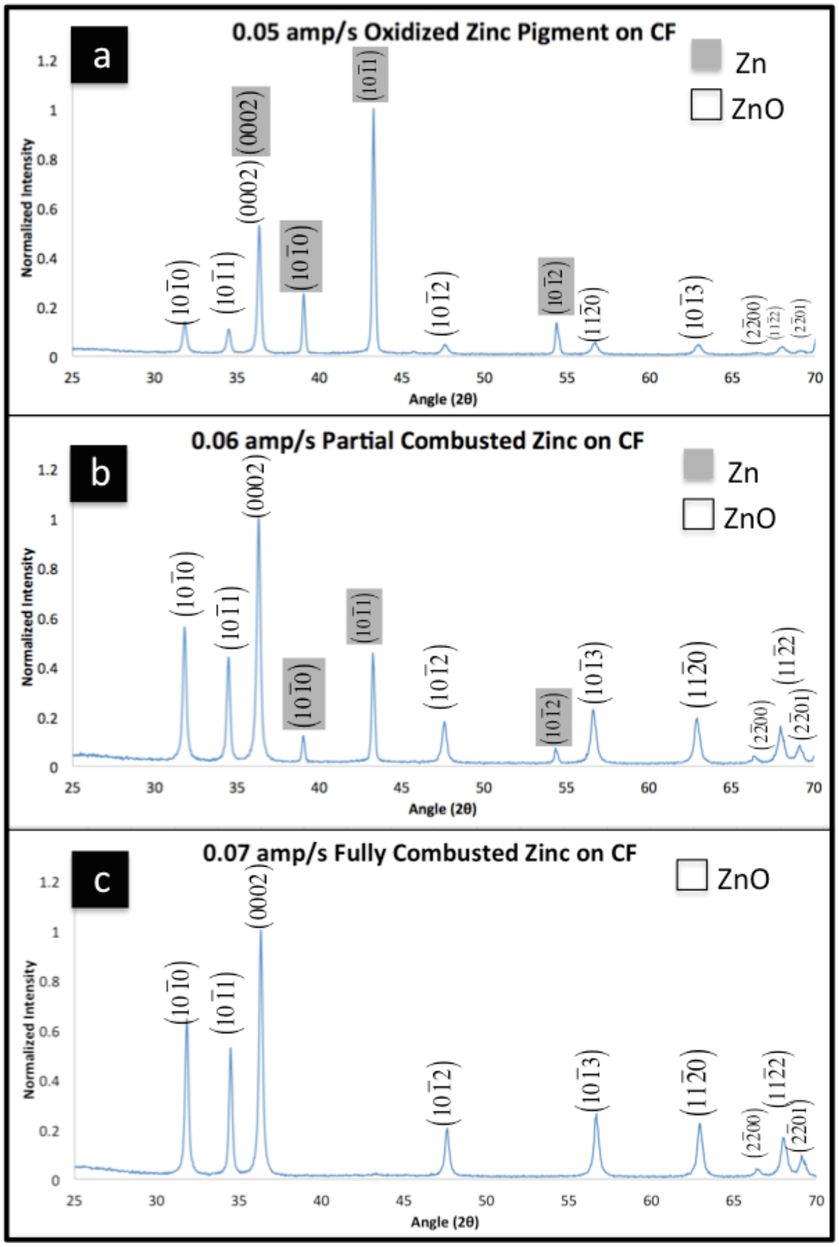

Figure 5. 5: XRD confirms the consumption of metallic zinc and the increase in ZnO. At the lowest heating rate, metallic zinc had not been fully consumed. At the metastable heating rate, the metallic Zn peaks have decreased as the ZnO peaks increased. At complete combustion, metallic zinc is consumed as it transforms into ZnO.

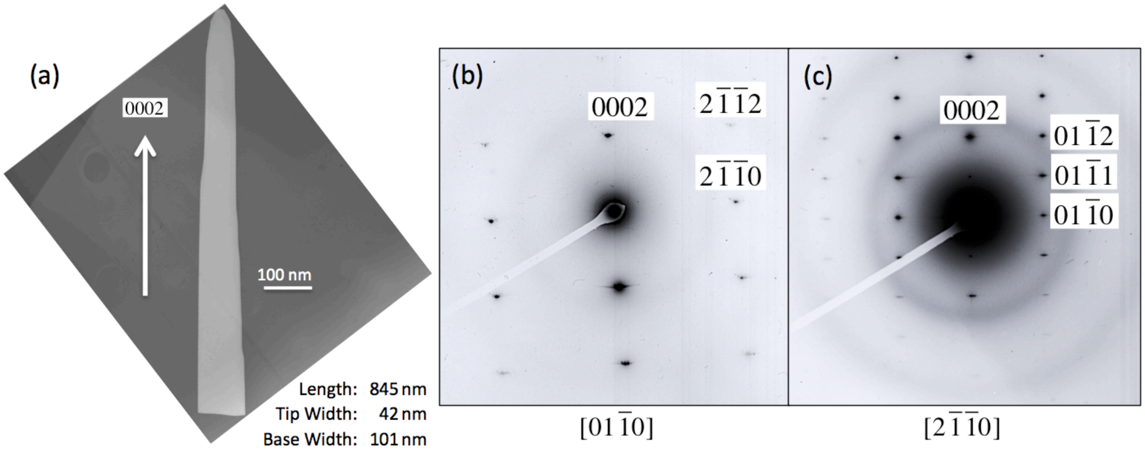

Figure 5. 6: A TEM image shows a ZnO Nanowire obtained through one of the samples. The growth of the ZnO was found to be in the (0001) direction through SAED.

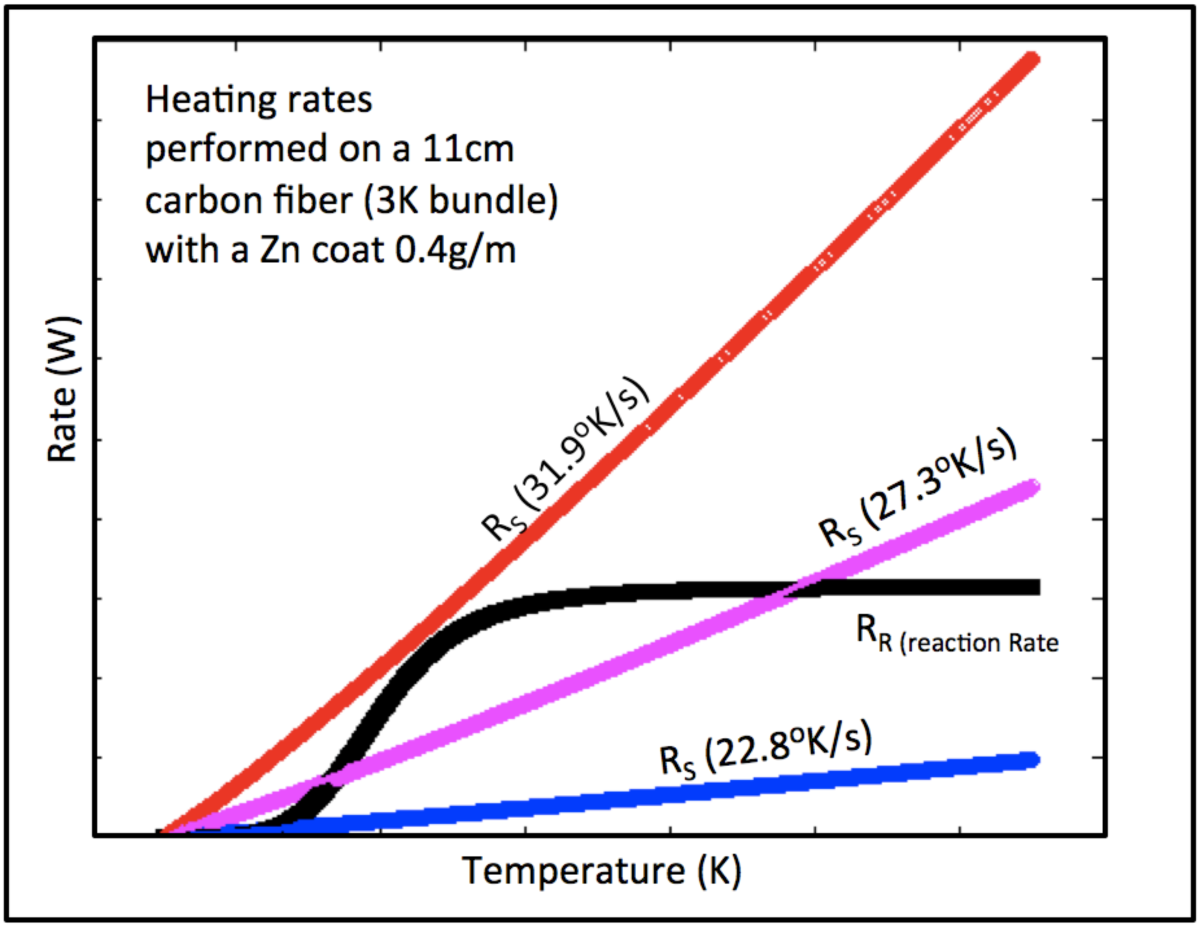

Figure 5. 7: A representation of Frank Kamenetskii's combustion modelwas plotted. The Supply rates are shown to be above, intersecting, or below the Reaction Rate (R_R). Above the (R_R), the reaction would result in combustion. Below the (R_R), the reaction would result in thermal oxidation. If the supply rate intersects with the (R_R) a metastable reaction occurs.

5.7. References

1. Gibson, R. F., A review of recent research on mechanics of multifunctional composite materials and structures. *Composite structures* **2010,** *92* (12), 2793-2810.
2. Falaki, H.; Mahajan, R.; Kandula, S.; Lymberopoulos, D.; Govindan, R.; Estrin, D. In *Diversity in smartphone usage*, Proceedings of the 8th international conference on Mobile systems, applications, and services, ACM: 2010; pp 179-194.
3. Chen, H.; Zhu, L.; Liu, H.; Li, W., Growth of ZnO nanowires on fibers for one-dimensional flexible quantum dot-sensitized solar cells. *Nanotechnology* **2012,** *23* (7), 075402.
4. Alipour Skandani, A.; Masghouni, N.; Case, S.; Leo, D.; Al-Haik, M., Enhanced vibration damping of carbon fibers-ZnO nanorods hybrid composites. *Applied Physics Letters* **2012,** *101* (7), 073111-073111-4.
5. O□zgu□r, U.; Alivov, Y. I.; Liu, C.; Teke, A.; Reshchikov, M. A.; Dog□an, S.; Avrutin, V.; Cho, S. J.; Morkoc□, H., A comprehensive review of ZnO materials and devices. *Journal of Applied Physics* **2005,** *98* (4), 041301.
6. Givargizov, E. I., Highly anisotropic crystals. **1987**.
7. McCune, M.; Zhang, W.; Deng, Y., High Efficiency Dye-Sensitized Solar Cells Based on Three-Dimensional Multilayered ZnO Nanowire Arrays with “Caterpillar-like” Structure. *Nano letters* **2012,** *12* (7), 3656-3662.
8. Wang, Z. L., Zinc oxide nanostructures: growth, properties and applications. *Journal of Physics: Condensed Matter* **2004,** *16* (25), R829-R858.
9. Fan, Z.; Lu, J. G., Zinc oxide nanostructures: synthesis and properties. *Journal of nanoscience and nanotechnology* **2005,** *5* (10), 1561-1573.
10. Ren, S.; Bai, Y. F.; Chen, J.; Deng, S. Z.; Xu, N. S.; Wu, Q. B.; Yang, S., Catalyst-free synthesis of ZnO nanowire arrays on zinc substrate by low temperature thermal oxidation. *Materials Letters* **2007,** *61* (3), 666-670.
11. Chang, P.-C.; Fan, Z.; Wang, D.; Tseng, W.-Y.; Chiou, W.-A.; Hong, J.; Lu, J. G., ZnO Nanowires Synthesized by Vapor Trapping CVD Method. *Chemistry of Materials* **2004,** *16* (24), 5133-5137.
12. Xu, S.; Wang, Z. L., One-dimensional ZnO nanostructures: Solution growth and functional properties. *Nano Research* **2011,** *4* (11), 1013-1098.
13. Tani, T.; Mädler, L.; Pratsinis, S., Homogeneous ZnO Nanoparticles by Flame Spray Pyrolysis. *Journal of Nanoparticle Research* **2002,** *4* (4), 337-343.
14. Unalan, H. E.; Wei, D.; Suzuki, K.; Dalal, S.; Hiralal, P.; Matsumoto, H.; Imaizumi, S.; Minagawa, M.; Tanioka, A.; Flewitt, A. J.; Milne, W. I.; Amaratunga, G. A. J., Photoelectrochemical cell using dye sensitized zinc oxide nanowires grown on carbon fibers. *Applied Physics Letters* **2008,** *93* (13), 133116-3.
15. Rackauskas, S.; Nasibulin, A. G.; Jiang, H.; Tian, Y.; Statkute, G.; Shandakov, S. D.; Lipsanen, H.; Kauppinen, E. I., Mechanistic investigation of ZnO nanowire growth. *Applied Physics Letters* **2009,** *95* (18), 183114.

16. Eckhoff, R., *Dust Explosions in the Process industries*. 2 ed.; Butterworth Heinemann: Oxford, 1997.
17. Gupta, A.; Harrison, I., New aspects in the oxidative stabilization of PAN-based carbon fibers. *Carbon* **1996,** *34* (11), 1427-1445.
18. Warnatz, J.; Maas, U.; Dibble, R. W., *Combustion: physical and chemical fundamentals, modeling and simulation, experiments, pollutant formation*. Springer: 2006.
19. THORNEL® T-300 PAN-BASED FIBER TECHNICAL DATA SHEET. Cytec, Ed. 2012; p 2.

Chapter 6: Growth Mechanisms of ZnO Nanostructures Hybridized on Carbon Fiber through Joule-Heating Induced Combustion

6.1 Introduction

In the previous chapter, it was shown that zinc oxide (ZnO) nanostructures can be synthesized on carbon fiber in a low-cost and highly reproducible procedure. Carbon fibers are hybridized with ZnO nanostructures for the creation of multifunctional composites[1,2]. To create hybridized carbon fibers, carbon fiber bundles are coated with Zn powders and followed by joule heating under atmospheric conditions. A minimum heating rate is required to ignite the Zn powders[3] to produce ZnO nanostructures. These nanostructures include tetrapods, sheets, nanowires, and hollow structures. If the minimum heating rate or minimum heat threshold were not reached, the zinc balls would undergo accelerated oxidation, but would not ignite or explode. Effort has been made to understand the minimum heating rate, but the growth mechanisms of these ZnO nanostructures are still to be determined. Schematics of the experiment and SEM images of the variety of ZnO nanostructures produced from this work are shown in fig 1.

Hybridized carbon fibers with ZnO nanostructures present a unique opportunity to develop multifunction composite. Each material, carbon fiber and ZnO, offers different sets of desired properties. Carbon fiber is a well-known lightweight structural material with a tensile strength of 1-7 GPa[4], a young's modulus of 230-900 GPa[5], and density of 1.7-2.2 (g/cm^3)[5]. It has a resistivity of 1.7 x 10^{-3} Ω×cm making a good candidate for resistive heating. In contrast to carbon fiber, ZnO is not a good structural material but is a well-known wide-band (3.7eV) semiconducting material[6]. It properties also exhibits piezoelectric[7], photovoltaic[8], and catalytic properties[9]. Zinc oxide has three different phases: wurtzite, zinc-blend, and rock salt, where the order is dictated of lower to higher states[10]. ZnO's basic synthesis is the combination of a zinc precursor and oxygen, shown below.

$$Zn^{2-} + \frac{1}{2}O_2 \rightarrow Zn$$

ZnO has received a recent wave of attention to the variety of nanostructures such as: tetrapods[11], ribbons[12], sheets[13], nanowires[14], and hollow urchins[15]. This variation of ZnO nanostructures can be traced back to Zn's high vapor pressure[16] (0.1 torr at 419°C). This results in high levels of sensitivity to different parameters such as heating rate, pressure, and oxygen content. ZnO is also naturally an anisotropic. All of these factors lead to the diverse array of nanostructures. By understanding the different ZnO nanostructure fabrication techniques, it is possible to match specific nano/microstructures produced by joule heating. From there, growth mechanisms can be proposed.

Traditional zinc oxide nanostructure fabrication methods include: thermal oxidation[17], Chemical Vapor Deposition (CVD)[6], flame synthesis[18], and hydrothermal process[19]. Amongst these methods, thermal oxidation and CVD have many similar ZnO nanostructures to those seen in zinc coated carbon fiber combustion reactions experiments. Thermal oxidation is based on diffusion, which is known to repeatedly produced ZnO nanowires[20], tubes[21], hollow spheres[22], and hollow sea urchins[23]. CVD is known to produce nanowires[24], sheets[13], ribbons[25], and tetrapods[26]. These two methods will serve as the models to explain the ZnO growth mechanisms hybridized ZnO nanostructures on carbon fibers.

6.2. Experimental Setup

For this work, the growth mechanism ZnO nanostructures through joule heating hybridization method is under investigation. To understand the ZnO nanostructures growth mechanisms on carbon fiber through explosion induced by joule heating, a series of different thicknesses of Zn precursor are applied to carbon fiber. The different thicknesses were labeled as light, medium, heavy medium, or heavy zinc coating. The respective weight gains for a 10cm sample were 0.025 g, 0.04 g, 0.05 g, and 0.06 g. A high precision scale took weight measurements of the coated carbon fiber, with an accuracy of 0.0001 grams. The weight was measured for 10cm long samples, representing the reaction region of the zinc-coated carbon fiber. Scanning Electron Microscopy (SEM) observation showed that the. SEM showed a variety of different zinc particles with diameters ranging from 2-20μm. Cytec T300 3K Carbon fiber bundles were used as the carbon fiber source. It has a known resistance of 1.7 x 10^{-3} Ω×cm, a weight density of 0.002gm/cm, and average fiber diameter of 5μm. The bundles were cut into 11cm strips and were coated with commercial galvanization zinc paint (93% pure zinc).

To conduct joule heating, the fibers with the zinc coat were placed between two electrodes and connected to a standard power-supply. The electrical contact region at each bundle's end was measured to be 0.05 cm to ensure good electrical contact. This left 10cm of the zinc-coated carbon fiber exposed to the atmosphere. The power-supply set to current control mode allowing the voltage to change accordingly to the resistance of the bundle. Since each bundle had a different amount of zinc coating, it was expected that each set would have a different minimum-heat transfer rate to ignite the zinc coat. To find this minimum-heating rate, different amperage rates were applied which could be correlated to temperature rates. The current would continue to rise until it reached a maximum of 1.7 amps.

The joule heating work was performed in a $2m^3$ fume hood under atmospheric conditions. The surface temperature, voltage, and current were actively recorded during the joule heating. The surface temperature of the samples was monitored with thermocouple and recorded LABview at a rate of 20recordings/sec. This temperature recording would allow the monitoring of the sudden changes during ignition and the maximum temperature generated by Zn powder combustion. The voltage and current were recorded by a digital multi-meter at a rate of 10 recordings/sec. With these two parameters, the power and resistance of the coated carbon fiber bundle could be calculated during joule heating. In addition, the power and resistance changes can be correlated with the heat transfer rate and the ignition temperature.

After each reaction, the electrical contact ends were removed, leaving just the reaction region. The weight of the reaction region of each coated fiber bundles was measured and compared with preheated weight. The zinc coat morphology changes on the surface and cross section were examined through SEM.

6.3.Results

ZnO nanostructures were successfully hybridized on carbon fiber through joule heating. The concentration of Zn particles on the carbon prior to joule heating played a role in the minimum heat transfer rate for combustion. Nanostructures associated with these transfer rates could also be distinguished. Finally, the cross-section analysis of the ZnO nanostructures can provide a means to understand the growth mechanism for the nanostructures.

For each joule heating experiment, a couple of events would occur. At 100^{o}C, the sizing began to burn and was seen as a wisp of smoke. Upon further heating, the coated carbon fiber would either not explode or explode. For the non-exploded samples, the heating rate was below a particular threshold, which would cause the coated carbon fiber to glow red but not cause the Zn powders to combust despite reaching 1.7 amps. However, if the rate was above the threshold, the coated carbon fiber would ignite and combust before reaching 1.7 amps. The faster the heating rate, the more probable the combustion. The combustion would continue until all of the zinc was consumed. The consumption period could be as little as microseconds once ignition occurs.

It was found that the additional zinc concentration required a lower minimum-heat transfer rate for Zn ignition. Figure 2 shows the heating rates performed on different concentrations of zinc powder on the carbon fiber. On the graph, the ignited samples are represented by diamonds and the non-ignited samples are represented by squares. Two trend-lines are shown to show the regions where the majority of the samples ignited or not. The region between these two trend-lines is considered metastable where the sample may or may not ignite.

These three regions corresponded well with Frank Kamenetskii's heat transfer and reaction rates[27], which can be seen in figure 6.3(a). If the heat transfer rate is above the reaction rate, the combustion of the zinc particles would occur. If the heat transfer rate is below the reaction rate, thermal oxidation of the zinc particles would occur. Finally if the heat transfer rate intersects the reaction rate, the reaction may or may not result in combustion. Based on the experimental results, the increased zinc concentration causes reaction rate to shift left. This means an increase in zinc concentration will require a lower heat transfer rate is cause zinc to combust. A visualization of this shift can be seen in figure 6.3(b).

Using the SEM, four distinct ZnO nanostructures were found on the combustion samples: tetrapods, nanosheets, nanowires, and hollow sea-urchins. The occurrence of these nanostructures could be correlated to the heating rate. The location of the nanostructures in the ZnO coat provides clues to the growth mechanism. On samples that did not combust, only oxidized Zn particles were found. Figure 6.4 shows images of all of observed distinct nanostructures. Table 6.1 shows the observed nanostructures and their placement in the thicknesses relative to the carbon fiber.

For combusted samples that were heated above the minimum threshold heat transfer rate, all four nanostructures were found. Figure 6.5 shows a cross section image of the ZnO coat and the respective positions these nanostructures through higher magnification images. Furthest away from the carbon fiber bundle, tetrapods were found. Directly beneath the tetrapods, ZnO nanosheets were formed. Below the sheets, nanowires could be found. Finally, between the nanowires and the carbon fiber bundles, hollowed sea urchins were found. The nanowires found in these samples have lengths between 500nm-5µm. The diameters were found to be less than 100nm.

For the combusted sample that was heated in the metastable region, nanowires and hollow sea-urchins were found. Figures 6.6 shows a cross section of the ZnO layer with higher magnification images showing the distinction between the nanowires and hollow sea-urchins. In some cases, uniform ZnO nanowire arrays were found on the carbon fiber. The nanowires found in the metastable samples have longer lengths > 5µm and diameters greater than 500 nm.

6.4. Discussion

To explain the growth mechanism behind these observe nanostructures, correlations can be made to work performed in chemical vapor deposition and thermal oxidation synthesis. The first three nanostructures are products of vapor deposition, whereas hollowed sea urchins are products of diffusion. Between CVD and Thermal oxidation models, the main variant between the two models is the oxygen availability. According to CVD growth different nanostructures could be repeatedly grown under the particular temperature regions and O_2 flow. Thermal oxidation begins with existing Zn structures at lower temperature and then exposes them oxygen, forming oxide structures. With the growth mechanism, the threshold heat transfer rate can be explained and why it is influenced by additional zinc concentration.

6.4.1. ZnO Tetrapod Growth

Tetrapods are a product of vapor deposition, which require a high temperature and high concentrations (>20%) of oxygen. The tetrapod is an independent ZnO nanostructures that have four legs and connected by a core. According to literature, this core is ZnO with zinc-blend structure. The legs are composed are ZnO in the wurtzite structure. Due to ZnO's anisotropic nature, the legs grow in the [0002] direction.

A ZnO tetrapod is a unique structure, which has a zinc-blende (ZB) core and wurtzite (WZ) legs. The ZB phase, is a metastable phase of ZnO, which it requires higher temperature and pressure than WZ growth. The WZ phase is the lowest energy phase of ZnO and more easily produced. For tetrapods to form, Zn vapor react (in a high temperature region) with oxygen to form a ZB core. As core travels into a lower temperature region with less oxygen, WZ legs begin to form. In CVD growth, the initial growth of a ZnO tetrapod will initiate by homogenously nucleation forming a Zinc-blende core structure. As the ZnO core travels down the tube furnace, two conditions changes: the temperature becomes cooler near the end of the furnace and oxygen concentration flow decreases because it getting consume by Zn vapors up stream. This it becomes more thermodynamically stable for continual ZnO growth to occur heterogeneously in the wurtzite form on the ZB ZnO cores. In the case with the hybridization of ZnO nanostructures on carbon fiber, tetrapods are located on the outer perimeter of the ZnO layer because it had the highest exposure to oxygen.

For this work, Zn vapors are produced through the joule heating of the carbon fiber and are then exposed to high temperature (>1600^{o}C) ZnO through the exothermic reaction. The Zn vapors will quickly react with the atmospheric oxygen and begin to form a ZB core. As the vapors move further away from the carbon fiber and surround oxygen is consumed, WZ legs begin to form on the ZB cores. Figure 6.7 shows a schematic of how ZnO tetrapod are formed from the zinc particle precursor.

6.4.2. ZnO Nanosheet Growth

ZnO sheets are particular are also formed through vapor deposition. Typical ZnO sheet growth is developed through medium concentrations (5%) of oxygen. Seen in many CVD experiments, initial growth of sheets begins as an array of ZnO nanowires (also known as combs). After these comb structures are formed, the space between the nanowires are filled with ZnO. Figure 6.8 show schematic of the sheet growth along with SEM images of the sheets grown through this work. The image shows clear nanowires arrays and sheet growth between the array. The sheet also shows a meniscus shape, which is representative of capillary growth which uses the nanowire array as heterogenous nucleation sites.

6.4.3. ZnO Nanowire Growth

ZnO nanowires are formed through vapor deposition and through diffusion. For deposition, nanowires formed under lower temperature synthesis and minimum O_2 concentrations, sometimes one fourth the requirement to produce tetrapods. The growth orientation of this nanowires is in the [0002] direction, which is the same for the legs of the tetrapods. Nanowires were found in the samples that were heated in the combusted regions and in the metastable regions. Figure 6.9 shows a schematic diagram of how ZnO nanowires can form through deposition or through diffusion. In deposition growth, vapors begin to form heterogenous ZnO structures in the [0002] direction. The anisotropic growth continues as the ZnO vapors deposit on the tip of the nanowire to help lower the surface energy of the (0001) plane. Diffusion growth occurs through metallic zinc diffusing through the ZnO. Zn has a higher diffusivity in ZnO than oxygen. Thus the growth direction is towards the oxygen rich environment. Zn diffusion towards the surface can be accelerated if there are grain boundaries, which provide a lower energy pathway.

6.4.4. Hollow ZnO Sea Urchins Growth

ZnO hollow sea urchins structures can be identified as spherical structures that have hollowed shell structures with nanowires protruding from the surface. Reports have shown hollow sea urchins are initially grown through a thermal oxidation process. The initial growth begins with a Zn particle exposed to oxygen, instantaneously creating an oxide layer. This oxide layer hinders further oxidation of metallic zinc. For the metallic zinc to reach the oxygen rich environment, diffusion through the ZnO crystal, diffusion through the ZnO grain boundaries, or evaporation through a crack in layer must occur. Both of these mechanisms can help cause a hollow structure to form. Through diffusion, hollowed structures are formed through the Kirkendall effect where Zn diffusion through ZnO is faster than oxygen diffusion in ZnO.

After the shell is formed, anisotropic nanowires are formed. The exact mechanism for the transition between a shell formation and the nanowire growth is not well established. Different groups have suggested various mechanisms: diffusion growth, stressed induced diffusion growth, and vapor deposition growth. In all of these reports, ZnO hollow sea urchin nanostructures are formed under elevated temperatures. Figure 6.10 shows a schematic of how these sea-urchin nanostructures form correlating to structures observed in the SEM images.

6.4.5. ZnO Nanowire Arrays on Carbon Fiber Growth

Upon further investigation, there was one more unique ZnO nanostructure observed, a uniform array of ZnO nanowires in direct contact with individual carbon fiber. These heterogenous structures were found beneath all of the nanostructures, directly on the carbon fiber bundle. It appears that the these covered carbon fibers were isolated from the carbon fiber bundle allowing them to be surrounded by zinc particles to allow for the wetting of zinc upon melting and then uniform explosive oxidation to create a uniform array of ZnO nanowires. Figure 6.11(a) shows a carbon fiber with a uniform array of zinc oxide nanowires. A zoomed in picture, figure 6.11(b), shows that the nanowires are 1-5µm in length and 100nm in diameter. From the different sections of the carbon fiber array, the density of these nanowires was found to be to be 10/µm2 as seen in figure 6.11c. In some cases, there are small cluster of ZnO nanowires attached to the ZnO shown in figure 6.11d, we can see that these ZnO appears to be connected to the carbon fiber.

From the layering of these nanostructures, it can be deduce the order in which these nanostructures were produced. Thus, the proposed mechanism for the ignited ZnO structures is a function of available oxygen. Initially, when ignition occurs, there is plenty of oxygen (20%) for tetrapod formation. Vapor Zn will react with oxygen and homogenously nucleate with a zinc blende structure. As it moves away from the system, the temperature decreases it becomes more preferential for wurtzite legs to form.

As the local O_2 is being consumed, the Zn beneath the outer layer will have less oxygen for reaction. Thus, there will not be enough O_2 for further ZnO tetrapod formation. Instead ZnO nanosheets and nanowires are formed. More evidence of oxygen depletion through consumption is evident by the hollow sea urchins beneath the nanowires. This is a slower method of growth since it is diffusion limited. Initially, there is only a small portion of O_2 available which is allowed to create a thin oxide layer. As the O_2 recovers due to the void left by the outer ZnO formation, the metallic zinc beneath the ZnO shells will begin to form into nanowires and create a sea urchin nanostructure. Similar to the hollowed sea urchin structures, ZnO coated carbon fiber bundle, uniform ZnO nanowire arrays that covered individual carbon fibers. The uniformity of the ZnO nanowire array provides evidence of Zn melting and wetting over the carbon fiber before explosion. The wetting of the zinc prior to explosion could explain the drop in resistivity of the zinc coated carbon fiber bundle as the heating rate increase. However, as combustion occurred, the resistivity increased because there was no more Zn contribution. For future systems, if uniform ZnO nanowire arrays over carbon fiber or other conductive advanced textiles are desired, wetting of the precursor of the fiber is crucial.

The presence of specific nanostructures provided many clues to the growth mechanisms behind the ZnO nanostructures through the joule heating of carbon fiber. These growth mechanisms can be used to help explain why the additional zinc concentration requires a lower threshold heat transfer rate for zinc combustion. Initially, this was not well understood. However, by understanding that some of the nanostructures grown near the metastable heat transfer rate were influenced by thermal oxidation, it can be proposed that at low concentrations, there is a more surface area/concentration exposed to the atmosphere. This exposure creates many oxide layers that prevent metallic zinc from vaporizing. For samples that have additional zinc concentration, many particles are not in beneath the outer layer are protected from the atmosphere and can heat and vaporized before being oxidized. Thus, lower heat transfer rate is required for Zn combustion. For samples with less zinc concentration, a higher heating rate is required to vaporize the zinc before an oxide barrier is created. These findings correlate well to Frank Kamenetskii's work on heat transfer rate, which describes that heat transfer rates above a reaction rate, combustion occurs. In this work, that reaction rate is correlated to the diffusion thermal oxidation rate. Above this rate, the vapors are produce and a reaction occurs in the vapor phase. This reaction is highly exothermic and defined as combustion.

6.5. Conclusion

By identifying the ZnO nanostructures and their location on the hybridized carbon fiber, their growth mechanism could be proposed based on the understanding of the same nanostructures found CVD and thermal oxidation growths. These growth mechanisms were used to help explain the additional zinc's concentration influence on the threshold heat transfer rate. It was found that at higher rates or additional zinc concentrations allow zinc vapor to form before being consumed by thermal oxidation. In this work, it was found that heat transfer rates and precursor concentrations influence the nanostructures produced on hybridize carbon fibers. These nanostructures will influence the overall functional properties for multifunctional composites.

6.6.Figures

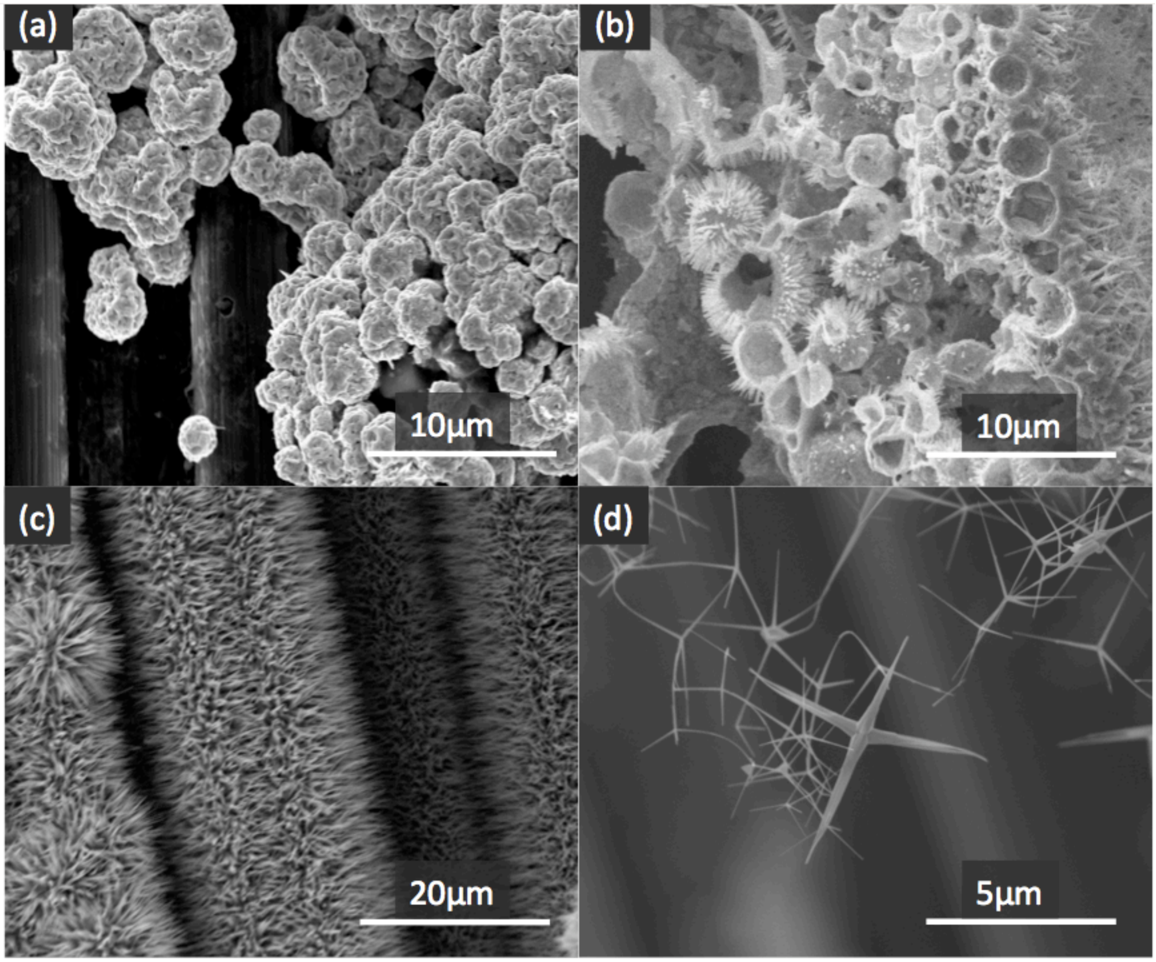

Figure 6. 1: Shows different ZnO nanostructures commonly found in ZnO hybridization process: (a) Oxidized ZnO particles (no combustion); (b) Hollow sea-urchins ZnO; (c)ZnO nanowire arrays on carbon fiber; (d) ZnO tetrapods.

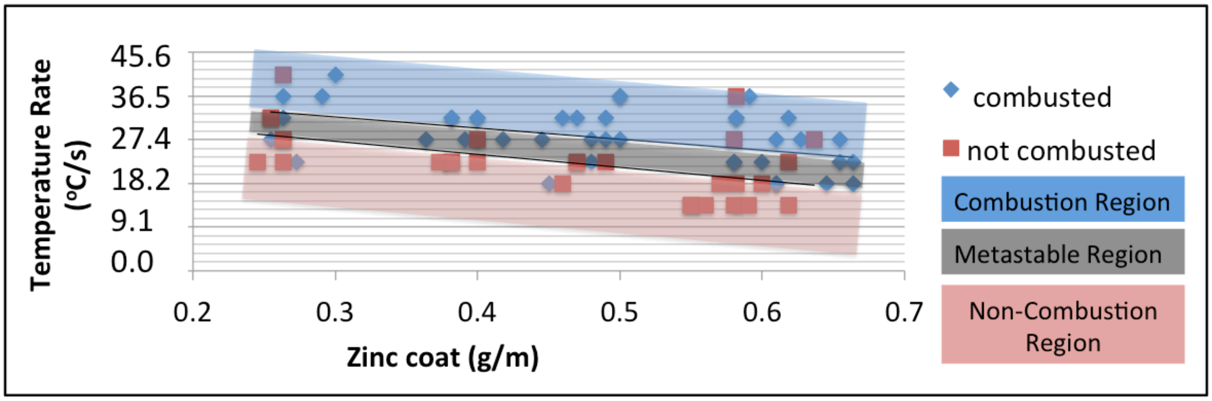

Figure 6. 2: This figure shows that combustion through heat transfer is dependent on the zinc coat density. At low coating densities it requires a faster heating rate. There are more surface areas exposed for thermal oxidation. As the zinc coat density is decrease, there is surface to volume ratio decreases allowing the Zn to vaporize before being trapped by an oxide layer barrier.

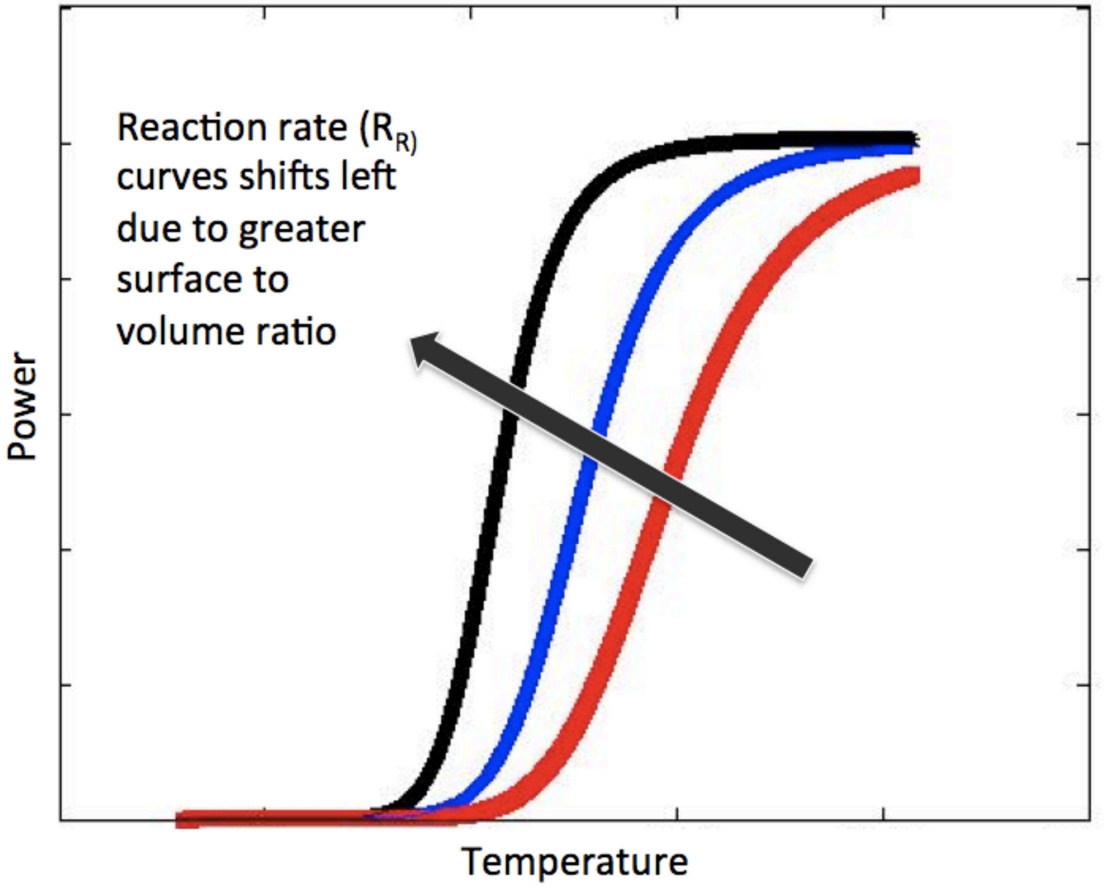

Figure 6. 3: A qualitative observation showed a left-shift in the Reaction Rate curve when fewer Zn precursors are applied on the carbon fiber. The few Zn particles offer more surface area for the oxidation reaction to occur which requires a faster heating rate to vaporize the zinc particles before oxidation occurs. Once oxidation occurs, the oxide layer serves as a barrier to prevent combustion.

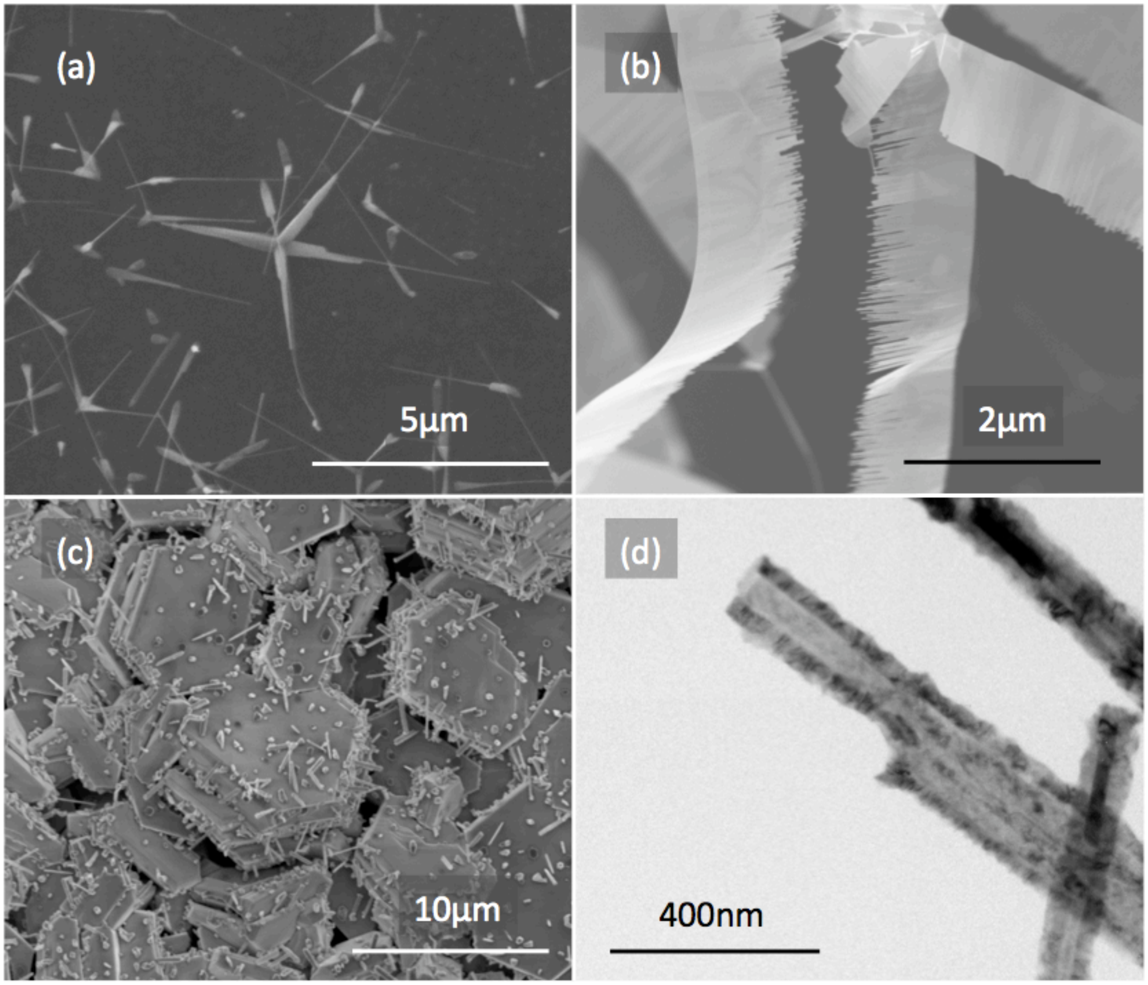

Figure 6. 4: Various ZnO nanostructures from CVD and thermal oxidation show similar features from Zn combustion. (a) and (b) show a multipod and a sheet respectively. Both nanostructures were grown in CVD. (c) and (d) show Zn plates with ZnO nanowires and hollow ZnO tubes respectively. These ZnO nanostructures were grown through thermal oxidation. ZnO nanostructures grown through these methods can be used to help provide a mechanistic understanding of ZnO developed through Zn combustion.

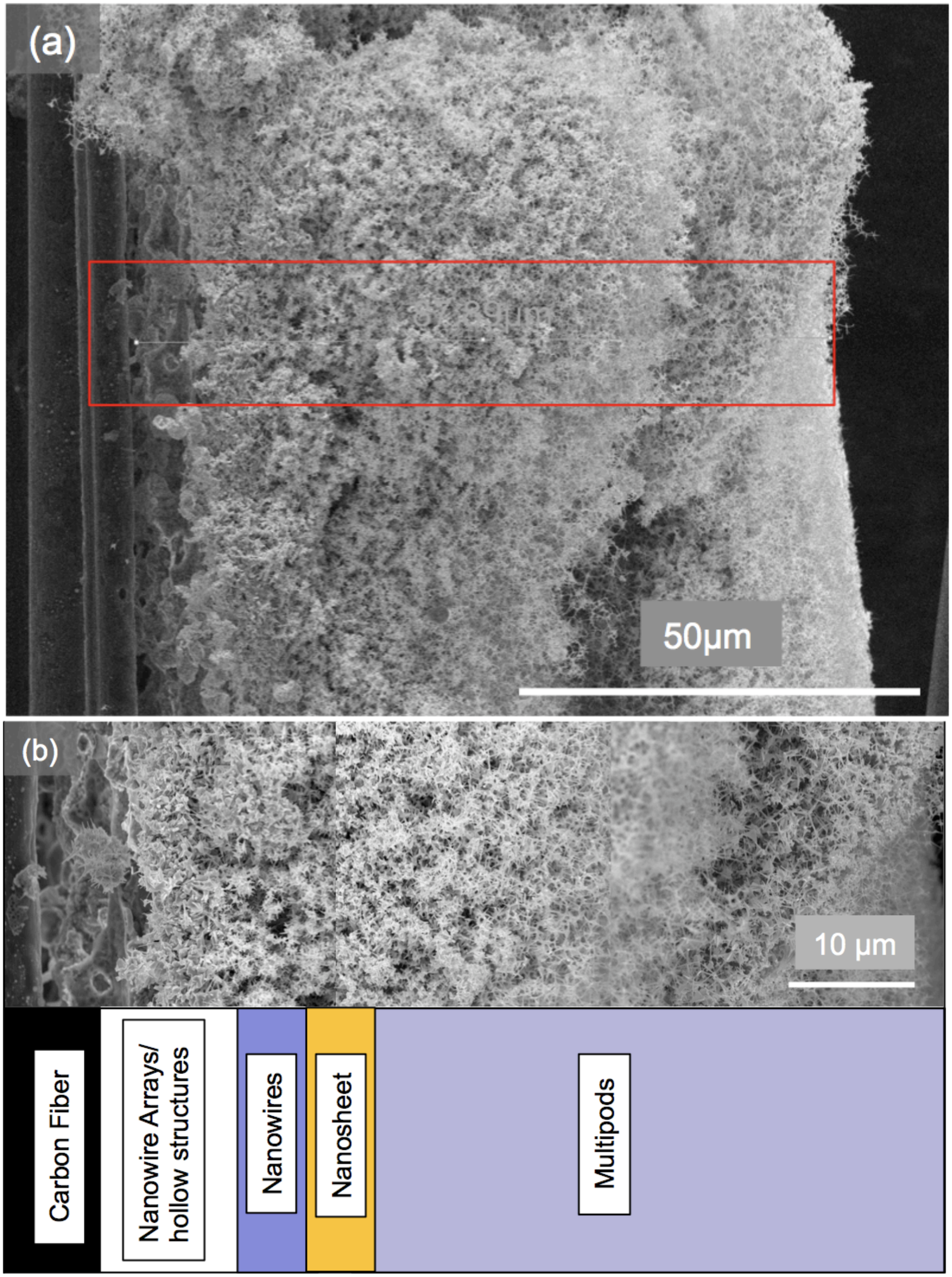

Figure 6. 5: (a) The cross section of a sample heated in the combusted region is shown. (b) A magnified version of the highlighted area is shown with the ZnO nanostructures identified. These nanostructures include Multipods (including tetrapos), nanosheets, nanowires, nanowire arrays, and hollow structures.

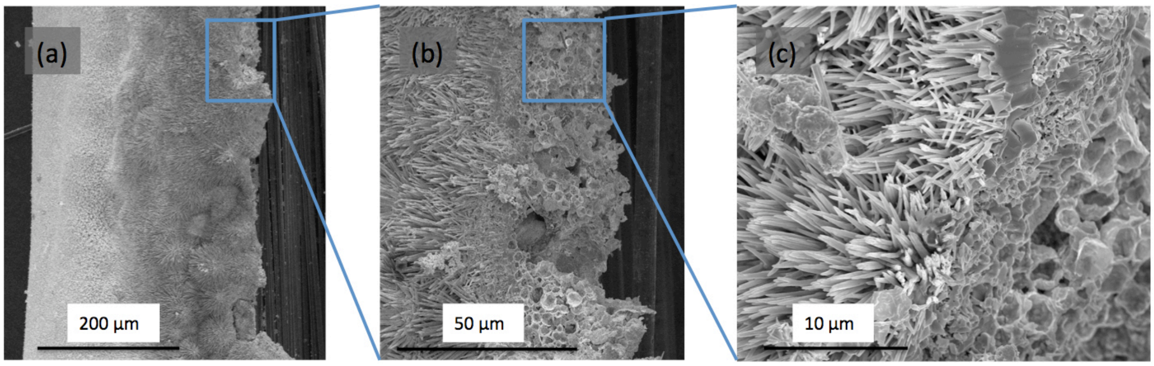

Figure 6. 6: (a) A cross section of a combusted sample that was heated at a metastable heating rate. Magnified images (b) and (c) show thick nanowires and hollowed structures.

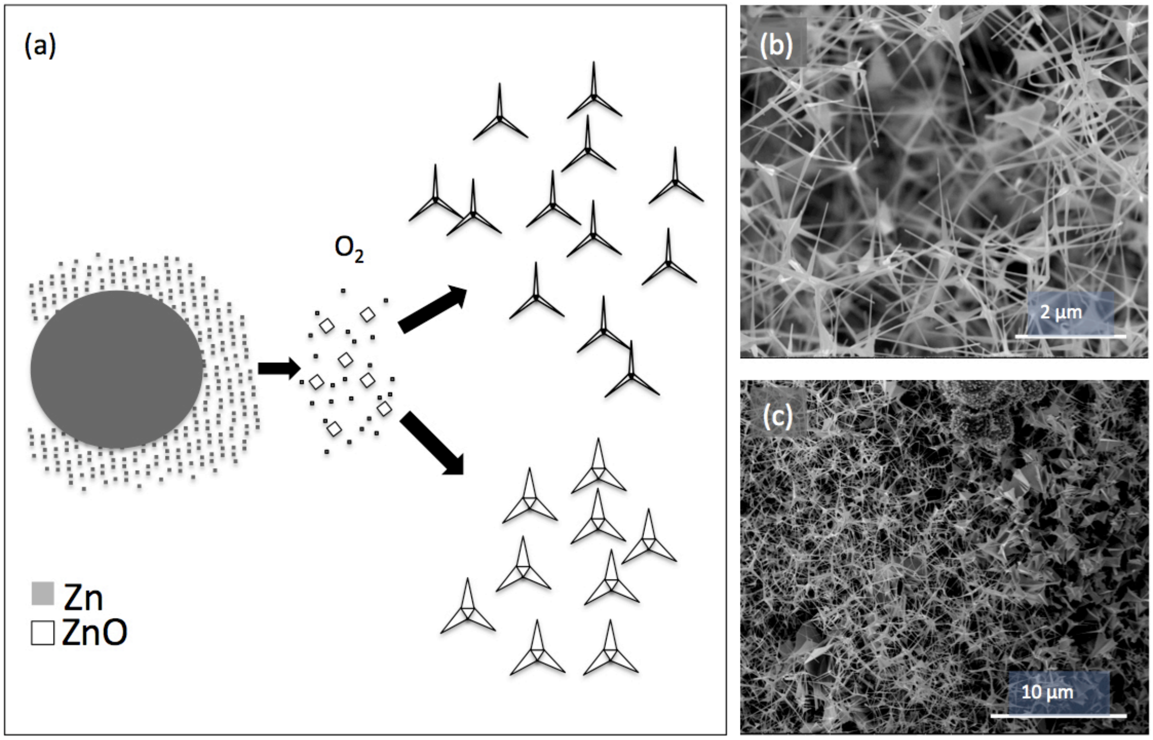

Figure 6. 7: A schematic of tetrapods grown through vapor deposition is shown. Core nuclei are formed homogenously. As the cores are carried into lower temperature regions, legs begin to grow on the cores. SEM images show the variation in size of different tetrapods.

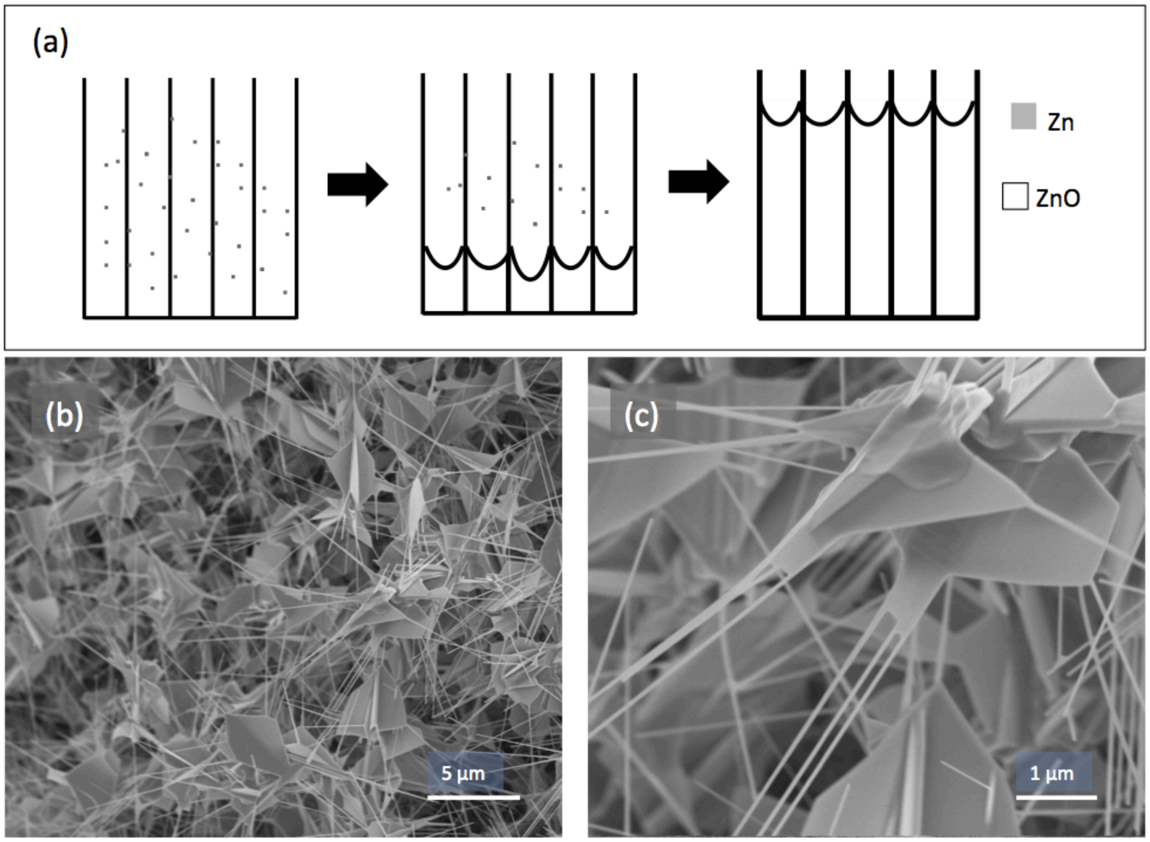

Figure 6. 8: A schematic of ZnO nanosheets growth is shown. As ZnO nanowires arrays are created, zinc vapors and oxygen begin to deposit between the sheets. In figure (b), an SEM image shows a large quantity of nanosheet growth. A magnified image is shown figure (c), where the sheet is growing between the nanowire arrays.

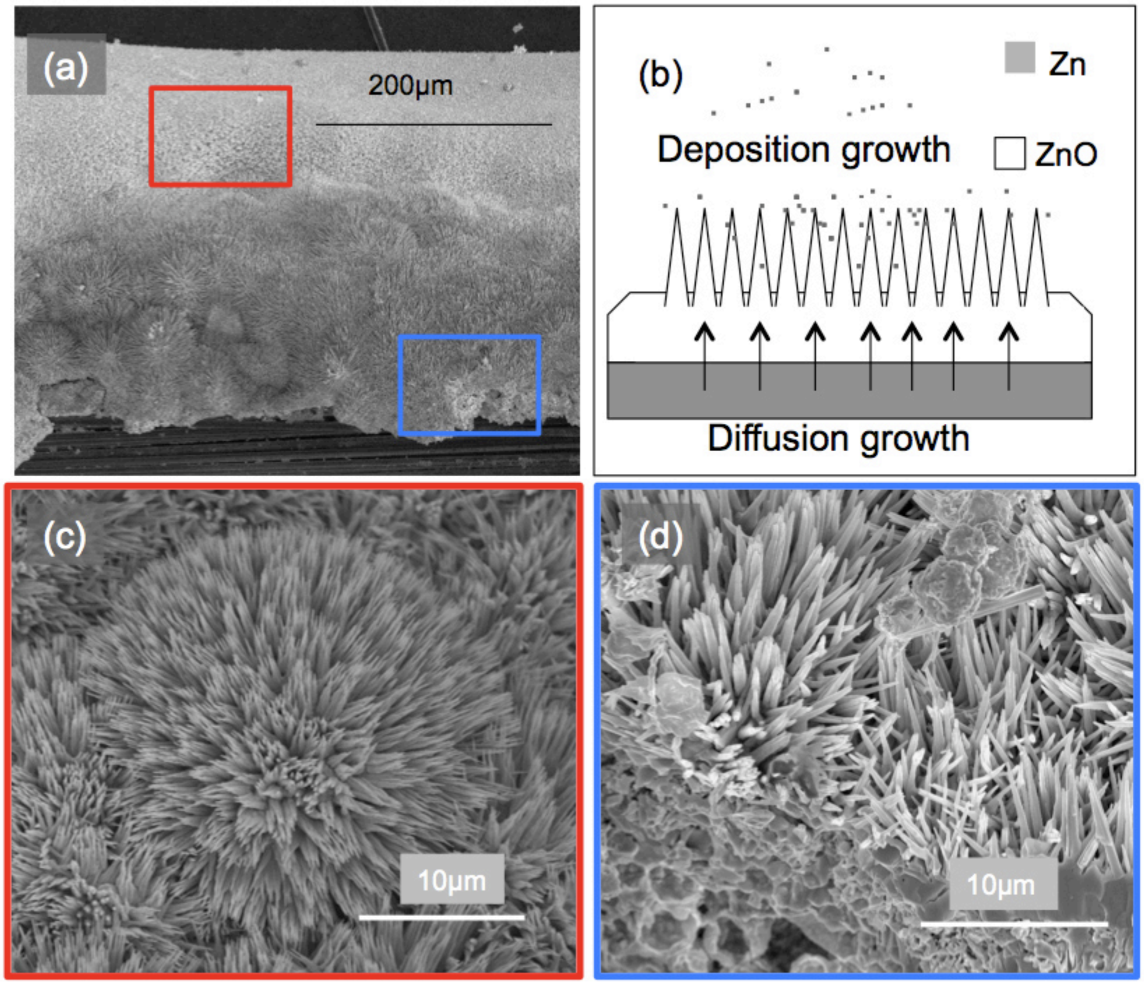

Figure 6. 9: (a) An SEM image shows the cross section of a sample heated by metastable heating rate. (b) A schematic dhows how ZnO nanowires can grow through deposition or diffusion mechanism. (c) A magnified image shows ZnO nanowire clusters on the surface of the ZnO coat. Zn vapors that are generated redeposit on the ZnO.

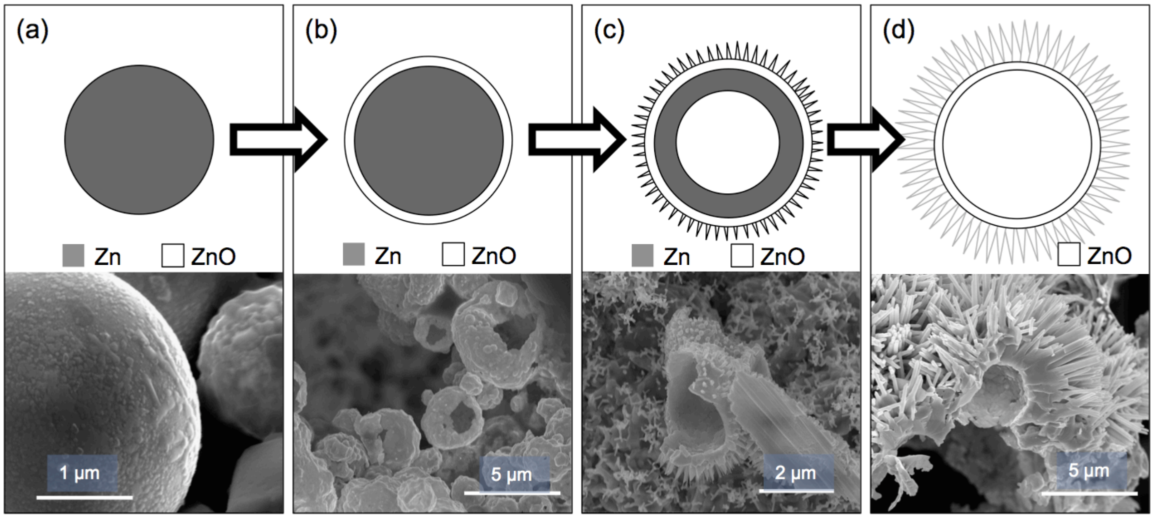

Figure 6. 10: The figure shows observed Zn and ZnO structures and a schematic of the progression of Zn particle evolution to become ZnO hollow sea urchins.

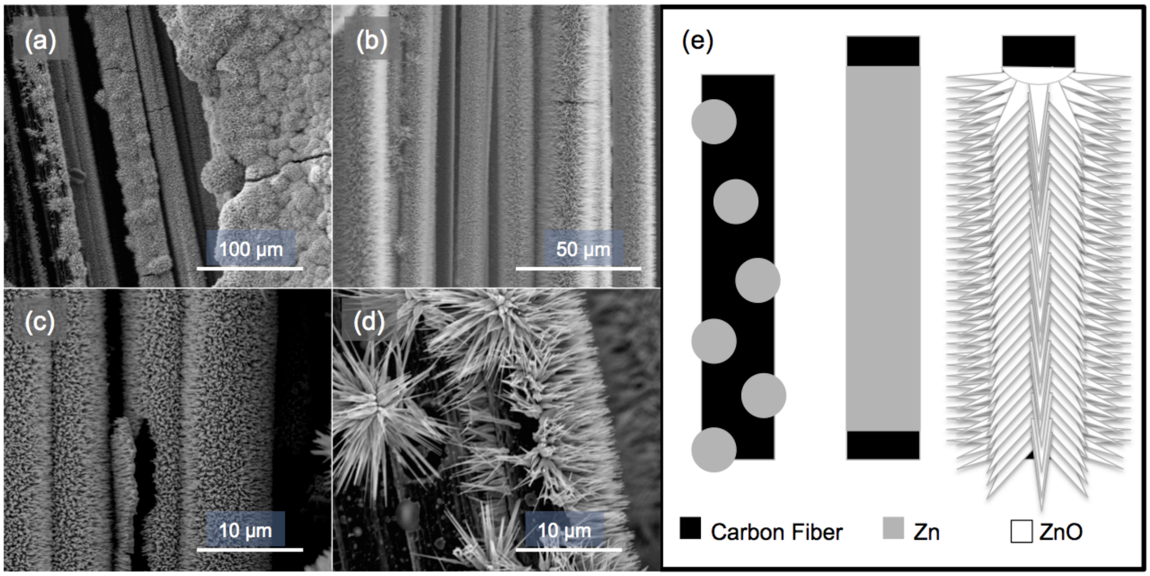

Figure 6. 11: Different images of uniform ZnO nanowire arrays show the variation nanowires grown on carbon fiber. A schematic of the ZnO nanowires is shown where the Zn particles wet the surface of the carbon fiber, which leads to the uniform array of ZnO nanowires on the carbon fiber.

6.7 References

1. Unalan, H. E.; Wei, D.; Suzuki, K.; Dalal, S.; Hiralal, P.; Matsumoto, H.; Imaizumi, S.; Minagawa, M.; Tanioka, A.; Flewitt, A. J., Photoelectrochemical cell using dye sensitized zinc oxide nanowires grown on carbon fibers. *Applied Physics Letters* **2008,** *93* (13), 133116.

2. Alipour Skandani, A.; Masghouni, N.; Case, S.; Leo, D.; Al-Haik, M., Enhanced vibration damping of carbon fibers-ZnO nanorods hybrid composites. *Applied Physics Letters* **2012,** *101* (7), 073111-073111-4.

3. Eckhoff, R., *Dust explosions in the process industries: identification, assessment and control of dust hazards*. Gulf professional publishing: 2003.

4. Gupta, A.; Harrison, I., New aspects in the oxidative stabilization of PAN-based carbon fibers. *Carbon* **1996,** *34* (11), 1427-1445.

5. Chand, S., Review carbon fibers for composites. *Journal of Materials Science* **2000,** *35* (6), 1303-1313.

6. Özgür, Ü.; Alivov, Y. I.; Liu, C.; Teke, A.; Reshchikov, M.; Doğan, S.; Avrutin, V.; Cho, S.-J.; Morkoc, H., A comprehensive review of ZnO materials and devices. *Journal of applied physics* **2005,** *98* (4), 041301.

7. Wang, Z. L.; Kong, X. Y.; Ding, Y.; Gao, P.; Hughes, W. L.; Yang, R.; Zhang, Y., Semiconducting and piezoelectric oxide nanostructures induced by polar surfaces. *Advanced Functional Materials* **2004,** *14* (10), 943-956.

8. Yang, J. L.; An, S. J.; Park, W. I.; Yi, G. C.; Choi, W., Photocatalysis using ZnO thin films and nanoneedles grown by metal–organic chemical vapor deposition. *Advanced materials* **2004,** *16* (18), 1661-1664.

9. Brown, M. E., ZnO-Rediscovered. **1957**.

10. Jaffe, J.; Hess, A., Hartree-Fock study of phase changes in ZnO at high pressure. *Physical Review B* **1993,** *48* (11), 7903.

11. Zanotti, L.; Calestani, D.; Villani, M.; Zha, M.; Zappettini, A.; Paorici, C., Vapour‐phase growth, purification and large‐area deposition of ZnO tetrapod nanostructures. *Crystal Research and Technology* **2010,** *45* (6), 667-671.

12. Leung, Y.; Djurišić, A.; Gao, J.; Xie, M.; Wei, Z.; Xu, S.; Chan, W., Zinc oxide ribbon and comb structures: synthesis and optical properties. *Chemical physics letters* **2004,** *394* (4), 452-457.

13. Park, J.-H.; Choi, H.-J.; Choi, Y.-J.; Sohn, S.-H.; Park, J.-G., Ultrawide ZnO nanosheets. *Journal of Materials Chemistry* **2004,** *14* (1), 35-36.

14. Banerjee, D.; Lao, J. Y.; Wang, D. Z.; Huang, J. Y.; Ren, Z. F.; Steeves, D.; Kimball, B.; Sennett, M., Large-quantity free-standing ZnO nanowires. *Applied Physics Letters* **2003,** *83* (10), 2061.

15. Shen, G.; Bando, Y.; Lee, C.-J., Synthesis and Evolution of Novel Hollow ZnO Urchins by a Simple Thermal Evaporation Process. *The Journal of Physical Chemistry B* **2005,** *109* (21), 10578-10583.

16. Fan, Z.; Lu, J. G., Zinc oxide nanostructures: synthesis and properties. *Journal of nanoscience and nanotechnology* **2005,** *5* (10), 1561-1573.

17. Zha, M.; Calestani, D.; Zappettini, A.; Mosca, R.; Mazzera, M.; Lazzarini, L.; Zanotti, L., Large-area self-catalysed and selective growth of ZnO nanowires. *Nanotechnology* **2008,** *19* (32), 325603.

18. Tani, T.; Mädler, L.; Pratsinis, S., Homogeneous ZnO Nanoparticles by Flame Spray Pyrolysis. *Journal of Nanoparticle Research* **2002,** *4* (4), 337-343.

19. Baruah, S.; Dutta, J., Hydrothermal growth of ZnO nanostructures. *Science and Technology of Advanced Materials* **2009,** *10* (1), 013001.

20. Khanlary, M. R.; Vahedi, V.; Reyhani, A., Synthesis and characterization of ZnO nanowires by thermal oxidation of Zn thin films at various temperatures. *Molecules* **2012,** *17* (5), 5021-9.

21. Liu, B.; Zeng, H. C., Direct growth of enclosed ZnO nanotubes. *Nano Research* **2009,** *2* (3), 201-209.

22. Gu, Z.; Paranthaman, M. P.; Xu, J.; Pan, Z. W., Aligned ZnO nanorod arrays grown directly on zinc foils and zinc spheres by a low-temperature oxidization method. *ACS nano* **2009,** *3* (2), 273-278.

23. <2005. shen. Synthesis and Evolution of Novel Hollow ZnO Urchins by a Simple Thermal Evaporation Process.pdf>.

24. Chang, P.-C.; Fan, Z.; Wang, D.; Tseng, W.-Y.; Chiou, W.-A.; Hong, J.; Lu, J. G., ZnO nanowires synthesized by vapor trapping CVD method. *Chemistry of materials* **2004,** *16* (24), 5133-5137.

25. Pan, Z. W.; Dai, Z. R.; Wang, Z. L., Nanobelts of semiconducting oxides. *Science* **2001,** *291* (5510), 1947-9.

26. Ding, Y.; Lin Wang, Z.; Sun, T.; Qiu, J., Zinc-blende ZnO and its role in nucleating wurtzite tetrapods and twinned nanowires. *Applied physics letters* **2007,** *90* (15), 153510-153510-3.

27. Frank-Kamenetskii, D. A. b. *Diffusion and heat exchange in chemical kinetics*; University press: 1955.

Chapter 7 Future Work and Conclusion

7.1. Summary

The culmination of this work focused on understanding the growth mechanism of ZnO nanostructures to apply them on carbon fiber for multifunctional composites. The growth mechanisms of ZnO nanostructures were understood through thermal oxidation (diffusion) and chemical vapor deposition systems were investigated. Both of these systems provided clear understanding of ZnO nanostructure growth. Unfortunately both of the systems are not practical for applying ZnO nanostructures on carbon fiber because they produce ZnO nanostructures at low yields. This low yield derives from the required vacuum systems and high temperature furnaces, which require additional processing time for pumping, heating, and cooling. Instead, a new method was created and investigated to enable a low cost-robust method to hybridize ZnO nanostructures on carbon fiber. This method uses Self-propagating High-temperature (combustion) Synthesis to ignite and combust metallic zinc powders. Through various characterization techniques, it was found that many of the nanostructures through the SHS process were similar to those seen in thermal oxidation and CVD processing. Thus, the growth mechanisms of the nanostructures through the SHS process were proposed.

7.2. Developing a Multifunctional Composite

With hybridized ZnO coated carbon fiber, multifunctional composites can be created. Four different carbon fiber layup designs were created shown in Figure 7.1. Traditional carbon fiber wet layup procedures were followed. The matrix material, EPON 862, was mixed with a curing agent, Epikure W, in a 100:26 ratio. Degassing was followed after mixing. The epoxy mixture was applied on each sheet of carbon fiber. The resin soaked carbon fiber sheets were they laid in the appropriate stacking sequence. The bagging procedures included a mold (aluminum coated with a nonstick coat), the carbon fiber sheets, Teflon release film, a bleeder, and a nonporous bagging material. The bagging unit was placed under 29 inches Hg of vacuum, sufficient for pulling out excess resin and further degasing the composite structure. The vacuumed bagging unit was then placed in an oven at 180°C for 5 hours.

To test for piezoelectric properties, the composites were placed under two conducting plating plates (aluminum foil) and wired to an oscilloscope. The samples are then placed with on two cylindrical points at the ends and tap in the middle, like a 3-point bend test. An illustration of this set up is shown in figure 7.2. Amongst the four samples, voltage responses were seen in 1ZNO-2C-1ZnO, 1C-2-1C, and 4ZnO layup sequence. No response was seen in the 4C layup sequence. The highest observed voltage response was .1V, which is two orders of magnitude higher than noise produce by surface contact. In these preliminary tests, it has been observed that the piezoelectric functionality has been successfully added to carbon fiber through the added ZnO nanostructures.

7.3. Applications

The Preliminary results open up a new avenue for work for high impact applications. The piezoelectric response will open up a new avenue for sensing and damping harvesting applications for carbon fiber reinforced composites[1]. Other reports have use ZnO in photovoltaic energy harvesting applications[2]. In the case large commercial avionics, there is a lot of real estate on aircraft wings, which can take advantage of these multifunctional composites.

Piezoelectric composites can be used for active sensing especially at the front edges of aircraft wings to monitor sites of impact with birds or other debris during flight. This monitoring system can be used as active non-destructive testing, which can assess possible structural damage such as delamination or cracking. This can increase the amount of time the aircraft is in the air because current composite aircrafts are required NDT assessment after each flight. Current NDT methods required the aircraft to be grounded. An active monitoring system can provide assessment in the air and pinpoint locations where possible damage occurred on impact for specific location NDT assessment. Such assessments can help prolong predetermined aircraft lifetimes.

Piezoelectric composites can also be used in structural dampening applications. Currently, lead-zirconium titanate (PZT) fibers are used in sports equipment such as tennis rackets, skis, and snowboards. As the users routinely experience impacts in the respective sports, joint and muscle fatigue are more probable. With active dampening, the piezoelectric composites help stiffen the equipment through an indirect response where an external voltage is applied to prompt a mechanical response. Similar responses can be useful to help stabilize aircraft wings. Carbon fiber hybridized with ZnO nanostructures may find application in these applications because successful carbon fiber composites have been shown with piezoelectric responses.

Though it is out of the scope of this work, carbon fiber hybridized with ZnO nanostructures can be used for energy harvesting. Reports have shown ZnO nanostructures hybridized on carbon fiber (through separate CVD and hydrothermal processing work) were dye-synthesized to produce photovoltaic devices. With the given real estate on aircraft wings, multifunctional composites exhibiting photovoltaic energy harvesting may help prolong flights. Currently UAV use silicon based solar cells to help prolong flight.

The work on multifunctional composites is far from complete. By no means are the produced composite coupons ready to be tested in modern aircraft such as the Boeing 787. A complete analysis of multifunctional composites produced by the SHS method is out of the scope of this thesis. However, this work has opened up a new avenue of research, which should provide a feasible opportunity to develop multifunctional composites through our ZnO nanostructures hybridized on carbon fiber. Areas of work that can be pursued include quantifying the piezoelectric response. These avenues include the measuring the piezoelectric response in relation to the ZnO quantity, quality, and layup sequence.

ZnO quantity can be simply be quantified as the amount of ZnO is hybridized on the carbon fiber. The previous chapter discussed the effect of Zn precursor on the heat transfer rate for combustion. However, it was not yet investigated on the effect it would have on the piezoelectric response.

ZnO quality can be related to ZnO nanostructures produced in the combustion process. It was shown in the previous chapters that different ZnO nanostructures could be related to different heat transfer rates. At heat transfer rates in the combustion region, many ZnO nanostructures such as tetrapods, sheets, nanowires, and hollow sea-urchins were found. For samples found in the metastable region, ZnO nanowires and hollow sea-urchins were found. The respective structure and sizes of these structures still needs further investigation at the microscopic and macroscopic level.

The layup sequence may also affect the piezoelectric response. In preliminary composite manufacturing results, no distinction was made between the layup sequence 1C-2-1C and 1-2C-1. However, further investigation of the layup sequence is required when ZnO quantity and quality is considered.

Another avenue of research needs investigation is the mechanical durability of these carbon fiber composite hybridized with ZnO nanostructures. To synthesize the ZnO nanostructures, a zinc powder combustion process is used. The process requires carbon fibers to be joule heated to temperatures that exceed 750oC. The combustion temperature of the zinc powder reaches a measured temperature of 1700oC. The possible damage to the carbon fiber through this process can compromise the structural integrity of the carbon fiber. To understand the damage on the carbon fiber, tensile testing at the individual fiber and composite level should be investigated. Tensile testing can provide can help determine the damage assessment on the carbon fiber. The results can also be combined with microscopic observations. The fracture features can help assist the type of failure mechanism.

Another area of structural integrity that must also be considered is the fatigue strength of the multifunctional composites. Fiber reinforced composites are highly pursued for their superior fatigued strength compared to their metal counterparts. However, if the fibers are weakened by the combustion process, these multifunctional composite may not be pursued for the compromised mechanical behavior.

Thus it is important developing ways to hybridize ZnO nanostructures on carbon fiber while considering fiber preservation. A couple possible routes can be pursued, though they do not guarantee the effectiveness of fiber preservation. The first route can include using appropriate amounts of precursor. It was found that under additional zinc precursor helped lower the joule-heating rate for the carbon fiber for zinc combustion. This lower temperature synthesis can help preserve the fiber's structural integrity. Another possible route can include a high temperature coating on carbon fiber to help minimize the oxygen contact at high temperatures. Oxidation of carbon fiber is well known and can destroy fibers at low as 400°C under prolonged exposure[3].

7.4. Conclusion

These are just some of the new avenues that work can be pursued towards the development of multifunctional composites using carbon fiber hybridized with ZnO nanostructures. This work was designed to find an affordable means to develop a multifunctional composite by integrating different disciplines of materials science and engineering through both literature and experimental understanding. Crystal growth through thermodynamic and kinetic understanding has provided means to understand the growth mechanism of ZnO nanostructures. Electrical properties have provided insight on the unique properties of ZnO: semiconducting, photochemical excitation, and piezoelectricity. Carbon fiber reinforced composites (known for their high strength, high modulus, and low density) have provided a substrate medium for ZnO nanostructures. By taking advantage of carbon fiber's resistive heating, Zn powders can be ignited into ZnO nanostructures. The hybridized fibers can then be integrated in a composite and used for future applications that require multiple properties: high strength, low weight, energy harvesting, damping, and sensing.

7.5 Figures

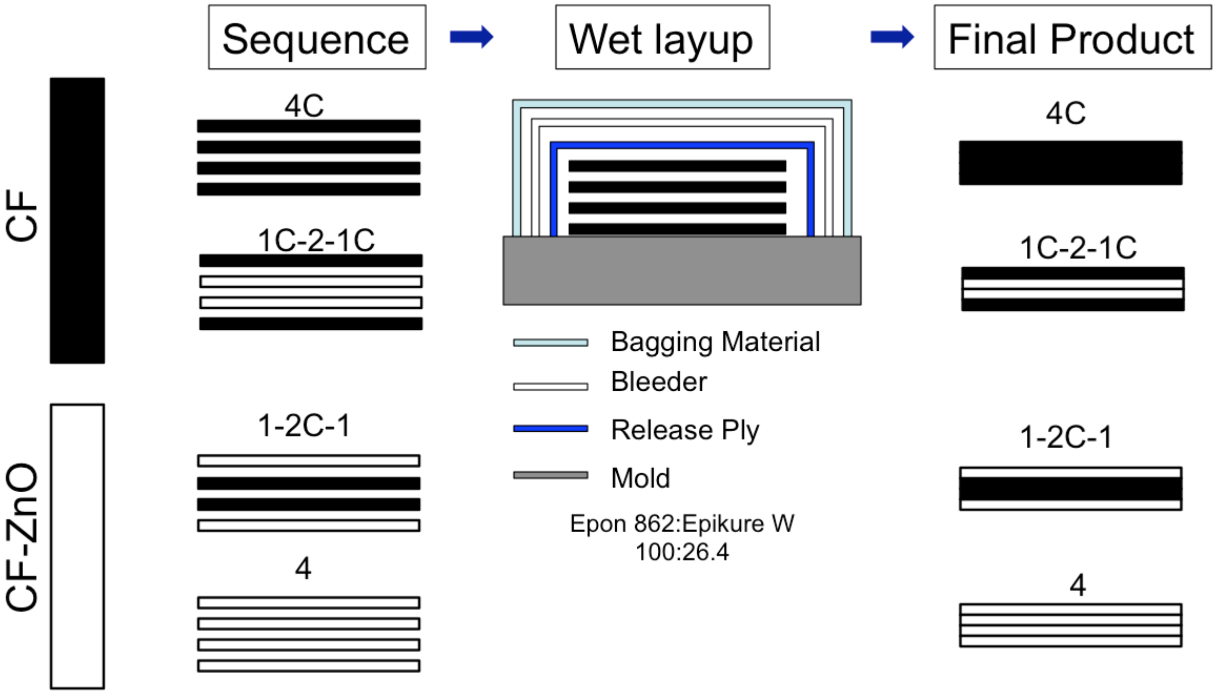

Figure 7. 1: Carbon fiber bundles with and without a ZnO coating are laid up in different sequences. A traditional wet hand layup method is used to make different composites.

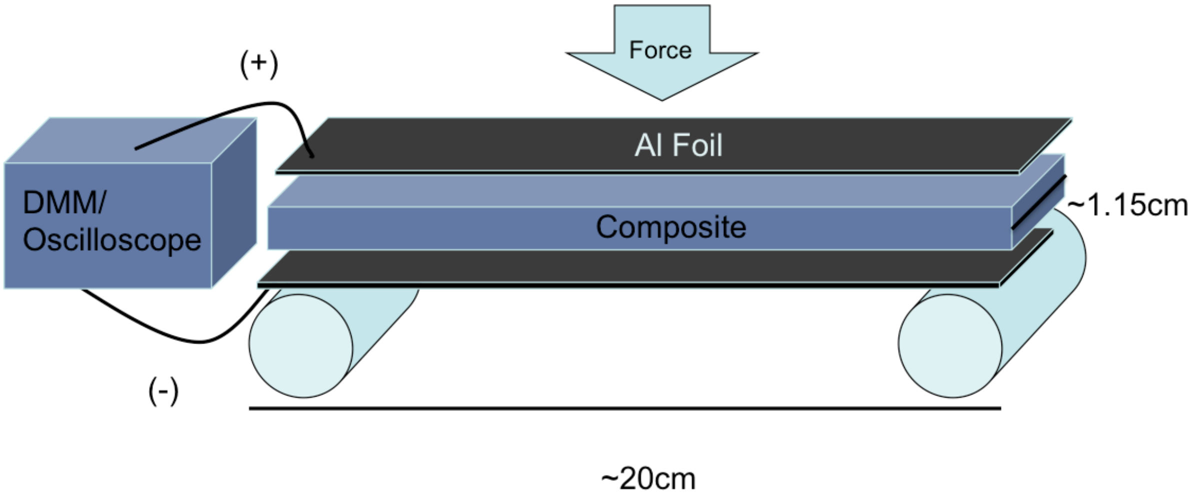

Figure 7. 2: A schematic of piezoelectric verification a multifunctional composite produced with ZnO nanostructures hybridized on carbon fibers.

7.6. References

1. Alipour Skandani, A.; Masghouni, N.; Case, S.; Leo, D.; Al-Haik, M., Enhanced vibration damping of carbon fibers-ZnO nanorods hybrid composites. *Applied Physics Letters* **2012,** *101* (7), 073111-073111-4.
2. Unalan, H. E.; Wei, D.; Suzuki, K.; Dalal, S.; Hiralal, P.; Matsumoto, H.; Imaizumi, S.; Minagawa, M.; Tanioka, A.; Flewitt, A. J., Photoelectrochemical cell using dye sensitized zinc oxide nanowires grown on carbon fibers. *Applied Physics Letters* **2008,** *93* (13), 133116.
3. Quintiere, J. G.; Walters, R. N.; Crowley, S., *Flammability Properties of Aircraft Carbon-Fiber Structural Composite*. Office of Aviation Research and Development, Federal Aviation Administration: 2007.